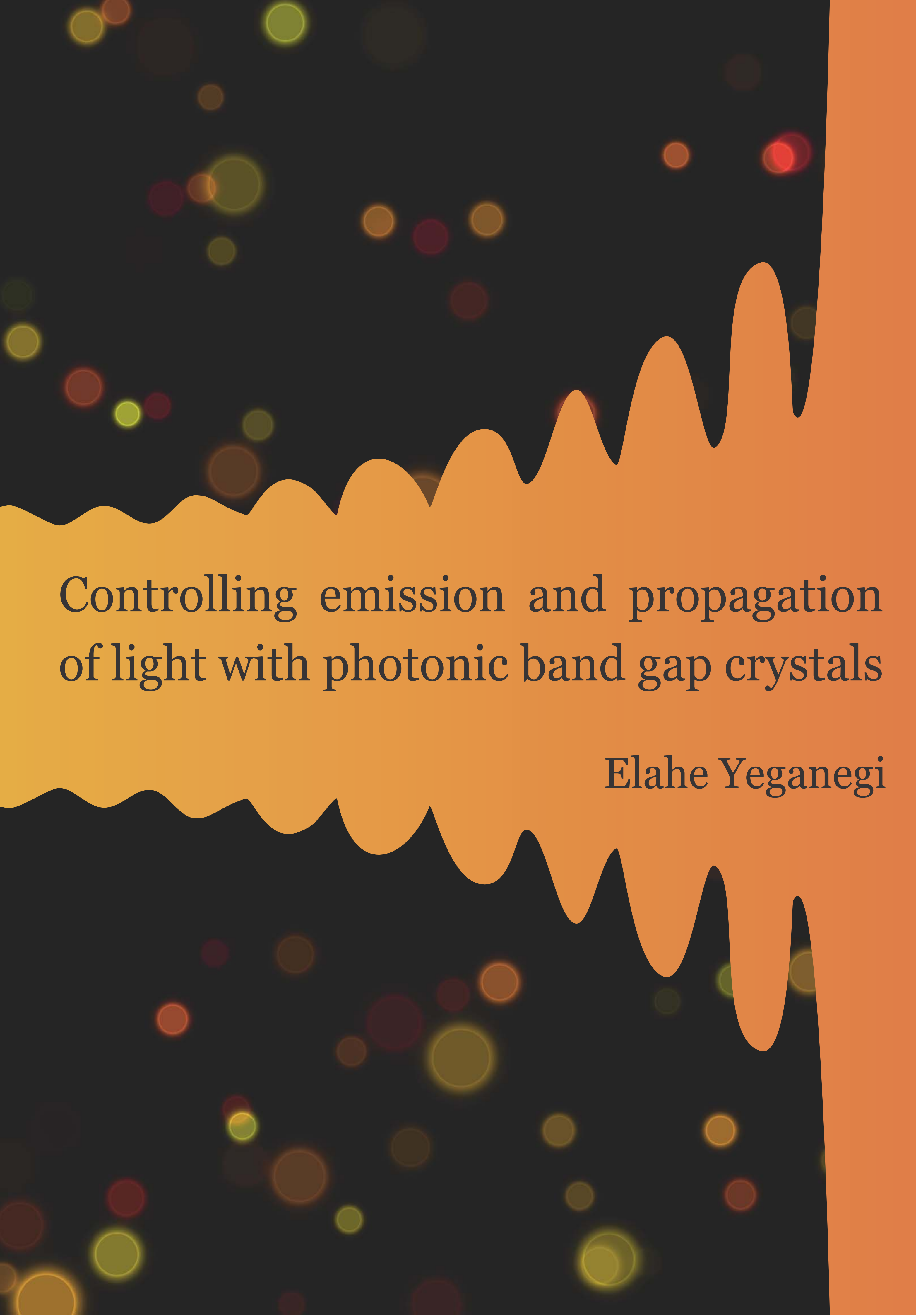

Controlling emission and propagation of light with photonic band gap crystals

Elahe Yeganegi

Controlling emission and propagation of light with photonic band gap crystals

Beheersen van de emissie en propagatie van licht met fotonische band gap kristallen

Promotiecommissie

Promotores	Prof. Dr. W. L. Vos Prof. Dr. A. Lagendijk
Overige leden	Prof. Dr. L. Novotny Prof. Dr. W. L. IJzerman Prof. Dr. J. Herek Prof. Dr. V. Subramaniam

The work described in this thesis is financially supported by the
'Nederlandse Organisatie voor Wetenschappelijk Onderzoek' (NWO).

It was carried out at the
Complex Photonic Systems (COPS) chair,
Department of Science and Technology
and MESA+ Institute for Nanotechnology,
University of Twente, P.O. Box 217,
7500 AE Enschede, The Netherlands.

ISBN: 9789461087652

CONTROLLING EMISSION AND PROPAGATION OF LIGHT WITH PHOTONIC BAND GAP CRYSTALS

PROEFSCHRIFT

ter verkrijging van
de graad van doctor aan de Universiteit Twente,
op gezag van de rector magnificus,
prof. dr. H. Brinksma,
volgens besluit van het College voor Promoties
in het openbaar te verdedigen
op woensdag 1 October 2014 om 12:45 uur

door

Elahe Yeganegi Dastgerdi

geboren op 9 september 1984
te Boroujen, Iran

Dit proefschrift is goedgekeurd door:

Prof. Dr. W. L. Vos en Prof. Dr. A. Lagendijk

Contents

CHAPTER 1

Introduction

The importance of light to mankind is reflected by the tremendous efforts that are being made worldwide to control its creation and propagation. Profiting from the interplay between light and matter, carefully designed optical elements, such as mirrors and lenses, have been successfully employed in the last centuries for light manipulation. Recently it has also become possible to manipulate light on length scales down to the nanoscale by using composite structures with feature sizes in the range of the wavelength or even smaller. This research is the realm of the young and blossoming field called nanophotonics, that has already yielded exciting new applications such as photonic crystal fibers with custom-made dispersion [1] that allow supercontinuum light sources [2], frequency combs and ultrastable clocks leading to a Nobel prize in physics [3], ultra high density data storage [4], optical antennas [5], efficient light sources [6], and many more.

One of the most fascinating phenomena in nanophotonics is the three-dimensional photonic band gap which provides an ultimate control over the interaction between light and matter, of which spontaneous emission is a well-known example [7]. By placing an emitter inside an ideal photonic band gap crystal, the emitter stays excited forever. The perfect control of the spontaneous emission is only attainable for an infinitely extended perfect photonic crystal. In real life, however, all crystals are finite, and disorder is inevitable. Therefore in this thesis we investigate the light propagation in real finite photonic crystals. This chapter gives a short introduction about several important subjects relevant to this study. An outline of this thesis is given at the end of this chapter.

1.1 Spontaneous emission under control

Spontaneous emission is one of the two fundamental processes of emitting a photon from a two-level system such as an atom, a molecule, or a quantum dot*. A simplistic representation of a two level system consists of a ground state with energy E_i and an excited state with energy E_f higher than E_i. As is shown in Fig. 1.1 the starting situation is that the emitter is excited. The emitter stays

---

* The other process of emitting a photon is stimulated emission.

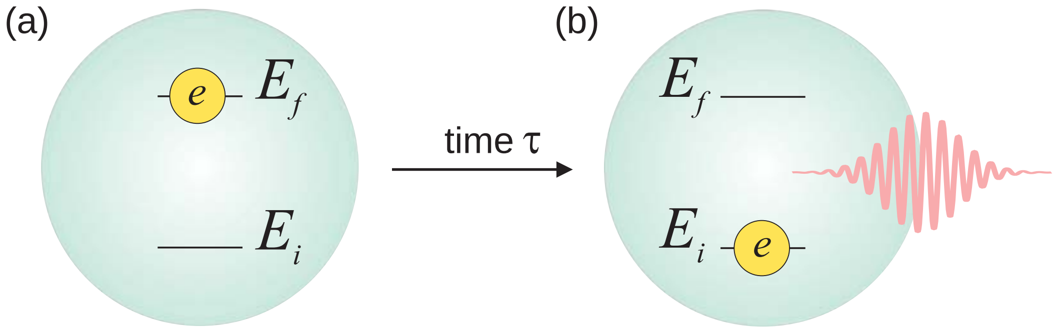

Figure 1.1: Schematic illustration of the spontaneous emission process. (a) The starting situation: Emitter is excited. (b) The emitter decays back to the ground state by emitting a photon.

excited for an average time τ, known as the emitters' lifetime, and then it decays to the ground state by emitting a photon. Interestingly, the exact moment in time that a photon is emitted can not be predicted. Nevertheless, the average time it takes -the lifetime- is well defined and can be finely controlled. The inverse of the lifetime is the decay rate γ, which is given by Fermi's Golden rule for dipole transition [8]:

$$\gamma(\mathbf{r}) = \frac{2\pi}{\hbar} \sum_{|f\rangle} |\langle f|\hat{\mathbf{d}}(\mathbf{r}) \cdot \mathbf{E}(\mathbf{r})|i\rangle|^2 \delta(E_f - E_i) \tag{1.1}$$

Here $\hat{\mathbf{d}}$ is the dipole transition moment operator. The decay rate is determined by summing over all available final states $|f\rangle$. Fermi's Golden Rule can be rewritten as [9, 10]:

$$\gamma(\mathbf{r}, \mathbf{e_d}, \omega) = \frac{\pi\omega d^2}{\hbar\epsilon_0} N_{rad}(\mathbf{r}, \mathbf{e_d}, \omega) \tag{1.2}$$

where the expression separates into an emitter part depending on the magnitude of the dipole moment d, and the field part or the local density of states LDOS N_{rad} that is a property of the emitters' environment. The LDOS counts the number of modes into which a photon can be emitted, and can be interpreted as the density of vacuum fluctuations at the position of the emitter as discovered by Sprik, *et al* [9]. Since the spontaneous emission rate depends on the projection of the dipole moment orientation on the local field, thus the emission rate is enhanced if the interaction of the dipole with the field is higher than in vacuum, and it is inhibited if it is lower. This equation only holds if the interaction between the emitter and the field is in the Markovian regime of quantum electrodynamics where the electromagnetic field-emitter interaction has an infinitely short memory [11]. Since the LDOS is a general physical property in any light-matter interaction, it is possible to control the radiative bandwidth of the resonance of a plasmonic particle (see App. C).

This irreversible emission process happens spontaneously and the emission time cannot be predicted *a priori*. The irreversible dynamics is valid in the Markovian regime where the transferred energy from the emitter to the electromagnetic field is irreversibly lost. A different type of dynamics occurs if the interaction between the emitter and vacuum modes of the electromagnetic field posses a finite memory time. In this case Fermi's Golden rule breaks down. An example is Rabi oscillations in which the emitter is coupled with a single resonance of the electromagnetic field leading to a periodic exchange of excitation energy between the atom and the field [12–14]. Strong variations in the spectral, and spatial distribution of the LDOS leads to fractional decay, where the Fermi's golden rule does not apply [15, 16]. Another breakdown of Fermi's golden rule occurs when the LDOS is nonstationary in time [17]. Fast modulations of the LDOS at times shorter than the emitters' lifetime cause a time dependent dynamics [18]. The study in this thesis is in the Markovian regime where Fermi's Golden Rule is valid.

1.2 General wave description: Green's functions

Green's function method is a very useful tool that provides complete information about systems that are described by linear differential equations [19]. In heat conduction the Green's function describes temperature at a chosen point due to a heat source located at the source point [20]. In classical mechanics the Green's function stands for displacements due to an applied force [21]. In electrodynamics it represents the electric field at the field point caused by an electric dipole emitter at the source point [22].

If a system is homogeneous the position of the source is unimportant. However, for an inhomogeneous medium the source position is an important parameter since the response to the point source depends on the source's position. The number of singularities in the Green's function gives the number of modes, because the Green's function diverges at resonant modes of the system. The scalar Green's function for a dipole in free space or in a homogeneous environment describes spherical waves [22]

$$G_0(\mathbf{r}, \mathbf{r}') = \frac{e^{\pm ik|\mathbf{r}-\mathbf{r}'|}}{4\pi|\mathbf{r}-\mathbf{r}'|}. \tag{1.3}$$

The solution with the plus sign denotes a spherical wave that propagates out of the origin whereas the solution with the minus sign is a wave that converges towards the origin. Since a dipole is generating the field it is physically correct to only retain the outward propagating wave. One of the physical properties accessible through the Green's function is the LDOS, that is the $\mathrm{Im}(\mathrm{G}_0(\mathbf{r}, \mathbf{r}, \omega))$ [10, 23, 24]. Thus for a homogeneous medium taking $\mathrm{Im}(\mathrm{G}_0(\mathbf{r}, \mathbf{r}))$, in Eq. (1.3) gives rise to LDOS $= 1$ for any choice of r as expected for a homogeneous system.

The solution becomes much more complicated if the emitter is in a complex environment such as a photonic crystal [25]. For complex media, such as photonic crystals the Green's function is not known, since the Maxwell equations cannot be solved analytically. The Green's function can be written as expansion of eigenfunctions of the system [10]. In practice one can calculate the eigenvalues and eigenfunctions of an infinite system using methods such as plane wave expansion methods in frequency domain or finite-difference time-domain(FDTD) [26]. In this thesis we propose a first theory for the LDOS in the band gap of a finite photonic crystal and it turns out that the insights in Green's function are crucial to solve this problem.

1.3 Photonic crystals

Photonic crystals are periodic composite structures of two or more different materials with a periodicity in the order of wavelength of light [26]. Typically one of the materials is air and the other one is a high index material such as silicon, GaAs, or AlAs. Depending on the periodicity, light with a certain wavelength range can not propagate into the crystal due to the Bragg diffraction. The Bragg condition is satisfied when light reflected from different planes in the crystal interferes constructively and thus a high reflectivity peak is observed at these wavelengths. Figure 1.2 illustrates the Bragg condition $m\lambda = 2dsin\theta$, with λ the Bragg diffracted wavelength, m an integer that is the order of the diffraction, d the spacing between the lattice planes, and θ the angle which light propagates with respect to the crystal planes. The appearance of a band gap is a consequence of Bragg diffraction. At the Bragg condition, a range of frequency exist for which propagation of light in certain directions is not possible: the so-called stop gap. Where the range of frequencies is determined experimentally, it is described with the term "stop band".

A basic parameter of photonic crystals is the photonic strength S. The photonic strength S that is defined as the polarizability per volume is a measure to describe how strongly light interacts with a complex photonic medium [27]. For very high S a band gap is expected to occur in periodic media. By measuring the central frequency of the stop band ω_{gap} and the stop band width $\Delta\omega_{gap}$ the photonic strength is determined as $S = \Delta\omega_{gap}/\omega_{gap}$. For an opal photonic crystal made by self-assembly processes of polystyrene particles $S \approx 0.06$, whereas for formation of a full photonic band gap the photonic strength should be higher : $S \geq 0.2$ [28].

The simplest photonic crystal, also known as Bragg stack, is an alternating sequence of layers of two or more materials, in which periodicity takes place only in one direction. If the structure is periodic in 2 directions it is a two-dimensional photonic crystal. A two-dimensional photonic crystal is capable of controlling light propagation in plane and is mostly used in in-plane photonic crystal waveguides or cavities [29–34]. The full potential of photonic crystals is achieved when the periodicity is extended in all directions forming a three-dimensional (3D) photonic crystal. If the stop gaps that appear at all directions overlap with each other a 3D full photonic band gap is formed where light is forbidden to travel in the crystal in all directions and for both polarizations [7].

There are three main classes of 3D photonic crystals that function as photonic band gap crystals: inverse opal [35–39], woodpile [40–48], and inverse woodpile

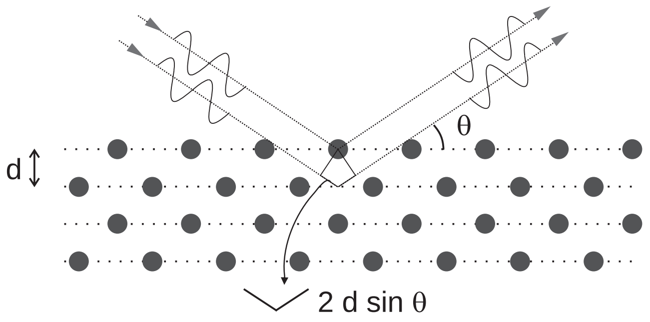

Figure 1.2: Schematic representation of the Bragg condition. Incident light is reflected from consecutive lattice planes. When the optical path length difference of the reflected light from different planes ($2dsin\theta$) is an integer number of the wavelength, the waves interfere constructively.

photonic crystals [49–55]. Although a photonic band gap can be seen in several other crystal geometries, the inverse woodpile photonic crystals are very interesting because of their relatively easy and robust fabrication process by etching pores in two directions and their high photonic strength of $S = 0.25$, resulting in a broad band gap [26, 56]. The photonic crystals studied in this thesis are 2D rectangular lattice and 3D inverse woodpile crystals with a diamond-like structure, fabricated by etching pores in a silicon wafer [56]. In chapter 2 we will describe the silicon inverse woodpile photonic crystals in more detail.

1.4 Diamond structured photonic crystals

In crystallography a diamond structure is a structure in which atoms are located in the same position as carbon atoms in a diamond crystal. The crystal structure of diamond consists of a face-centered cubic (*fcc*) lattice, with a basis of two identical carbon atoms associated with each lattice point: one at (0, 0, 0) and the other at (1/4, 1/4, 1/4), where the coordinates are given as fractions along the cube sides a. This is the same as two interpenetrating *fcc* lattices, each offset from the other along a body diagonal by one-quarter of its length $a/4$. The cubic lattice parameter a is the same as for the *fcc* lattice, but there are two atoms per rhombohedal primitive cell [57].

In the early 1990s the possibility to use photonic crystals with diamond-like structures was described in a number of papers, see Refs. [49, 58]. These photonic crystals are extremely interesting because they have significant potential for wide photonic bandgaps. Therefore, materials with relatively low refractive index contrasts of $m > 1.9$ suffice in order to obtain a photonic bandgap. A simultaneous advantageous feature of 3D diamond-like photonic crystals is that the bandgap is robust to unavoidable fabrication deviations and random disorder, see Refs. [59–61] for calculations on this aspect.

In one of the earliest studies calculations showed that air-spheres arranged in a diamond structure with a refractive index contrast of 3.6 would give wide

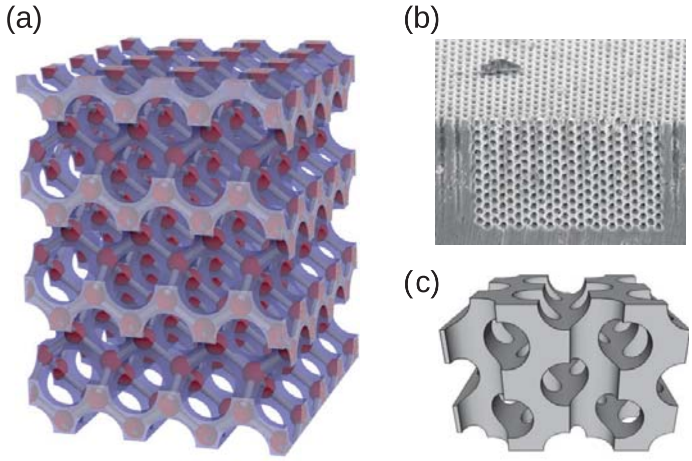

Figure 1.3: (a) Schematic representation of the structure of an "inverse woodpile" photonic crystal. It consists of two sets of pores perpendicular to each other, yielding a three-dimensional (3D) crystal structure. The structure is similar to a diamond crystal - shown with red spheres as carbon atoms as in diamond gem stone - yet 10,000 times magnified. The crystal controls the flow of light in an analogous way to how an atomic crystal controls the flow of electrons. Image courtesy of Léon Woldering. (b) SEM image of silicon inverse woodpile photonic crystal made in our group using CMOS-compatible nanotechnology. (c) Schematic image of position and overlap of the pores in our inverse woodpile crystal.

bandgaps of up to 28% bandwidth [58]. Unfortunately such diamond structures remain elusive to date. In a 2004 review diamond-like photonic crystals and the efforts to obtain them have been reviewed [62].

In 1991 diamond structures were proposed by etching or milling pores of air sequentially in three different directions in a backbone with a high index of refraction [63]. Such crystals were later fabricated from GaAs [64]. Transmission measurements were used to study the optical properties of these structures and an attenuation up to 80% was reported. A width of the bandgap of around 19% was reported, inferred from the width of the troughs in transmittance. In addition this paper emphasizes the importance of avoiding making these structures by etching or milling of tapered pores. This fabrication deviation was shown to have a significant effect on the band gap. Layer-by-layer woodpile structures were first proposed by the Iowa State group as a practical way to realize powerful diamond-structured photonic crystal [49]. The expected maximum width of the bandgap was predicted to be a sizable 18%. The crystal structure resembles a pile of logs of wood, hence their name. Diamond-like silicon spiral photonic crystals have been obtained by glancing angle deposition [65]. In this method, silicon is grown by electron beam evaporation on substrates that contain tungsten seeds. These seeds are arranged in a suitable square lattice with a lattice constant near 1000 nm. Silicon woodpiles have also been fabricated by direct laser writing of a template and subsequent double inversion to amorphous silicon [44]. Based on scanning electron micrographs, the expected bandgap for this structure was predicted to have a width of nearly 9%. Optical transmission measurements displayed a strong stop gap in the range of the expected bandgap. An intriguing method to fabricate diamond-like photonic crystals is biotemplating [66]. In this method, the diamond-like scale of a beetle is used as a template. By a double, sol-gel based, inversion method, the template is replicated in titania. The periodicity of these diamond-like structures is in the order of the wavelength of visible light. The expected width of the band gap of these structures is calculated to be around 5%, but the gap is probably narrower or even closed due to the significant structural distortions that are apparent in the scanning electron micrographs of the structures. Among all diamond structures, 3D photonic crystals known as “inverse-woodpile” are of particular interest [49] because of their conceptual ease of fabrication and a broad photonic band gap that is robust to disorder and fabrication imperfections [61, 67, 68]. Broad band gaps with widths exceeding 25% have been predicted for inverse woodpiles [49]. These crystals consist of pores that run in two perpendicular directions in a high-index backbone. Thus, the structure is the inverse of the woodpile structure. Figure 1.3 (a) shows a superposition of diamond structure with an inverse woodpile 3D photonic crystal. It is seen that the “carbon-atoms” from the superimposed diamond structure are positioned in the nodes of inverse-woodpile structure, confirming that an inverse woodpile has a diamond structure. Figure 1.3 (b) is a scanning electron micrograph of a 3D silicon inverse woodpile photonic crystal made in our group [55]. These crystals are realized by etching two sets of perpendicular pored in silicon wafer as described in Sec 2.2. A schematic image of the positions and overlap of the pores is shown in Fig. 1.3 (c). We will see in this thesis that the silicon inverse woodpile 3D photonic crystals are optically very powerful as they reveal prominent cavity QED effects on excited-state lifetimes.

1.5 Importance of three-dimensional photonic band gap

Many efforts have been stimulated over the years by the theoretical prediction that there exists an infinite three-dimensional, periodic structure that exhibits a three-dimensional (3D) photonic band gap [7, 69–71]. In this frequency range the density of optical states (DOS) is zero and vacuum fluctuations are inhibited. This characteristic property of the 3D bandgap crystal leads to novel phenomena in cavity quantum electrodynamics (cQED) [7, 69] where they offer at least five prospects for new physics. Firstly and probably the most eagerly pursued phenomenon is the complete inhibition of spontaneous emission. Any interaction mediated by vacuum fluctuations is affected by their suppression in the band gap [72]. Therefore, a crystal with a 3D photonic band gap not only inhibits spontaneous emission - including a shift of the emitter’s frequency known as the Lamb shift [73] - it will also modify the spectrum of blackbody radiation [74–76], it will affect resonant dipole-dipole interactions including the van der Waals and Casimir forces [77, 78], it will control the radiative width of plasmonic resonances [79], and the well-known Förster resonant energy transfer that is prominent in biology and chemistry [10, 72, 80]. Secondly, once a band gap is achieved, the cQED physics becomes even richer by introducing point defects. A point defect acts as a tiny cavity that is shielded in all three dimensions from the vacuum by the surrounding crystal [26, 81]. Hence such a photonic band gap cavity is literally a “nanobox for light”. A third reason why 3D photonic band gaps are relevant to solid state cQED occurs when a gain medium is introduced in a nanobox. Such a nanobox with gain offers the promise of a thresholdless laser [7]. Fourth, an important research theme in cQED is the breaking of the weak-coupling approximation. There are several ways to break the weak-coupling limit. One approach is to operate close to a van Hove singularity where the density of states has a cusp [57]. A second approach to break the weak-coupling limit consists of rapidly modulating the“bath” that surrounds a two-level quantum emitter [11], using ultrafast all-optical switching methods [17]. Fifth, in quantum physics there is an active interest in decoherence, that is, the loss of coherence between the components of a system that is in a quantum superposition [82]. Hence the shielding of vacuum fluctuations by a 3D photonic band gap offers opportunities to make optical quantum systems robust to decoherence.

In summary, (3D) photonic crystals with a 3D photonic bandgap play a fundamental role in cavity quantum electrodynamics (QED), especially in phenomena where the local density of optical states plays a central role. One can say that photonic bandgap crystals offer a knob to dial the density of states for broad frequency bandwidths over a wide range, from near zero to several times the value in vacuum. In this thesis we will study spontaneous emission inhibition of emitters embedded in a 3D bandgap crystal. Here, important progress has occurred in the last decade, bringing the long-sought inhibition from a theoretical prediction to experimental reality after forty years since the prediction by Bykov, Yablonovitch, and John [7, 69, 70]

1.6 Real 3D photonic band gap crystals

A complete photonic band gap where the photonic density of states vanishes and the propagation of light is strictly forbidden in all directions [36, 83] is a theoretical concept where crystals are assumed to be infinite and perfect. Real photonic crystals are always of finite size, therefore boundary effects are always present. In addition randomness and disorder in a real crystal is unavoidable. As a result the zero number of modes can never be reached and the DOS does not go to zero.

The first theoretical calculation of the emission rate in finite crystal was done by Whittaker in 2000 [84], Hermann and Hess in 2002 [85], and Kole in 2003 [86], resulting in a finite inhibition in the band gap. Hermann and Hess, and Kole calculated the modified emission rate for 3D finite inverse opal photonic band gap crystals using finite-difference time-domain methods, and Whittaker for woodpile photonic band gap crystals that are only finite in thickness but infinite laterally using scattering matrix approach. In addition to the finite size that limits the inhibition and introduces a small but finite DOS in the band gap, surface states are also omnipresent when a crystal is finite and they contribute to the inhibition in the band gap. In this thesis we will see that contribution of the surface states is negligible compared to the finite size effect due to the finite crystal volume, see chapter 4. It is also important to keep in mind that the surface states exist only at some particular termination of the crystal as discussed in Ref.[26]. In addition to the finite size, in a real photonic crystal disorder and randomness are also inevitable. Several studies show effect of disorder on the DOS in photonic band gap crystals [59, 87]. As the theoretical calculations show the disorder gives rise to the Lifshitz tail in the band gap, and therefore narrowing down the band gap width. In chapter 6 we study the disorder induced to the crystals during the fabrication process of our silicon photonic crystals. Similar measurements are performed on synthesized opal photonic crystals. The coherent length, long range, and short range order are studied showing that the disorder effects can be neglected in fabricated photonic crystals. To the best of our understanding, the most important property of a real photonic crystal that makes it different than an ideal crystal are the finite size effects. Therefore in chapters 3 and 4 the finite size effect is extensively discussed.

1.7 Probing the local density of states

Since the LDOS is one of the two determining factor of the coupling between quantum emitters and their photonic environment, measuring the LDOS provides key fundamental insights into light-matter interaction in nano-scales.

As mentioned in Sec.1.1, one method to probe the LDOS in nanoscale is emission measurements. The local density of states is proportional to the radiative decay rate of emitters. By fixing the emitters position at particular positions in the nano-structure and optically exciting them the emitters decay rate is measured [88]. Since the radiative decay rate is proportional to the LDOS, the LDOS can be derived precisely. In this case the efficiency of the method is limited by the quantum efficiency of emitters and the spatial resolution of measuring the LDOS depends on how accurately emitters are positioned in the structure. Self-assembled quantum dots which are grown in the high index material are used to measure the LDOS in high index part of the structure [89], and colloidal quantum dots or dye molecules that are fixed in low index material or bound to structure with polymer layers are used to measure the LDOS in the low index part of the structure [90].

Another method is Cathodoluminescence microscopy, where a beam of fast electrons is used as excitation source. The advantage of this method is that structures can be probed with a very high spatial resolution of 1-10 nm, similar to electron microscopes. However, this is an advantage from the imaging point of view. For probing the local properties of the structure the high resolution is perished due to diffusion of electrons inside the structure. Therefore despite a very high resolution focus, the measured values for the LDOS are averaged over the diffused volume of the electrons [91]. Since the electron beam excites the electron in high index material this method is limited to measuring the LDOS only in high index material.

A third method to measure the LDOS is to measure the group velocity at constant frequency for all wave vectors, since the DOS can be written as an integral of the inverse group velocity over all wave vectors. and scale that with the local field at every position in the structure for 4π angles [57]. Due to complexity, this method has not been successfully applied for the LDOS measurements after it has been proposed theoretically.

1.8 Outline of this thesis

In this thesis both theoretical and experimental studies about light propagation in real photonic band gap crystals are presented. We investigate several aspects of a real photonic band gap crystal by different types of measurements such as time resolved emission of light sources in the band gap, scattering of light due to randomness and probing the internal wave structure in the photonic crystals.

In chapter 2, we describe the silicon inverse woodpile photonic crystals that we use in our emission control measurements in this thesis. We present our study on optical properties of PbS quantum dots that have been used as light sources in the photoic band gap crystal. Finally, we describe the near-infrared setup used for most of our measurements throughout this thesis.

In chapter 3, we present our theoretical study of the local density of states (LDOS) in the band gap of a finite one-dimensional photonic crystal. In this study we propose two new Ansatzes based on well-known physical concepts. Our original view points allow us to develop a model for the LDOS in the band gap of a finite photonic crystal.

Chapter 4 describes a quantitative study of finite size effect in 3D photonic band gap crystal. We first present our experimental study on inhibition in the band gap as a function of frequency. In this study we observe the highest ever inhibition observed in the band gap range. The inhibition is very strong, yet limited, due to the finite size of the crystal. We develop a theory to describe the finite size effect on inhibition in the band gap crystal.

Chapter 5 demonstrates a Bayesian statistical analysis approach that we applied to our time-resolved emission data analysis. Due to a high level of background in the time-resolved measurements a Bayesian analysis was required to refine the model parameters.

In chapter 6, we present our study on probing the internal structure of synthesized opal and fabricated 2D silicon photonic crystals using imaging techniques. Although the methods that are used in this chapter are very simple, the collected data is surprisingly complex to analyze. We present different approaches to probe the internal structure of a real photonic crystal and we conclude this chapter with proposed methods for the future experiments.

In chapter 7, we study out-of-plane scattering of light in 2D silicon photonic crystals. By illuminating a photonic crystal and a multiple scattering sample with a broad band white light source we quantify the differences in light transport inside periodic and random photonic structures.

Chapter 8 concludes the thesis. A summary of the thesis is presented and an outlook on future theoretical and experimental studies is given.

The initial research question of this thesis was to manipulate the radiative rate of the plasmonic particles using photonic band gap crystals. Preliminary experiments were done to investigate the feasibility of this study. However, it turned out that due to a low quality of the currently available plasmonic particles the experiment would not work. The preliminary results are presented in appendix C of this thesis.

Bibliography

[1] P. Russell, *Photonic crystal fibers*, Science **299**, 358 (2003). — p.11.

[2] J. Clowes, *Next generation light sources for biomedical applications*, Optik & Photonik **3**, 36 (2008). — p.11.

[3] S. A. Diddams, D. J. Jones, J. Ye, S. T. Cundiff, J. L. Hall, J. K. Ranka, R. S. Windeler, R. Holzwarth, T. Udem, and T. W. Hänsch, *Direct link between microwave and optical frequencies with a 300 thz femtosecond laser comb*, Phys. Rev. Lett. **84**, 5102 (2000). — p.11.

[4] B. H. Cumpston *et al.*, *Two-photon polymerization initiators for three-dimensional optical data storage and microfabrication*, Nature **398**, 51 (1999). — p.11.

[5] P. Bharadwaj, B. Deutsch, and L. Novotny, *Optical antennas*, Adv. Opt. Photon. **1**, 438 (2009). — p.11.

[6] J. J. Wierer, A. David, and M. M. Megens, *III-nitride photonic-crystal light-emitting diodes with high extraction efficiency*, Nature Photon. **3**, 163 (2009). — p.11.

[7] E. Yablonovitch, *Inhibited spontaneous emission in solid-state physics and electronics*, Phys. Rev. Lett. **58**, 2059 (1987). — p.11, 14, 17, 18.

[8] E. Fermi, *Quantum theory of radiation*, Rev. Mod. Phys. **4**, 87 (1932). — p.12.

[9] R. Sprik, B. A. van Tiggelen, and A. Lagendijk, *Optical emission in periodic dielectrics*, Europhys. Lett. **35**, 265 (1996). — p.12.

[10] L. Novotny and B. Hecht, *Principles of nano-optics* (Cambridge University Press, New York, 2006). — p.12, 13, 14, 17.

[11] A. Lagendijk, in *Vibrational relaxation studied with light, pages 197-238 in: Ultrashort processes in condensed matter*, edited by W. E. Bron (Plenum, New York, 1993). — p.12, 18.

[12] J. P. Reithmaier, G. Sęk, A. Löffler, C. Hofmann, S. Kuhn, S. Reitzenstein,

L. V. Keldysh, V. D. Kulakovskii, T. L. Reinecke, and A. Forchel, *Strong coupling in a single quantum dot-semiconductor microcavity system*, Nature **432**, 197 (2004). — p.13.

[13] T. Yoshie, A. Scherer, J. Hendrickson, G. Khitrova, H. M. Gibbs, G. Rupper, C. Ell, O. B. Shchekin, and D. G. Deppe, *Vacuum rabi splitting with a single quantum dot in a photonic crystal nanocavity*, Nature **432**, 201 (2004). — p.13.

[14] P. Maunz, T. Puppe, I. Schuster, N. Syassen, P. W. H. Pinkse, and G. Rempe, *Normal-mode spectroscopy of a single-bound-atom–cavity system*, Phys. Rev. Lett. **94**, 033002 (2005). — p.13.

[15] S. John and T. Quang, *Spontaneous emission near the edge of a photonic bandgap*, Phys. Rev. A **50**, 1764 (1994). — p.13.

[16] P. T. Kristensen, A. F. Koenderink, P. Lodahl, B. Tromborg, and J. Mork, *Fractional decay of quantum dots in real photonic crystals*, Opt. Lett. **33**, 1557 (2008). — p.13.

[17] P. M. Johnson, A. F. Koenderink, and W. L. Vos, *Ultrafast switching of photonic density of states in photonic crystals*, Phys. Rev. B **66**, 081102 (2002). — p.13, 18.

[18] H. Thyrrestrup, A. Hartsuiker, J.-M. Gérard, and W. L. Vos, *Non-exponential spontaneous emission dynamics for emitters in a time-dependent optical cavity*, Opt. Express. **21**, 23130 (2013). — p.13.

[19] D. Duffy, *Green's functions with applications* (Taylor & Francis, 2001). — p.13.

[20] J. V. Beck, *Heat Conduction Using Green's Functions* (Hemisphere Publishing Corporation, 1992). — p.13.

[21] H. Goldstein, C. P. Poole, and J. L. Safko, *Classical mechanics* (Pearson Education, Limited, 2013). — p.13.

[22] J. Jackson, *Classical electrodynamics* (Wiley, 1999). — p.13.

[23] A. Lagendijk and B. A. Van Tiggelen, *Resonant multiple scattering of light*, Phys. Rep. **270**, 143 (1996). — p.13.

[24] K. Joulain, R. Carminati, J. P. Mulet, and J. J. Greffet, *Definition and measurement of the local density of electromagnetic states close to an interface*, Phys. Rev. B **68**, 245405 (2003). — p.13.

[25] K. Sakoda, *Optical properties of photonic crystals* (Springer, 2005). — p.13.

[26] J. D. Joannopoulos, S. G. Johnson, J. N. Winn, and R. D. Meade, *Photonic crystals - molding the flow of light, 2nd edition* (Princeton University Press, 2008). — p.14, 15, 18, 19.

[27] W. Vos, R. Sprik, A. van Blaaderen, A. Imhof, A. Lagendijk, and G. H. Wegdam, *Strong effects of photonic band structures on the diffraction of colloidal crystals*, Phys. Rev. B. **53**, 16231 (1996). — p.14.

[28] A. F. Koenderink, *Emission and transport of light in photonic crystals*, Ph.D. thesis, (University of Amsterdam) available from: www.photonicbandgaps.com, 2003. — p.14.

[29] T. F. Krauss, R. M. De La Rue, and S. Brand, *2-dimensional photonicbandgap structures operating at near-infrared wavelengths*, Nature **383**, 699 (1996). — p.14.

[30] M. Kanskar, P. Paddon, V. Pacradouni, R. Morin, A. Busch, J. F. Young, S. R. Johnson, J. MacKenzie, and T. Tiedje, *Observation of leaky slab modes in an air-bridged semiconductor waveguide with a two-dimensional photonic lattice*, Appl. Phys. Lett. **70**, 1438 (1997). — p.14.

[31] T. Baba, N. Fukaya, and J. Yonekura, *Observation of light propagation in photonic crystal optical waveguides with bends*, Electron. Lett. **35**, 654 (1999). — p.14.

[32] M. Lončar, D. Nedeljković, T. Doll, J. Vučković, A. Scherer, and T. P. Pearsall, *Waveguiding in planar photonic crystals*, Appl. Phys. Lett. **77**, 1937 (2000). — p.14.

[33] S. Olivier, C. Smith, M. Rattier, H. Benisty, C. Weisbuch, T. Krauss, R. Houdre, and U. Oesterle, *Miniband transmission in a photonic crystal coupled-resonator optical waveguide*, Opt. Lett. **26**, 1019 (2001). — p.14.

[34] J. Vuckovic, M. Loncar, H. Mabuchi, and A. Scherer, *Optimization of the q factor in photonic crystal microcavities*, IEEE J. Quant. Electron. **38**, 850 (2002). — p.14.

[35] J. E. G. J. Wijnhoven and W. L. Vos, *Preparation of photonic crystals made of air spheres in titania*, Science **281**, 802 (1998). — p.14.

[36] K. Busch and S. John, *Photonic band gap formation in certain self-organizing systems*, Phys. Rev. E **58**, 3896 (1998). — p.14, 18.

[37] A. Blanco, E. Chomski, S. Grabtchak, M. Ibisate, S. John, S. W. Leonard, C. Lopez, F. Meseguer, H. Miguez, J. P. Mondia, G. A. Ozin, O. Toader, and H. M. van Driel, *Large-scale synthesis of a silicon photonic crystal with a complete three-dimensional bandgap near 1.5 micrometres*, Nature **405**, 437 (2000). — p.14.

[38] Y. A. Vlasov, X. Z. Bo, J. C. Sturm, and D. J. Norris, *On-chip natural assembly of silicon photonic bandgap crystals*, Nature **414**, 289 (2001). — p.14.

[39] T. Euser, H. Wei, J. Kalkman, Y. Jun, A. Polman, D. J. Norris, and W. L. Vos, *All-optical octave-broad ultrafast switching of si woodpile photonic band gap crystals*, J. Appl. Phys. **102**, 053111 (2007). — p.14.

[40] J. G. Fleming and S. Y. Lin, *Three-dimensional photonic crystal with a stop band from 1.35 to 1.95 μm*, Opt. Lett. **24**, 49 (1999). — p.14.

[41] S. Noda, K. Tomoda, N. Yamamoto, and A. Chutinan, *Full three-dimensional photonic bandgap crystals at near-infrared wavelengths*, Science **289**, 604 (2000). — p.14.

[42] M. Qi, E. Lidorikis, P. T. Rakich, S. G. Johnson, J. D. Joannopoulos, E. P. Ippen, and H. I. Smith, *A three-dimensional optical photonic crystal with designed point defects*, Nature **429**, 538 (2004). — p.14.

[43] I. Povey, D. Whitehead, K. Thomas, M. Pemble, M. Bardosova, and J. Renard, *Photonic crystal thin films of gaas prepared by atomic layer deposition*, Appl. Phys. Lett. **89**, 104103 (2006). — p.14.

[44] N. Tétreault, G. von Freymann, M. Deubel, M. Hermatschweiler, F. Pérez-Willard, S. John, M. Wegener, and G. A. Ozin, *New route to three-dimensional photonic bandgap materials: silicon double inversion of polymer templates*, Adv. Mater. **18**, 457 (2006). — p.14, 16.

[45] K. Aoki, D. Guimard, M. Nishioka, M. Nomura, S. Iwamoto, and Y. Arakawa, *Coupling of quantum-dot light emission with a three-dimensional photonic-crystal nanocavity*, Nature Photon. **2**, 688 (2008). — p.14.

[46] S. Ogawa, K. Ishizaki, T. Furukawa, and S. Noda, *Spontaneous emission control by 17 layers of three-dimensional photonic crystals*, Electronics Lett. **44**, 377 (2008). — p.14.

[47] S. Kawashima, K. Ishizaki, and S. Noda, *Light propagation in three-dimensional photonic crystals*, Opt. Express. **18**, 386 (2009). — p.14.

[48] K. Ishizaki, M. Koumura, K. Suzuki, K. Gondaira, and S. Noda, *Realization of three-dimensional guiding of photons in photonic crystals*, Nature Photon. **7**, 133 (2013). — p.14.

[49] K. M. Ho, C. T. Chan, C. M. Soukoulis, R. Biswas, and M. Sigalas, *Photonic band gaps in three dimensions: new layer-by-layer periodic structures*, Solid State Commun. **89**, 413 (1994). — p.15, 16, 17.

[50] J. Schilling, J. White, A. Scherer, G. Stupian, R. Hillebrand, and U. Gösele, *Three-dimensional macroporous silicon photonic crystal with large photonic band gap*, Appl. Phys. Lett. **86**, 011101 (2005). — p.15.

[51] S. Takahashi, M. Okano, M. Imada, and S. Noda, *Three-dimensional photonic crystals based on double-angled etching and wafer-fusion techniques*, Appl. Phys. Lett. **89**, 123106 (2006). — p.15.

[52] M. Hermatschweiler, A. Ledermann, G. A. Ozin, M. Wegener, and G. von Freymann, *Fabrication of silicon inverse woodpile photonic crystals*, Adv. Func. Mater. **17**, 2273 (2007). — p.15.

[53] S. Takahashi, K. Suzuki, M. Okano, M. Imada, T. Nakamori, Y. Ota, K. Ishizaki, and S. Noda, *Direct creation of three-dimensional photonic crystals by a top-down approach*, Nat. Mater. **8**, 721 (2009). — p.15.

[54] D. J. Shir, E. C. Nelson, D. Chanda, A. Brzezinski, P. V. Braun, J. A. Rogers, and P. Wiltzius, *Dual exposure, two-photon, conformal phase mask lithography for three dimensional silicon inverse woodpile photonic crystals*, J. Vac. Sci. Technol. B **28**, 783 (2010). — p.15.

[55] J. M. van den Broek, L. A. Woldering, R. W. Tjerkstra, F. B. Segerink, I. D. Setija, and W. L. Vos, *Inverse-woodpile photonic band gap crystals with a cubic diamond-like structure made from single-crystalline silicon*, Adv. Funct. Mater. **22**, 25 (2012). — p.15, 17.

[56] L. A. Woldering, *Fabrication of photonic crystals and nanocavities*, PhD Thesis, University of Twente, 2008. — p.15.

[57] N. W. Ashcroft and N. D. Mermin, *Solid state physics* (Holt, Rinehart and Winston, New York, 1976). — p.15, 18, 20.

[58] K. M. Ho, C. T. Chan, and C. M. Soukoulis, *Existence of a photonic gap in periodic dielectric structures*, Phys. Rev. Lett. **65**, 3152 (1990). — p.15, 16.

[59] M. M. Sigalas, C. M. Soukoulis, C. T. Chan, R. Biswas, and K. M. Ho, *Effect of disorder on photonic band gaps*, Phys. Rev. B **59**, 12767 (1999). — p.15, 19.

[60] R. Hillebrand and W. Hergert, *Scaling properties of a tetragonal photonic crystal design having a large complete bandgap*, Phot. Nano. Fund. Appl. **2**,

33 (2004). — p.15.

[61] L. A. Woldering, A. P. Mosk, R. W. Tjerkstra, and W. L. Vos, *The influence of fabrication deviations on the photonic band gap of three-dimensional inverse woodpile nanostructures*, J. Appl. Phys. **105**, 093108 (2009). — p.15, 17.

[62] M. Maldovan and E. L. Thomas, *Diamond-structured photonic crystals*, Nat. Mater. **3**, 593 (2004). — p.16.

[63] E. Yablonovitch, T. J. Gmitter, and K. M. Leung, *Photonic band stucture: the face-centered-cubic case employing nonspherical atoms*, Phys. Rev. Lett. **67**, 2295 (1991). — p.16.

[64] C. C. Cheng, V. Arbet-Engels, A. Scherer, and E. Yablonovitch, *Nanofabricated three dimensional photonic crystals operating at optical wavelengths*, Phys. Scr. **T68**, 17 (1996). — p.16.

[65] D.-X. Ye, Z.-P. Yang, A. S. Chang, J. Bur, S. Y. Lin, T.-M. Lu, R. Z. Wang, and S. John, *Experimental realization of a well-controlled 3d silicon spiral photonic crystal*, J. Phys. D **40**, 2624 (2007). — p.16.

[66] J. W. Galusha, M. R. Jorgensen, and M. H. Bartl, *Diamond-structured titania photonic-bandgap crystals from biological templates*, Adv. Mater. **22**, 107 (2010). — p.17.

[67] A. Chutinan and S. Noda, *Effects of structural fluctuations on the photonic bandgap during fabrication of a photonic crystal*, J. Opt. Soc. Am. B **16**, 240 (1999). — p.17.

[68] J. Schilling and A. Scherer, *Photonics nanostruct*, Fundam. Appl **3**, 90 (2005). — p.17.

[69] V. Bykov, *Spontaneous emission in a periodic structure*, Sov. Phys. JETP **35**, 269 (1972). — p.17, 18.

[70] S. John, *Strong localization of photons in certain disordered dielectric superlattices*, Phys. Rev. Lett. **58**, 2486 (1987). — p.17, 18.

[71] C. M. Soukoulis, *Photonic band gap materials : The semiconductors of the future?.*, Physica Scripta **T66**, 146 (1996). — p.17.

[72] S. Haroche, in *Cavity quantum electrodynamics, pages 767–940 in: Fundamental systems in quantum optics*, edited by J. Dalibard, J. M. Raimond, and J. Zinn-Justin (North Holland, Amsterdam, 1992). — p.17.

[73] S. John and J. Wang, *Quantum electrodynamics near a photonic band gap: Photon bound states and dressed atoms*, Phys. Rev. Lett. **64**, 2418 (1990). — p.17.

[74] J. G. Fleming, S. Y. Lin, I. El-Kady, R. Biswas, and K. M. Ho, *All-metallic three-dimensional photonic crystals with a large infrared bandgap*, Nature **417**, 52 (2002). — p.17.

[75] J. Fleming, *Addendum: Three-dimensional photonic-crystal emitter for thermal photovoltaic power generation*, Appl. Phys. Lett. **86**, 249902 (2005). — p.17.

[76] A. Babuty, K. Joulain, P. O. Chapuis, J. J. Greffet, and Y. De Wilde, *Blackbody spectrum revisited in the near field*, Phys. Rev. Lett. **110**, 146103 (2013). — p.17.

[77] G. Kurizki and A. Genack, *Suppression of molecular interactions in periodic*

dielectric structures, Phys. Rev. Lett. **61**, 2269 (1988). — p.17.

[78] M. I. Antonoyiannakis and J. B. Pendry, *Electromagnetic forces in photonic crystals*, Phys. Rev. B **60**, 2363 (1999). — p.17.

[79] B. C. Buchler, T. Kalkbrenner, C. Hettich, and V. Sandoghdar, *Measuring the quantum efficiency of the optical emission of single radiating dipoles using a scanning mirror*, Phys. Rev. Lett. **95**, 063003 (2005). — p.17.

[80] C. Blum, N. Zijlstra, A. Lagendijk, M. Wubs, A. P. Mosk, V. Subramaniam, and W. L. Vos, *Nanophotonic control of the förster resonance energy transfer efficiency*, Phys. Rev. Lett. **109**, 203601 (2012). — p.17.

[81] E. Yablonovitch, T. J. Gmitter, R. D. Meade, A. M. Rappe, K. D. Brommer, and J. D. Joannopoulos, *Donor and acceptor modes in photonic band structure*, Phys. Rev. Lett. **67**, 3380 (1991). — p.18.

[82] W. H. Zurek, *Decoherence and the transition from quantum to classical*, Phys. Today **44**, 36 (1991). — p.18.

[83] S. John and K. Busch, *Photonic bandgap formation and tunability in certain self-organizing systems*, J. Lightwave Technol. **17**, 1931 (1999). — p.18.

[84] D. M. Whittaker, *Inhibited emission in photonic woodpile lattices*, Opt. Lett. **25**, 779 (2000). — p.18.

[85] C. Hermann and O. Hess, *Modified spontaneous-emission rate in an inverted-opal structure with complete photonic bandgap*, J. Opt. Soc. Am. B **19**, 18 (2002). — p.18.

[86] S. Kole, *New methods for the numerical solution of maxwell's equations*, PhD Thesis, Rijksuniversiteit Groningen, 2003. — p.18.

[87] S. R. Huisman, G. Ctistis, S. Stobbe, A. P. Mosk, J. L. Herek, A. Lagendijk, P. Lodahl, W. L. Vos, and P. W. H. Pinkse, *Measurement of a band-edge tail in the density of states of a photonic-crystal waveguide*, Phys. Rev. B **86**, 155154 (2012). — p.19.

[88] P. Anger, P. Bharadwaj, and L. Novotny, *Enhancement and quenching of single-molecule fluorescence*, Phys. Rev. Lett. **96**, 113002 (2006). — p.19.

[89] Q. Wang, S. Stobbe, and P. Lodahl, *Mapping the local density of optical states of a photonic crystal with single quantum dots*, Phys. Rev. Lett. **107**, 167404 (2011). — p.19.

[90] M. D. Leistikow, J. Johansen, A. J. Kettelarij, P. Lodahl, and W. L. Vos, *Size-dependent oscillator strength and quantum efficiency of CdSe quantum dots controlled via the local density of states*, Phys. Rev. B **79**, 045301 (2009). — p.19.

[91] T. Coenen, *Angle-resolved cathodoluminescence nanoscopy*, PhD Thesis, Amsterdam University, 2014. — p.19.

CHAPTER 2

Samples and instrumentation

2.1 Introduction

We give a short introduction on silicon inverse woodpile photonic crystals, that have been used for controlling light propagation in this thesis. To avoid light absorption by silicon we use PbS quantum dots that emit in the near infrared as light sources in photonic crystals. Before infiltrating quantum dots in the complex environment of photonic crystals we characterize their behavior in suspension. We measure emission and absorption spectra, as well as time-resolved emission measured by time-correlated single-photon counting method. The experiments performed in this thesis require a number of special requirements and therefore we needed to have a custom-designed experimental setup. The main purpose of this setup is to investigate the control of spontaneous emission using photonic crystals. The setup is designed to enable not only emission measurements but also reflection, and transmission measurements on silicon inverse woodpile photonic crystals in the near infrared range.

2.2 Silicon inverse woodpile photonic crystals

As discussed in chapter.1 our photonic crystals are designed so that they can manipulate and control light propagation in a certain range of wavelengths. In this thesis we have mainly studied silicon inverse woodpile photonic crystals because of their broad and complete photonic band gap for all directions and both polarizations. This is obtained by the extent of the crystal in all three dimensions. A cubic inverse woodpile photonic crystal consists of two perpendicular, geometrically identical sets of cylindrical pores, as first proposed by Ho *et al.* [1]. The combination of the two sets of pores results in a three-dimensional structure with a face-centered-cubic lattice and a diamond-like symmetry. By optimizing the crystal parameters such as pore radius and lattice parameters, it is possible to realize a full 3D band gap (see Fig. 2.1) with a broad relative width of more than $\Delta\omega/\omega = 25\%$ [2, 3].

Figure 2.1(a) shows a scanning electron micrograph of a silicon 3D inverse woodpile photonic crystal fabricated in our group using CMOS compatible methods [5, 6]. The extent of the 3D crystal is indicated by the red dashed lines and the 3D crystal is surrounded by the parent 2D crystal. Figure 2.1(b) illustrates the designed structure of a 3D inverse woodpile crystal with lattice parameters a

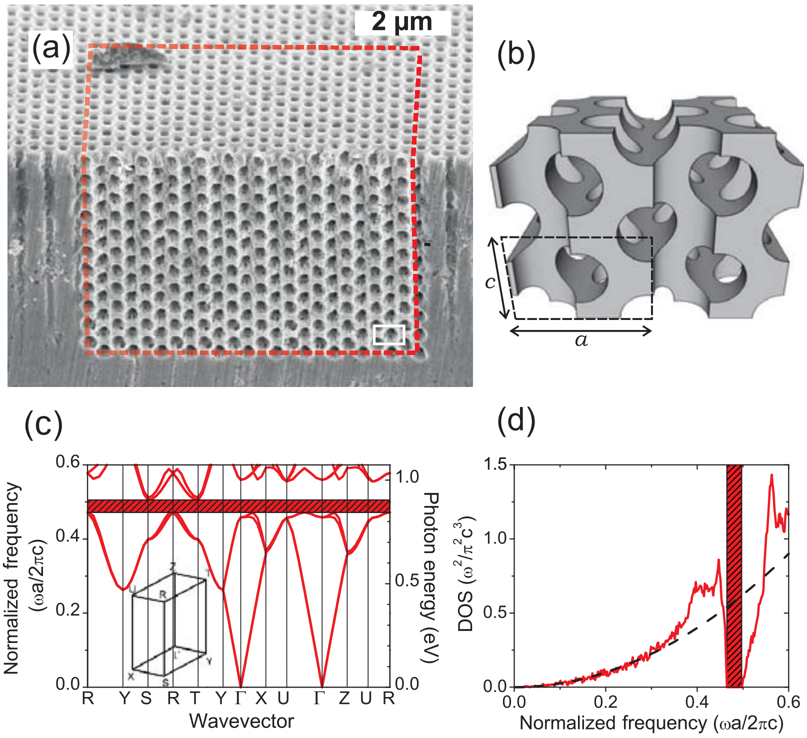

Figure 2.1: (a) Scanning electron micrograph of a 3D inverse woodpile photonic crystal made from silicon. The 3D crystal is delimited by the dashed lines and consists of two perpendicularly etched sets of carefully aligned pores, surrounded by a 2D crystal. (b) Schematic image showing the positions and overlap of the pores, and unit cell parameters a and c. (c) Band structure of an inverse woodpile photonic crystal with pore radius 170 nm, $\varepsilon = 12.1$ for silicon and $\varepsilon = 2.25$ for toluene-filled pores. The band gap is indicated with the red bar. Inset: first Brillouin zone. (d) Density of states (DOS) per volume for the same crystal calculated with 10000 k-points [4]. The DOS vanishes in the band gap. Dashed curve: quadratic behavior in the low frequency limit.

and c. The SEM image shows that the fabricated crystals compare well to the designed structures. The cubic crystals have lattice parameters $a = 693$ and $c = 488$ nm ($a/c = \sqrt{2}$), and a range of pore radii ($136 < r < 186$ nm) to tune the band gap to different frequencies. The 3D crystals extend over $L^3 = 12a \times 12c \times 12c$, which exceeds the Bragg attenuation length (see [7, 8]) in every direction [9]. The good optical quality and high photonic interaction strength (see [10]) of our crystals were confirmed by optical reflectivity experiments where intense and broad peaks were observed. The stop bands overlap for all probed directions and polarizations, which consists the first ever experimental signature of a 3D photonic band gap [9].

Fig. 1(c) shows the calculated band structure [4] for an inverse woodpile crystal. A photonic band gap appears in the frequency range where modes are forbidden for all wave vectors and polarizations. Fig. 1(d) shows the corresponding density of states (DOS). In Figs. Fig. 2.1(c) and (d), the band gap has somewhat narrowed since we consider here a reduced dielectric constant between silicon and toluene, to account for the liquid medium of embedded colloidal quantum dots.

At low frequency the DOS increases quadratically similar to that of a medium with an effective index of refraction. The DOS deviates from the parabola beyond reduced frequency 0.35, and vanishes between 0.478 and 0.504 in the photonic band gap. Considering the lattice parameter $a = 693$ nm, the band gap is centered around 1400 nm which overlaps with the telecommunication range and avoids the silicon absorption range.

Beside optical characterization of these structures by means of reflectivity experiments [9] our group was the first to control spontaneous emission of quantum emitters in a 3D photonic band gap crystal [11]. Since this early study was limited to a few selected frequencies, in chapter 4 of this thesis we will present the first systematic measurements of controlling spontaneous emission in a finite 3D inverse woodpile photonic crystal. In chapters 6 and 7 we investigate light scattering in 2D silicon photonic crystals.

2.3 Optical properties of PbS quantum dots

In order to probe the density of states inside inverse woodpile photonic crystals we need to infiltrate quantum emitters into the crystals. Since it is fairly challenging to embed efficient emitters in silicon, we have decided to infiltrate emitters only in the low-index medium, which is fortunately the majority of a photonic crystal. Because silicon absorbs light with a photon energy larger than its electronic band gap of about 1.12 eV, corresponding to wavelengths shorter than 1100 nm, it is not possible to use visible-light emitting quantum dots or dye molecules, see *e.g.* [12]. Therefore we have used PbS quantum dots suspended in toluene, purchased from Evident (PbS-1500), that emit in the near infrared wavelength range. For the measurements the quantum dots concentration is reduced to 2×10^{-6} Mol/l to avoid reabsorption of the emitted photons by closely packed quantum dots. From TEM microscopy measurements quantum dots have an average diameter 4.1 nm with standard deviation of 0.5 nm [13].

The absorbance spectrum of quantum dots ensemble has been measured as shown in Fig. 2.2. To measure the absorbance, a beam from a supercontinuum white light source (Fianium) was sent through the suspension of quantum dots with a concentration of 2.10^{-6} Mol/l. The transmitted light is analyzed using a Fourier transform infrared spectroscopy (BioRad FTS-6000) in combination with a pre-amplified InAs photodiode. This setup is used to measure absorption between 4000 and 12000 cm^{-1} corresponding to wavelengths between 830 to 2500 nm. Several faint peaks are seen in the absorbance spectra which correspond to different energy transitions in the quantum dots as indicated in the figure. Every single quantum dot has a set of discrete levels. The energy states of quantum dots are labeled as $1S$, $1P$, $1D$, and so on, similar to atoms and molecules [14, 15]. Similarly, $1S_e$ is the first electron state and $1S_h$ the first hole state, and so forth. The $1S_e - 1S_h$ is the first transition, since it requires the minimum energy. The first seven transitions of PbS quantum dots has been extensively investigated in Ref. [16].

Figure 2.3(a) shows the emission spectrum measured on an ensemble of the

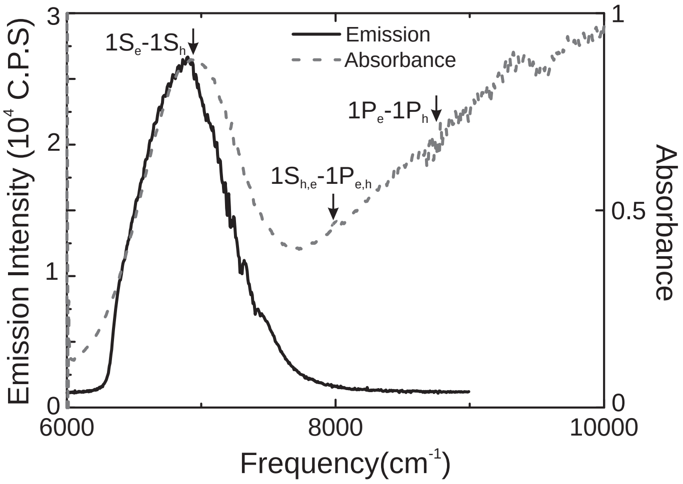

Figure 2.2: Emission (black) and absorbance (dashed gray) spectra of PbS quantum dots suspended in toluene. The emission spectrum is slightly red-shifted with respect to the absorption spectrum corresponding to the Stokes shift.The $1S_e - 1S_h$ is indicating the first transition, $1S_{h,e} - 1P_{e,h}$ the second and $1P_e - 1P_h$ the third transition observed in the absorbance measurements.

PbS quantum dots. It is seen that the spectrum is very broad covering the range between 1300 nm to 1600 nm in the near infrared region, with a peak at 1470 nm ($0.84eV$) with FWHM of 0.086 eV. The broad spectrum of the quantum dots is mostly caused by size polydispersity. The energy gap of the quantum dots is tuned by changing the quantum dot size. Therefore a size distribution of quantum dots leads to a distribution which manifest itself as inhomogeneous broadening in the optical spectra [17]. In a preliminary experiment by Leistikow, the inhomogeneous line broadening of PbS quantum dots by fluorescence line narrowing was measured, suggesting that about half of the linewidth of approximately 70 nm is caused by homogeneous broadening [13]. Intriguingly, our results of frequency dependent decay rate in the band gap in chapter 4 provide evidence for a considerably narrower homogeneous line width: we observe large changes of the decay rate within the band gap at steps of 20 nm suggesting that the homogeneous line broadening is even smaller than 20 nm. Since in our measurements data is collected more systematically and because of sufficient number of data points we think that our results are more reliable than the previous results.

The broad, inhomogeneously broadened, emission spectrum of the PbS quantum dots overlaps very well with the photonic band gap of some of our crystals. This makes it possible to investigate the control of spontaneous emission throughout the band gap (Ch. 4).

In Fig. 2.2 the emission spectrum is plotted together with the absorbance spectrum. As expected the emission spectrum is slightly red-shifted with respect to the main peak of the absorbance spectrum. The red shift of the emission spectra with respect to absorption spectra is known as Stokes shift, which is commonly observed in any florescent molecule and semiconductor quantum dots [18–21].

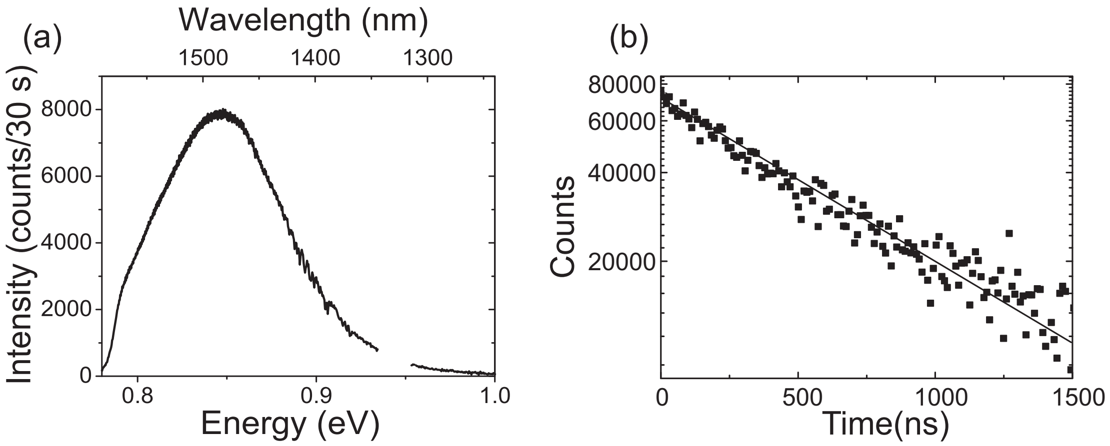

Figure 2.3: (a) Emission spectrum of PbS quantum dot ensemble in toluene. The steep edge at low energy is caused by the cut-off of the detector. The lack of data points around 1 eV is caused by "dead" pixels in the detector [22]. (b) The decay curve of PbS quantum dot ensemble in toluene at λ=1475 nm wavelength. Time resolved emission measurement shows a single exponential decay (black solid line) with a typical decay rate of 1.7 μs^{-1}. Depending on the position of the focus in the suspension the signal level changes and therefore such a time-resolved measurements can take between one to ten minutes.

However, the underlying mechanism of Stokes shift is still controversial. In case of semiconductor quantum dots, this shift decreases with the increase in radius of the dot and disappears beyond a certain radius as reported in Ref. [22] for PbSe quantum dots. The red shift occurs principally if either the top of the valence band is an optically passive state such as a P state, or if the electron and the hole are in a triplet state. Absorption of a photon from the top of the valence band in such cases is not allowed and is possible only from an optically active state lying deeper in the valence band. The exciton, once formed after absorption, can not decay to the top of the valence band by direct dipole transition and hence is called "dark exciton" [18]. Deexcitation eventually takes place with the help of phonons thus giving rise to photons that are red shifted compare to the excitation, as in Fig 2.2 [19, 23, 24].

From Fermi's golden rule applied to spontaneous emission the radiative decay rate of a quantum emitter is modified by the local density of states [12, 25]. Since the emitters in the photonic crystals experience a different LDOS than the one in the suspension, their decay rates change. Hence measuring the decay rate of the emitters in the photonic crystal is a method to probe the LDOS:

$$N_{rad}(\mathbf{r}, \mathbf{e_d}, \omega) = (\frac{\pi d^2 \omega}{\hbar \epsilon_0})^{-1} \gamma_{rad}(\mathbf{r}, \mathbf{e_d}, \omega) \tag{2.1}$$

where $N_{rad}(\mathbf{r}, \mathbf{e_d}, \omega)$ is the projected LDOS and $\gamma_{rad}(\mathbf{r}, \mathbf{e_d}, \omega)$ is the radiative decay rate. For that reason the time-resolved decay rate of the ensemble of quantum dots is extensively studied in this thesis. In time-resolved emission the total decay rate is measured that consists of both radiative and non-radiative decay rate $\gamma_{tot} = \gamma_{rad} + \gamma_{nrad}$. Since only the radiative decay rate is controlled by the LDOS, from our measurements of maximum inhibition in the band gap (discussed in Sec. 4.3) we found the non-radiative decay rate to be at most 5% of the total decay rate, hence $\gamma_{nrad} \leq 0.085 \mu s^{-1}$. An additional consistency check for the LDOS is obtained since the broad quantum dot spectrum allows us to access the long-wavelength limit below the band gap, where the LDOS shows typical quadratic behavior even in a strongly interacting photonic crystal [26]. To compare the LDOS in the crystal with the one in a homogeneous medium, considerable care has to be taken to account for position dependent effects, see notably [27]. This paper shows clearly that even in the long-wavelength limit, the LDOS in the low-index medium in a photonic crystal does not necessarily converge to the LDOS of the low-index medium. This forces to make the choice to normalize the calculated LDOS to bulk toluene or to the low-frequency limit of the DOS of the crystal*. In the calculations done in chapter 4 we have normalized the DOS and the LDOS of photonic crystals to the bulk toluene LDOS.

Figure 2.3(b) shows the decay curve of PbS quantum dots suspended in toluene. Quantum dots are excited by a 532 nm (2.33 eV) wavelength pulsed laser that is at a photon energy much higher than the emission energy of quantum dots. By measuring the time difference between the laser pulse generated by a diode in the laser and the detection pulse of the PMT, we obtain a histogram of the photon arrival times: a decay curve. This method is known as time-correlated single-photon counting (TCSPC) [28]. The decay curve shown here is measured at the peak wavelength of the emission spectrum at 1470 nm. These quantum dots have a typical single exponential decay with a rate of 1.7 μs^{-1} in toluene. The decay rate changes by changing the solvent as reported by different groups [29–31]. This is logical because the surrounding refractive index changes, which modifies the local environment of quantum dots and leads to a different decay rate.

Since we are measuring in the near infrared region the time resolved emission is collected on a huge background level of approximately 3.10^5 dark counts per second [13, 22]. The background must be carefully considered before the time resolved data can be properly interpreted, see Ch. 5. From the TCSPC method to obtain a statistically reliable photon arrival histogram, the repetition rate of the excitation laser must be at least 5 times lower than the decay rate that one wants to measure [28]. This is because after 5 decay times the photon intensity is about 100 times lower than the initial photon intensity, which is considered to have a negligible contribution on the background. Therefore for the experiments performed on photonic crystals in which a 18-fold inhibition occurs, we had to use a low laser repetition rate of 80 kHz, which is the lowest possible repetition rate of our laser. The 18 times inhibition corresponds to a life time of approximately 10 μs. The time between two laser pulses at 80 kHz repetition rate is 12.5 μs which is not 5 times longer than the longest lifetime. Even though this laser repetition rate is technically the longest available at the time of the experiment, the consequence is that we probably statistically bias the photon arrival times histogram to short arrival times and hence, to faster life times.

---

* To be sure, there are infinite long wavelength limit, depending on position, see Fig.7 in Ref. [27]

The number of signal counts is typically 1% of the repetition frequency, or 8.10^3 signal counts per second which is much lower than the background level. To calculate the background level we use 200 bins, with bin size 0.128 ns, that corresponds to about 25 ns before the laser pulse arrives. The statistical analysis of time resolved emission measurements is discussed extensively in chapter 5.

2.4 Experimental setup

Based on the properties of the photonic band gap crystals and the PbS quantum dots, we formulate five main requirements for our optical setup:

1. Capability of doing continuous-wave and time resolved measurements in the near infrared range.
2. Collection and detection in a broad range of wavelengths in near infrared.
3. Possibility of measuring emission, reflection, and transmission in the same setup.
4. Very high resolution microscope in the near infrared regime which resolves a 5 μm photonic crystal.
5. Precise positioning and stability of photonic crystal samples to within 500 nm.

We have built a setup that satisfies all our requirements, as shown schematically in Fig. 2.4. The setup is modification of a setup designed and built earlier by Husken [22]; notably since no cryostat was necessary, the setup could be clearly simplified thus leading to greater stability. A He-Ne laser is used for alignment purposes as well as to excite continuous wave (CW) emission of the quantum dots. A pulsed laser (Time-bandwidth, Cougar) with an emission wavelength of 532 nm and tunable repetition rate is used to excite time-resolved emission of quantum dots. This green 532 nm laser light has a higher photon energy than the quantum dots emission energy where quantum dots absorb this energy. This wavelength is, however, above the band gap of silicon and thus coincides with the high absorption range of the silicon. Fortunately, since quantum dots are within the pores in toluene the laser light that is guided through the pores excites quantum dots. A supercontinuum white light source (Fianium SC-450-2) is also placed in the setup for quantum dot line broadening measurements, reflectivity, and broadband out of plane scattering measurements on photonic crystal samples (chapter 7). For measuring emission of quantum dots in photonic crystals light is focused onto the photonic crystal samples by the illumination objective $o2$ with a numerical aperture NA=0.12. For broadband reflectivity measurements this objective is replaced with a reflective objective with a NA=0.28. For the alignment the illumination objective is placed on a manual three dimensional translational stage with 10 μm resolution.

In order to measure transmission, light is passed through the sample from its backside, by reflecting from $M1$ mirror. Light that emanates from the sample is

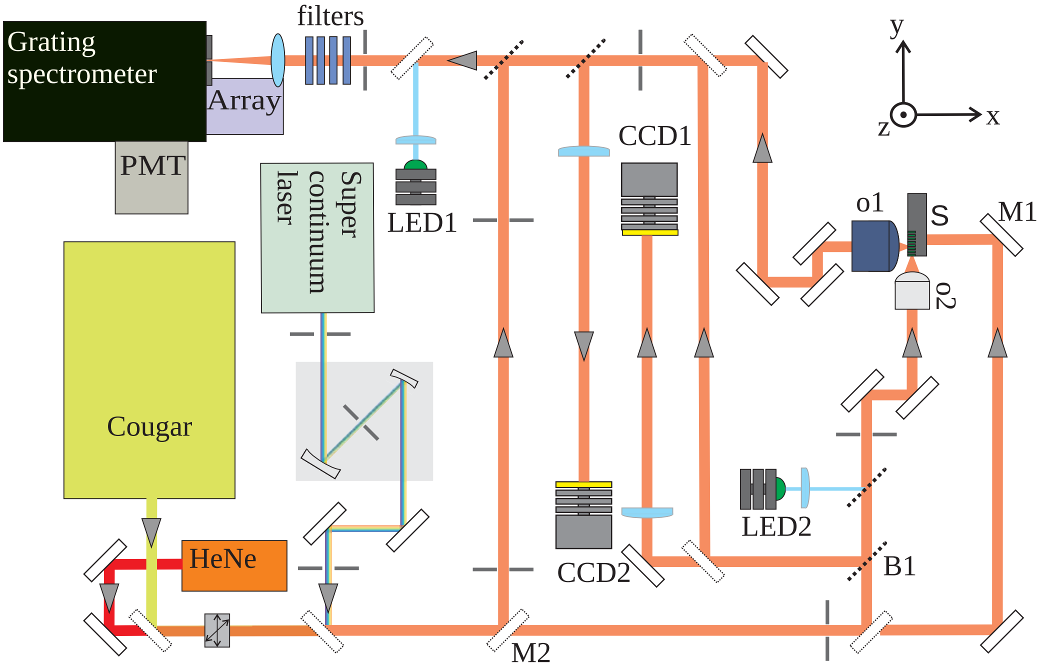

Figure 2.4: Schematic representation of the experimental setup used for the measurements in this thesis. The incident laser light is guided to the illumination objective (*o2*) to be focused on the sample (*S*). The emitted light is collected by a high numerical aperture objective *o1* NA=0.72, then is dispersed by spectrometer. Time resolved emission is detected with a photomultiplier tube (PMT).

collected by a high numerical aperture objective, NA=0.72 (*o1*,Nikon CFIL Plan EPI SLWD). The collection objective is placed under an angle of 90° with respect to the illumination objective to prevent direct reflection of excitation light into the detector in emission experiments. The high NA objective has a relatively large working distance (6 mm) to facilitate the alignment of photonic crystal samples, even in a cuvette. This objective is mounted on three single piezo transducers (PIHera, P-622.Z series) enabling a lateral degree of freedom of 100 μm and 60 μm in the z-direction with a resolution of 0.1 nm and a position accuracy of 0.02 nm [22]. A digital piezo controller (PI-E710) in combination with home-written LabView codes is used to control the position of the collecting objective. The collected light passes through several 850 nm and 1100 nm long pass filters to filter stray laser light in emission experiments. Light is then dispersed by a grating spectrometer(Princeton Instruments, Spectra Pro 2558) with a grating of 85 lines/mm and is imaged into a liquid nitrogen cooled InGaAs diode array (OMA-V: 1024-2.2 LN). The array is sensitive from 1000 to 1650 nm suitable to measure emission spectra. The combination of spectrometer slit size, grating steps and the array's resolution give rise to a step size of 0.08 nm in the spectrum.

Time-resolved emission is detected with a Peltier-cooled Hamamatsu NIR photomultiplier tube (PMT). The selected emission photon energy band width that is detected by the PMT is set by a slit width, and is chosen to be approximately 3 meV. The PMT is connected to a Picoquant PicoHarp 300 timing card. Thus it is possible to measure the decay curve of emitters at particular emission frequencies by the time correlated single photon counting method (TCSPC) [28, 32]. The time resolution is set by the bin size and is 0.128 ns. The PicoHarp 300 is perfectly matched to this detector and the overall Instrument Response Function (IRF) is as short as 40 ps FWHM. Since the quantum dots life time is much longer, the IRF is insignificant.

Alignment of the incident light and the collected light with respect to the sample is realized by implementing two charge couple cameras (CCD 1 and 2) in combination with two single white light emitting diodes (LED 1 and 2). The LEDs are equipped with plano-convex lenses to illuminate the entire aperture of the microscope objectives. Optical images of the surfaces of the sample are collected directing the reflected light of the LEDs to the CCD cameras via pellicle beam splitters and plano-convex lenses. This enables to investigate the position of the incident light on the sample via the illuminating objective, as well as to put the sample in focus with respect to both the illuminating and collecting microscope objectives. The setup scheme is similar to the setup built by Husken [22], except that here we have two separate imaging systems for the illumination path and detection path, for convenient alignment. In this setup we have an additional light path for measuring reflectivity from both sides of the crystal. The first path is from the illumination side. Light illuminates the sample via the illuminating objective *o2* and reflects back from the same objective, after reflecting from beam splitter *B1* is sent to the detector. The second path is via the detection objective, where light that is reflected from the *M2* mirror illuminated the sample and reflects back and is sent to the detector.

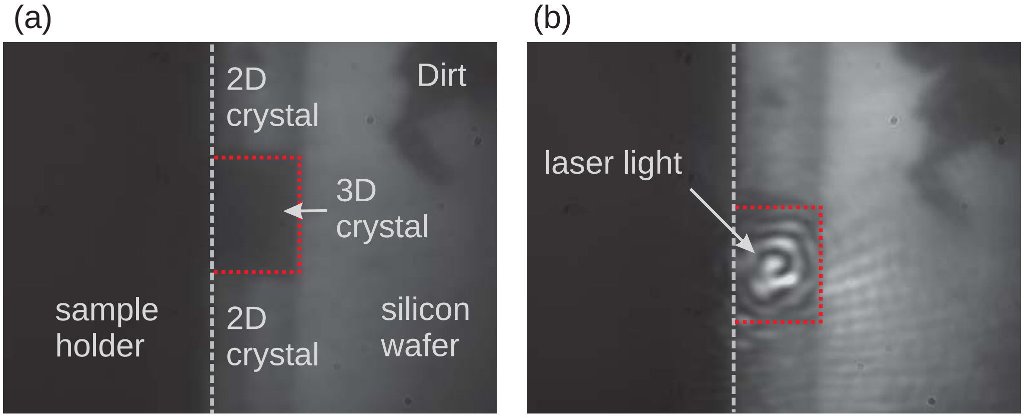

Figure 2.5: CCD camera image of a 3D photonic crystal (internal name: Ad3b-14112008) in a cuvette filled with toluene in the near infrared setup with white light illumination. (a) The 3D photonic crystal is indicated with a dashed red rectangle. The 3D crystal is surrounded with 2D crsyals in the vertical direction along the dashed gray bar. The pitch of the pores is 0.69 ± 0.02 μm. The dark spot on the silicon wafer is dirt that has stuck to the wafer during sample fabrication. The image shows that the spatial resolution is sufficient to image 3D photonic crystals. (b) Result of a successful alignment procedure on a 3D photonic crystal. The laser light is focused in the middle of the 3D crystal. Since the crystal is in a cuvette, the resolution is slightly worse than what is expected.

Figure 2.5 shows a white light image of the side view of a sample that contains both 2D and 3D crystals in the setup. The gray bar along the dashed line is the 2D crystal that surrounds the 3D crystal. The pores of the 2D crystal are along the horizontal direction. The dark gray rectangle in the middle is the 3D photonic crystal. Figure 2.5(b) is a white light image of the same sample during the alignment procedure on the 3D photonic crystal. The laser light is focused in the middle of the 3D crystal. These images show that the spatial resolution of the setup is high enough to resolve a 3D crystal with a lateral length of 5 μm, which therefore meets the requirement for successful studies.

2.5 Summary

In this chapter we describe the infrastructure to study inhibition of spontaneous emission in 3D photonic band gap silicon inverse woodpile photonic crystals. These crystals have a 3D extent in all three dimensions by etching perpendicular sets of pores in two directions. The crystals have the widest ever photonic band gap in the near infrared, confirmed with reflectivity and emission measurements. In order to probe the density of states in the band gap of the photonic crystals we infiltrate PbS quantum dots in the crystals pores. The broad emission spectrum of the PbS quantum dots overlaps very well with the photonic band gap of our crystals.

We describe the near infrared emission setup that is used for most of the experiments in this thesis. This setup includes optical paths for emission measurements, transmission, and reflection measurements in the near infrared range. The absorbance spectrum of quantum dots is measured by exciting quantum dots with a white light source, showing different transitions in quantum dots energy levels. Comparing the emission and the absorbance spectra we observe a Stokes shift. The decay rate of quantum dots shows a decay rate of 1.7 μs^{-1} at the peak of emission spectrum, in agreement with the decay rate reported from other studies in literature.

Bibliography

[1] K. M. Ho, C. T. Chan, C. M. Soukoulis, R. Biswas, and M. Sigalas, *Photonic band gaps in three dimensions: new layer-by-layer periodic structures*, Solid State Commun. **89**, 413 (1994). — p.27.

[2] R. Hillebrand, S. Senz, W. Hergert, and U. Gösele, *Macroporous-silicon-based three-dimensional photonic crystal with a large complete band gap*, Journal of applied physics **94**, 2758 (2003). — p.27.

[3] L. A. Woldering, A. P. Mosk, R. W. Tjerkstra, and W. L. Vos, *The influence of fabrication deviations on the photonic band gap of three-dimensional inverse woodpile nanostructures*, J. Appl. Phys. **105**, 093108 (2009). — p.27.

[4] S. G. Johnson and J. D. Joannopoulos, *Block-iterative frequency-domain methods for maxwells equations in a planewave basis*, Opt. Express **8**, 173 (2001). — p.28.

[5] J. M. van den Broek, L. A. Woldering, R. W. Tjerkstra, F. B. Segerink, I. D. Setija, and W. L. Vos, *Inverse-woodpile photonic band gap crystals with a cubic diamond-like structure made from single-crystalline silicon*, Adv. Funct. Mater. **22**, 25 (2012). — p.27.

[6] R. W. Tjerkstra, L. A. Woldering, J. M. van den Broek, F. Roozeboom, I. D. Setija, and W. L. Vos, *Method to pattern etch masks in two inclined planes for three-dimensional nano- and microfabrication*, J. Vac. Sci. Technol. B **29**, 061604 (2011). — p.27.

[7] S. Y. Lin and G. Arjavalingam, *Tunneling of electromagnetic waves in two-dimensional photonic crystals*, Opt. Lett. **18**, 1666 (1993). — p.28.

[8] J. Huang, N. Eradat, M. E. Raikh, Z. V. Vardeny, A. A. Zakhidov, and R. H. Baughman, *Anomalous coherent backscattering of light from opal photonic crystals*, Phys. Rev. Lett. **86**, 4815 (2001). — p.28.

[9] S. R. Huisman, R. Nair, L. A. Woldering, M. D. Leistikow, A. P. Mosk, and W. L. Vos, *Signature of a three-dimensional photonic band gap observed on silicon inverse woodpile photonic crystals*, Phys. Rev. B **83**, 205313 (2011). — p.28, 29.

[10] W. L. Vos, R. Sprik, A. van Blaaderen, A. Imhof, A. Lagendijk, and G. H. Wegdam, *Strong effects of photonic band structures on the diffraction of colloidal crystals*, Phys. Rev. B **53**, 16231 (1996). — p.28.

[11] M. D. Leistikow, A. P. Mosk, E. Yeganegi, S. R. Huisman, A. Lagendijk, and W. L. Vos, *Inhibited spontaneous emission of quantum dots observed in a 3D photonic band gap*, Phys. Rev. Lett. **107**, 193903 (2011). — p.29.

[12] L. Novotny and B. Hecht, *Principles of nano-optics* (Cambridge University Press, New York, 2006). — p.29, 31.

[13] M. D. Leistikow, *Controlling spontaneous emission with nanostructures*, PhD Thesis, University of Twente, 2010. — p.29, 30, 32.

[14] A. L. Efros and A. L. Efros, *Interband absorption of light in a semiconductor sphere*, Sov. Phys. Semicond **16**, 772 (1982). — p.29.

[15] A. I. Ekimov and A. A. Onushchenko, *Size quantization of the electron energy spectrum in a microscopic semiconductor crystal*, JEPT Lett **40**, 1136 (1984). — p.29.

[16] L. Cademartiri, E. Montanari, G. Calestani, A. Migliori, A. Guagliardi, and G. A. Ozin, *Size-dependent extinction coefficients of PbS quantum dots.*, J. Am. Chem. Soc **128**, 10337 (2006). — p.29.

[17] V. I. Klimov, *Nanocrystal quantum dots* (CRC Press Boca Raton, FL, 2010). — p.30.

[18] M. Nirmal, D. J. Norris, M. Kuno, M. G. Bawendi, A. L. Efros, and M. Rosen, *Observation of the "dark exciton" in cdse quantum dots*, Phys. Rev. Lett. **75**, 3728 (1995). — p.30, 31.

[19] A. L. Efros, M. Rosen, M. Kuno, M. Nirmal, D. J. Norris, and M. Bawendi, *Band-edge exciton in quantum dots of semiconductors with a degenerate valence band: Dark and bright exciton states*, Phys. Rev. B **54**, 4843 (1996). — p.30, 31.

[20] M. Paillard, X. Marie, P. Renucci, T. Amand, A. Jbeli, and J. M. Gérard, *Spin relaxation quenching in semiconductor quantum dots*, Physical review

letters **86**, 1634 (2001). — p.30.

[21] A. Tackeuchi, R. Ohtsubo, K. Yamaguchi, M. Murayama, T. Kitamura, T. Kuroda, and T. Takagahara, *Spin relaxation dynamics in highly uniform inas quantum dots*, Applied physics letters **84**, 3576 (2004). — p.30.

[22] B. H. Husken, *Spontaneous emission of near-infrared quantum dots controlled with photonic crystals*, PhD Thesis, University of Twente, 2009. — p.31, 32, 33, 34, 35.

[23] J. Li and J.-B. Xia, *Exciton states and optical spectra in cdse nanocrystallite quantum dots*, Phys. Rev. B **61**, 15880 (2000). — p.31.

[24] A. Bagga, P. K. Chattopadhyay, and S. Ghosh, *Origin of stokes shift in inas and cdse quantum dots: Exchange splitting of excitonic states*, Phys. Rev. B **74**, 035341 (2006). — p.31.

[25] R. Sprik, B. A. van Tiggelen, and A. Lagendijk, *Optical emission in periodic dielectrics*, Europhys. Lett. **35**, 265 (1996). — p.31.

[26] A. F. Koenderink, L. Bechger, A. Lagendijk, and W. L. Vos, *An experimental study of strongly modified emission in inverse opal photonic crystals*, Phys. Stat. Sol. B **197**, 648 (2003). — p.32.

[27] I. S. Nikolaev, W. L. Vos, and A. F. Koenderink, *Accurate calculation of the local density of optical states in inverse-opal photonic crystals*, J. Opt. Soc. Am. B **26**, 987 (2009). — p.32.

[28] D. V. O'Connor, W. R. Ware, and J. C. Andre, *Deconvolution of fluorescence decay curves. a critical comparison of techniques*, J. Phys.l Chem. **83**, 1333 (1979). — p.32, 35.

[29] S. W. Clark, J. M. Harbold, and F. W. Wise, *Resonant energy transfer in pbs quantum dots*, The Journal of Physical Chemistry C **111**, 7302 (2007). — p.32.

[30] M. S. Gaponenko, A. A. Lutich, N. A. Tolstik, A. A. Onushchenko, A. M. Malyarevich, E. P. Petrov, and K. V. Yumashev, *Temperature-dependent photoluminescence of pbs quantum dots in glass: Evidence of exciton state splitting and carrier trapping*, Phys. Rev. B **82**, 125320 (2010). — p.32.

[31] Y. Chen, D. Yu, B. Li, X. Chen, Y. Dong, and M. Zhang, *Size-dependent radiative emission of pbs quantum dots embedded in nafion membrane*, Applied Physics B **95**, 173 (2009). — p.32.

[32] D. V. O'Connor and D. Philips, *Time correlated single photon counting* (Academic Press, 1984). — p.35.

CHAPTER 3

Local density of states in the band gap of a finite one-dimensional photonic crystal

3.1 Introduction

Recently, there have been great attempts to make 3D photonic band gap crystals which show a 3D photonic band gap [1–11]. In practice a real photonic crystal is of course always finite. Therefore the DOS, that is an average over all of space, can not describe the optical states in a *finite* system. For an inhomogeneous system, including finite crystals we need to take into account local properties and therefore we need to calculate the local density of states (LDOS). Having a finite crystal fundamentally changes the main features of the LDOS. First of all the LDOS that is zero in the band gap of an infinite crystal [12, 13], becomes non-zero in the band gap of a finite crystal [14, 15]. Moreover, within the bandgap of an infinite crystal the LDOS does not depend on frequency or position; in stark contrast in the bandgap of a finite crystal the LDOS does depend on frequency, position, and the crystal size. To date, most theories assume crystals of infinite extent (see Refs. [12, 13, 16, 17] and references therein), and can thus not be used to interpret experimental results on real crystals as first studied in Ref. [14]. To the best of our knowledge the LDOS in the band gap of a finite 3D photonic crystal has not been studied yet as a function of the crystal size and the position in the crystal and there is no analytic theory to calculate the LDOS for any class of crystal. Several groups have calculated optical properties of finite bandgap crystals: Interesting work has been done to calculate the DOS (but not the LDOS) for 1D-waves in the band gap of a finite 1D crystal by Bendickson *et al.* [18]. The LDOS for 2D waves has been calculated in the band gap of a 2D photonic crystals by Asatryan *et al.* as a function of position, crystal size, and frequency [19]. The 3D LDOS has been calculated for 1D and 2D crystals that do not have a 3D gap [15, 20, 21]. For 3D light in a 3D inverse opal, Hermann and Hess have calculated the LDOS as a function of frequency, position, and for several position in the crystal by means of finite difference time domain simulations [22]. Unfortunately, however, the results can not be applied to other crystals, physical insights are not readily apparent, as is intrinsic to

---

This chapter has been published as: E. Yeganegi, A. Lagendijk, A.P. Mosk, and W. L. Vos, Phys. Rev. B **89**, 045123: 1-10 (2014) simulations, and finally such calculations requires a lot of programming efforts and computational costs.

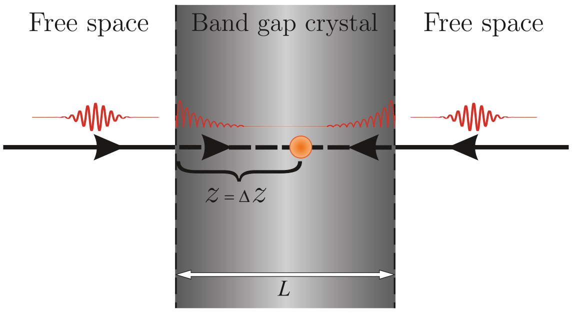

Figure 3.1: (color) Schematic drawing of a light source (orange sphere) embedded in a finite (1D) photonic band gap crystal with the size L (photonic crystal slab). The source is located at a depth $z = \Delta z$. The interface between the crystal and free space is indicated by the vertical dashed line. The shading in the crystal lightens away from the interface to illustrate the decreasing LDOS with depth into the crystal Δz.

In this chapter we introduce a new point of view on the band gap in a finite photonic crystal, which allows for simplified calculations based on physical principles. We consider a photonic band gap in a finite crystal to be the result of vacuum fluctuations in free space that tunnel into the forbidden zone where the fluctuations are exponentially damped. The physical situation is illustrated in Fig. 3.1 where a light source (orange circle) is embedded in a finite photonic band gap crystal. In this paper we will limit ourselves to a 1D structure. The reason is that the electromagnetic field propagation and the band structure in 1D can be calculated analytically, therefore we can test our model by comparing with the analytic calculations. Ultimately our model is intended to be extended to calculate the DOS inside the band gap of a finite 2 or 3-dimensional photonic crystal as a function of crystal size, and frequency, which is the subject of chapter 4.

3.2 Local density of states in a finite crystal

The local density of states (LDOS) projected on the transition dipole moment orientation in an infinite photonic crystal $N(\mathbf{r}, \omega, \mathbf{e}_d)$ is conveniently calculated as a sum over all modes [23–25]:

$$N(\omega, \mathbf{r}, \mathbf{e}_d) = \frac{1}{(2\pi)^3} \sum_n \int_{BZ} d\mathbf{K} \delta(\omega - \omega_{n,\mathbf{K}}) |\mathbf{e}_d \cdot \mathbf{E}_{n,\mathbf{K}}(\mathbf{r})|^2, \tag{3.1}$$

where ω is frequency, $\mathbf{r}$ is position in the crystal, and $\mathbf{e}_d$ is the dipole moment orientation. The integration over the real wave vector $\mathbf{K}$ is performed over the first Brillouin zone, and n is the band index. $\mathbf{E}_{n,\mathbf{K}}(\mathbf{r})$ is the mode function of the (quantized) electromagnetic field. In a photonic crystal these mode functions are Bloch modes equal to:

$$\mathbf{E}_{n,\mathbf{K}}(\mathbf{r}) = \bar{\mathbf{E}}_{n,\mathbf{K}}(\mathbf{r}) e^{-i\mathbf{K}.\mathbf{r}}. \tag{3.2}$$

where $\bar{\mathbf{E}}_{n,\mathbf{K}}$ has the periodicity of the unit cell. The physical interpretation of Eq. (3.1) is that the delta function $\delta(\omega - \omega_{n,\mathbf{K}})$ filters the relevant emission frequency from the collection of photonic states. Since in the band gap of an infinite crystal there are no propagating modes, the delta function causes the projected LDOS to become zero in this frequency range. We use a vector notation for $\mathbf{K}$ and $\mathbf{r}$ to enable the generalization to 2D and 3D.

To calculate the LDOS for a finite photonic crystal we modify the LDOS equation for an infinite photonic crystal. We develop a model for the LDOS in a finite crystal which concerns the fields $\mathbf{E}_{n,\mathbf{K}}(\mathbf{r})$ and the modes' linewidths to generalize the δ-function in Eq. 3.1, which are the two main factors in the LDOS. We propose that fields in the band gap can be calculated using our Ansatz as follows: in the gap the fields are interpolated between the allowed Bloch modes at the band edges that are frequency broadened by finite size and that are multiplied by a frequency dependent exponentially decaying term that describes tunneling. This model describes that at a depth z inside a finite photonic band gap crystal the vacuum modes that enter the crystal in a certain direction $\mathbf{K}$ are exponentially damped. The second factor is about the modes in the finite crystal. Modes in a finite crystals are no more delta functions and become broadened due to the finite size of the crystal. We propose to employ Lorentzian functions instead of the delta functions, where the linewidth of the Lorentzian is set by the crystal size L. These assumptions are used to calculate LDOS in the band gap of 1D photonic crystal as a function of frequency, depth in the crystal, and the crystal size.

In this chapter we describe in detail the above-mentioned viewpoint. In Sec. 3.3.1 we review analytic calculations of the field in a periodic medium. We start with a crystal of infinite extent as is illustrated in Fig. 3.2(a) and we describe Bloch modes as function of frequency and position in the crystal. We also describe the band structure of an infinite 1D photonic crystal in an intuitive way. In Sec. 3.3.2 we discuss the field behavior in a finite crystal as a function of frequency, the position and the crystal size. In Sec. 3.4 we describe our model for the LDOS in a finite crystal. In Sec. 3.5 we check our model by calculating the LDOS in the bandgap of a finite photonic crystal using the model and comparing that with the analytically calculated LDOS in the bandgap of a finite 1D crystal. Finally, in Sec. 3.6 we summarize our findings.

3.3 Field propagation in a periodic media

3.3.1 Infinitely extended photonic crystal

In this section we investigate the optical properties of an infinitely extended 1D periodic structure as shown in Fig. 3.2(a). To calculate the band structure and the electromagnetic fields we use the transfer matrix method. The details are available in the appendix A.

In Fig. 3.3 we plot the band structure for a crystal with alternating dielectric constants of $\epsilon_1 = 13$ and $\epsilon_2 = 1$ and layer thicknesses $a_1 = 0.2a$ and $a_2 = 0.8a$. We used $\epsilon_1 = 13$ as an approximation relevant to commonly used semiconductors

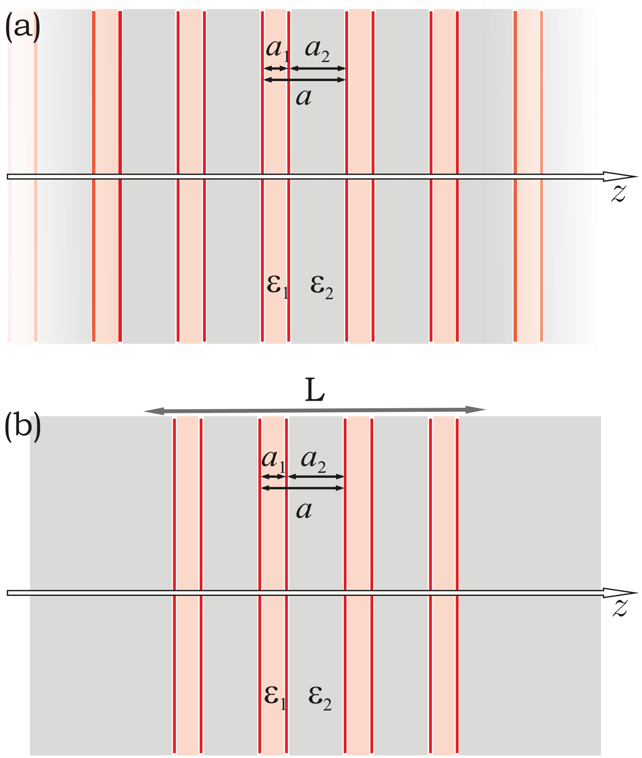

Figure 3.2: Schematic drawing of a one-dimensional periodic structure. (a) Infinite structure and (b) finite Bragg stack. One period, a, consists of two different media with width "a_1" and "a_2" and dielectric permittivities of ϵ_1 and ϵ_2 respectively. The crystal is taken to be one-dimensional and the other directions are used for illustration purposes.

such as GaAs and Si. Within the bands $\mathbf{K}$ is real corresponding to the propagating Bloch modes. In the stopgap, however, $\mathbf{K}$ becomes complex $\mathbf{K} = \mathbf{K}^{'} + i\mathbf{K}^{''}$ and therefore light is attenuated in the crystal. In this case the real part of the wave vector is clamped at the Brillouin zone edge $K^{'} = \pi/a$ [26]. Simultaneously the imaginary part strongly depends on frequency $\mathbf{K}^{''} = \mathbf{K}^{''}(\omega)$, as it increases from zero to a maximum at the stop gap center back to zero at the upper stopgap edge. Interestingly such a complex band structure has previously been considered for both photonic and phononic crystal structures [27, 28].
Fig. 3.4 (a) shows the calculated absolute value of the field $|\mathbf{E}_{n,\mathbf{K}}(z)|$ in the first band at a reduced frequency $\omega a/2\pi c = 0.2$. It is seen that the field maxima are located in the material with the high dielectric permittivity. This general and well-known behavior occurs at all frequencies in the first band up to the band edge at $\omega a/2\pi c = 0.203$ [26, 29] . If we assume light to be inside such an infinite structure at frequencies in the band gap, the field is exponentially damped since the incident light is reflected from each layer due to Bragg diffraction. Fig. 3.4(b) and (c) show fields at two different frequencies in the band gap, where Fig. 3.4(b) is for a frequency near the center of the band gap and Fig. 3.4(c) corresponds to a frequency close to the band edge where the imaginary part K'' of the wave vector is much smaller than at the center of the gap. Fig. 3.4 (d) shows the field

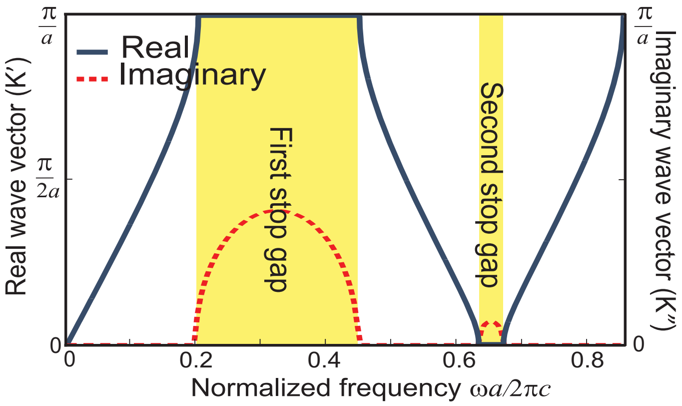

Figure 3.3: Calculated exact band structure of the one-dimensional periodic structure depicted at Fig. 3.2, where $a_1 = 0.2a$ and $a_2 = 0.8a$ and ϵ_1 and ϵ_2 are 13 and 1 respectively. The bands are shown with dark blue lines where the wave vector is real (left ordinate). The first two photonic bandgaps are shown with yellow bars. In the band gaps the wave vector becomes complex $\mathbf{K} = \mathbf{K}^{'} + i\mathbf{K}^{''}$, where the real part is clamped at the Brillouin zone edge wave vector ($K^{'} = \pi/a$) and the imaginary part $K^{''}$ strongly depends on the frequency as is shown by red dashed line (right ordinate).

at a frequency in the second band where field propagates in the structure and the field maxima are located in the material with low ϵ, in agreement with common lore for "*air bands*" [29, 30].

Now we turn to the field behavior as a function of frequency and position in the periodic structure. To build the model for the LDOS in a finite crystal we consider the main maximum of the field amplitude for different frequencies inside and outside the band gap. Fig. 3.5(a) shows the position of the field maximum within a unit cell as a function of normalized frequency. The ordinate between 0 and 0.2 is the high index material and from 0.2 to 1 is the low index material. The abscissa shows the frequency range, which includes the first and second band and the first band gap which is indicated with the yellow bar. In the first band the field maximum is in the middle of the high index material. In the second band the field maximum is in the middle of the low index material. This field behavior for propagating bands is well-known and corresponds to the dielectric band and air band nomenclature that pertains to a simple photonic crystal, see Ref [29]. In the band gap, however, the field maximum moves continuously from the middle of the high index layer to the middle of the low index material. It is seen in Fig. 3.5(a) that this trend through the unit cell is a complex function of frequency. From separate calculations we find that the path is a complicated function of a_1, a_2, ϵ_1 and ϵ_2. In the band gap, the field amplitude $|\mathbf{E}_{n,\mathbf{K}}(z)|$ does not fulfill the symmetry of the crystal any more – here in 1D mirror symmetry at the center of either layer 1 or layer 2 – since the fields are no more *bonafide* eigenfunctions of the crystal. The trajectory of the field maximum through the unit cell is a phenomenon known in X-ray literature, where it is used in X-ray fluorescence standing wave spectroscopy [31].

Fig. 3.5(b) shows the maximum field amplitude as a function of frequency.

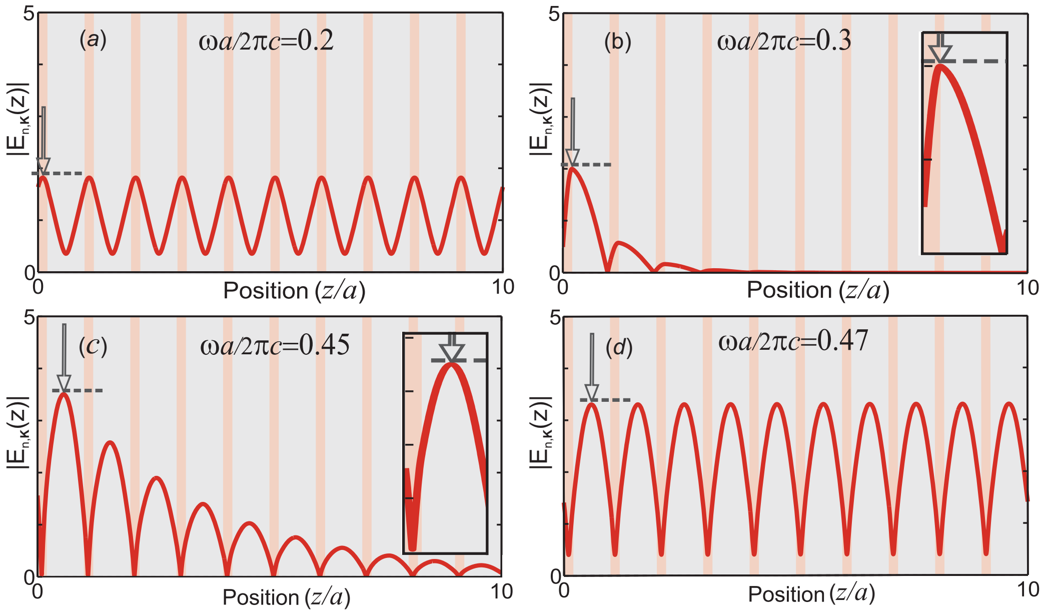

Figure 3.4: Absolute value of the electric field associated with (a) reduced frequency $\omega a/2\pi c = 0.2$, (b) reduced frequency $\omega a/2\pi c = 0.3$, (c) reduced frequency $\omega a/2\pi c = 0.45$, and (d) reduced frequency $\omega a/2\pi c = 0.47$ of the band structure plotted in the Fig. 3.3. The main maximum of the field amplitude is indicated in Fig. 3.4 with a black arrow.

In the first band the field amplitude maximum increases with frequency until it reaches the lower edge of the band gap. While the trend of the field maximum is continuous in moving from the first band to the band gap and then to the second propagating bands, there is a cusp at each band edge. At the frequency of the upper band edge the field amplitude is enhanced. The maximum of the field amplitude in the second band is higher compared to the first band. This enhancement can be understood from the conservation of field energy $|\epsilon \mathbf{E}_{n,\mathbf{K}}(z)^2|$, since the field maximum in the second band is centered in the low index material. This detailed investigation of the field behavior in the band gap suggests a relation between the fields in the gap and the fields at the band edges.

3.3.2 Finite photonic crystal

The advantage of a 1D calculation is that analytic calculations of the field and of the LDOS for a finite crystal is possible. In this section we calculate the field and the projected LDOS for a finite periodic structure that has the same periodicity and dielectric materials as the infinite one. We first calculate the field at different frequencies outside and inside the band gap and then using these fields we calculate the projected LDOS inside the band gap of a finite structure. Later on in Sec.3.5 we compare the LDOS calculated using our model with the exact LDOS calculated using a transfer matrix method.

To calculate the field in a finite structure we also use a transfer matrix method where the propagating fields are the total electric field and the total magnetic

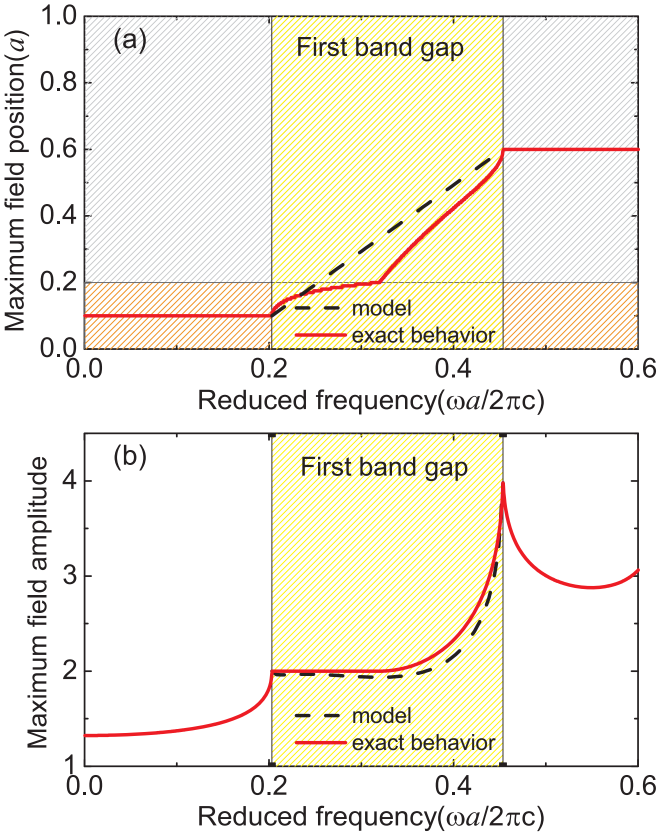

Figure 3.5: (a)Behavior of the first field maximum in the frequency range of the first bandgap. The ordinate between 0 and 0.2 is the high index material (indicated by the orange hatched bar) and from 0.2 to 1 is the low index material (indicated by the gray hatched bar). The red solid line is the exact behavior of the field and the black dashed line is the linear field interpolation with the position. (b) Comparison of the exact maximum field amplitude (red curve) and the model (black dashed curve) as a function of reduced frequency. In the model a linear interpolation is used for the position of the field maximum (see(a)). The model shows a very good agreement with the exact calculations.

field. The main difference between the calculations in a finite and infinite structure is that in the infinite structure fields are Bloch modes and therefore we have to apply an extra condition to imply field periodicity as a result of Bloch conditions. This reduces the number of initial conditions for the wave that propagates into the crystal. In case of the finite structure, the Bloch condition does not pertain once we have the freedom to choose any arbitrary initial conditions. If we take as an initial condition the incident wave $\left(1\ 0\right)^T$ (see Appendix A), the wave on the left side will be $\left(1\ r\right)^T$ and the wave on the right side $\left(t\ 0\right)^T$, where r and t are the amplitude transmission and reflection coefficients. The wave $\left(1\ r\right)^T$ contains both the reflection that is a property of the crystal and the incident wave that is not a property of the crystal. On the other hand, the right side wave $\left(t\ 0\right)^T$ only contains a property of the crystal. Since we wish to obtain properties of the crystal, we prefer to start with the wave $\begin{pmatrix} t & 0 \end{pmatrix}^T$ and propagate it backwards through the crystal. An advantage of this approach is that we minimize rounding errors when Bragg reflection occurs. If one would start from the left such errors appear especially when the structure becomes larger, leading to a non-physical solution. From scattering theory [32, 33], this result can be understood as follows: there are no bound states inside the crystal in the gap, therefore, all scattering states outside the crystal such as $\begin{pmatrix} t & 0 \end{pmatrix}^T$ form a complete set that characterize the crystals properties.

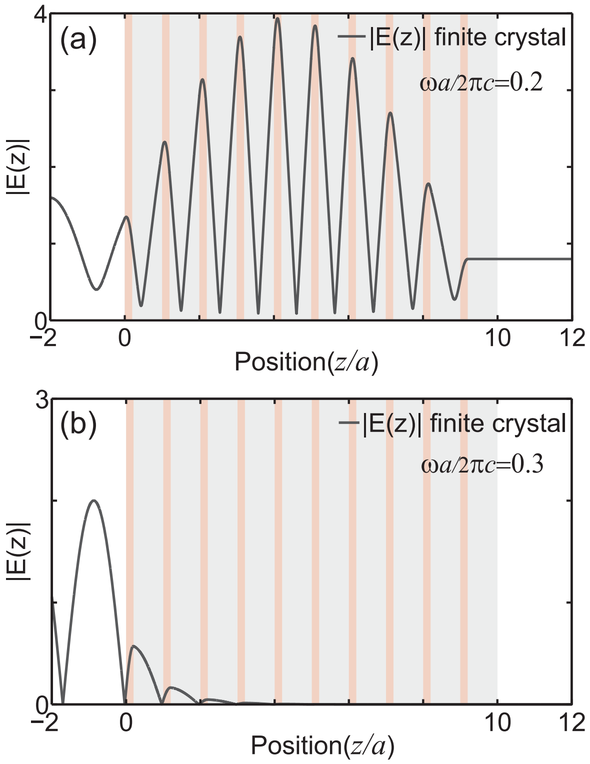

Figure 3.6: (a) Absolute value of the electric field at a frequency $\omega a/2\pi c = 0.2$ for a finite structure with $m = 10$ periods. The environment of the crystal is assumed to be air. (b) Absolute value of the electric field at a frequency $\omega a/2\pi c = 0.3$ inside the photonic band gap (see Fig. 3.3). At this frequency the field inside the structure is damped. The field in the finite structure decays with the same damping as the field in the infinite structure at the same frequency.

Fig. 3.6(a) shows the exact analytic calculations of the absolute field for a finite crystal consists of $m = 10$ layers. The environment is assumed to be free space. At a reduced frequency $\omega a/2\pi c = 0.2$ outside the band gap, the field is propagating through the crystal. As seen in the figure the field is not periodic and clearly differs from the field in the infinite structure at the same frequency (see Fig. 3.4) as a result of Fabry-Perot resonances due to the front and back surfaces. Fig. 3.6(b) shows the electric field for the same structure at a reduced frequency $\omega a/2\pi c = 0.3$. This frequency is in the band gap and here the field is damped. In the finite structure the field is damped with the same decay length as the field in the infinite structure at the same frequency, as is expected.

To calculate the LDOS we have calculated the field entering the crystal from *both* sides. Since the dipole orientation of the light source is in the direction of the field propagation, the intensity of the light entering the crystal is directly proportional to the projected LDOS. In Fig. 3.7 we show the calculated LDOS in the band gap of the finite crystal. The crystal has a larger size of $m = 20$ unit cells and has the same dielectric constants and layer thicknesses as before. We also calculate the LDOS using the Green function where we assume that the emitter is at position (z) in a host layer [34, 35] . The Green function can be solved self-consistently at any position in the structure. The imaginary part of the Green function leads to the LDOS that is shown in Fig. 3.7 by green dot-dashed line [34], which agrees well with the LDOS calculation using the field. It is seen that in the band gap the LDOS decreases exponentially with depth z in the crystal. At a frequency near the center of the bandgap as in Fig. 3.7(a) the LDOS decays faster compared to a frequency closer to the band edge as in Fig. 3.7(b), as is expected due to the smaller magnitude of the imaginary wave vector $\mathbf{K}''$ near the edge (see Fig.3.3). The LDOS behavior in the band gap will be discussed in more detail in Sec. 3.5.

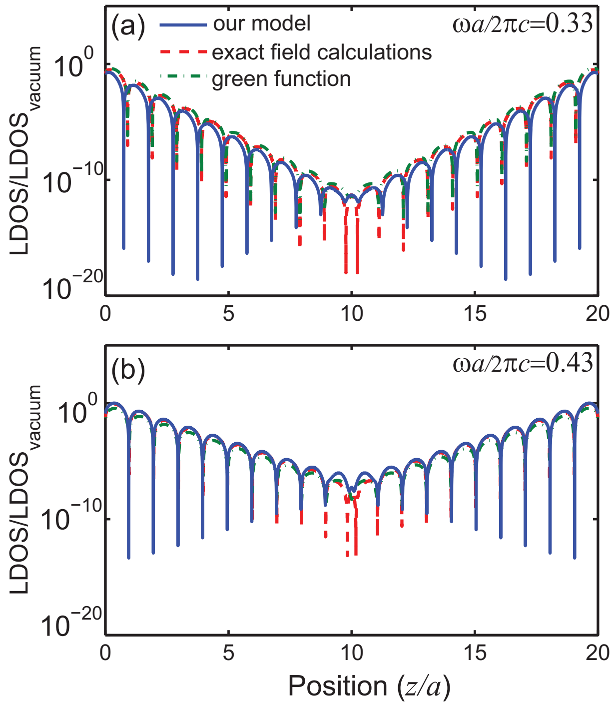

Figure 3.7: (color) The LDOS calculated using the Ansatz Eq. 3.5 (blue) and the exact LDOS calculated for a finite periodic structure at two different reduced frequencies $\omega a/2\pi c = 0.33$ and $\omega a/2\pi c = 0.43$ within the photonic bandgap (logarithmic axis). At frequency $\omega a/2\pi c = 0.33$ there is a small shift in the unitcell modulations of the LDOS. At frequency $\omega a/2\pi c = 0.43$ our model matches perfectly with the exact calculation. This small deviation between our model (blue curve) and the exact calculations of the LDOS using the field (red curve) and the Green function (green curve) is due to our simple interpolation and can be already seen in 3.5(b) at the same frequency.

3.4 Model for the LDOS in a finite crystal

To calculate the LDOS in the band gap of a finite crystal we implement our new point of view which consists of two main items. *First*, in a finite crystal the propagating modes are not strictly Bloch modes as in an infinite crystal. If we consider the Green function, it can be expanded in eigenfunctions $\mathbf{E}_{n,\mathbf{K}}(\mathbf{r})$ of the crystal as for an infinite crystal [36]:

$$\overleftrightarrow{G}(\mathbf{r},\mathbf{r}^{'};\omega) = \lim_{\epsilon\to 0}\sum_{\mathbf{K}} \frac{c^2\mathbf{E}^*_{n,\mathbf{K}}(\mathbf{r}^{'})\mathbf{E}_{n,\mathbf{K}}(\mathbf{r})}{\omega^2_{\mathbf{K}} - (\omega+i\epsilon)^2},$$

where we sum over all wave vectors $\mathbf{K}$ in all bands. In the case of a finite crystal the eigen functions become quasi modes that obey a bi-orthogonality condition [37]. Therefore we can write the same summation for the Green function in a finite system knowing that such quasi modes have a finite width. The width of these quasi modes can be determined by considering constant-flux modes [38]. A simple yet insightful approximation, inspired by the scaling theory of localization, is to determine the width by the time required for the wave to propagate out of the crystal [39]. If we consider the eigenfunctions $\mathbf{E}$ to have an amplitude of order one, the summation contains Lorentzian functions, therefore, we propose the finite crystal modes to be Lorentzians. $F(\omega - \omega_{i,j})$ describes how modes broaden in frequency due to the finite size of the crystal

$$F(\omega - \omega_{i,j}) = \frac{1}{(2\pi)}\frac{\Delta}{(\frac{\Delta}{2})^2 + (\omega - \omega_{i,j})^2}, \tag{3.3}$$

where Δ is the width of the Lorentzians. As a first step we take the width to be the same for every mode. We take the width to be equal to the ratio of the lattice parameter to the crystal size L [41]

$$\Delta = \frac{a}{L}. \tag{3.4}$$

Due to the finite size of the crystal the modes become discrete [40] and we have a summation of the Lorentzian modes. $\omega_{i,j}$ is the central frequency of each mode and therefore the central frequency of each Lorentzian function. m is the number of wave vectors in the Brillouin zone that is equal to the number of the unit cells in the finite crystal, which stems from the Born-Von Karman boundary condition in solid state physics [40]. L is the crystal size that is equal to $L = m{\cdot}a$. The number of Lorentzian functions is thus set by the number of modes in the finite crystal and is therefore equal to m for each band. The expression for the Lorentzian functions $F(\omega - \omega_{i,j})$ leads to delta functions in the limit of an infinitely large crystal ($L \longrightarrow \infty$), in agreement with Eq. 3.1.

The *second* item describes the waves in the band gap. To calculate the waves in the band gap we use two features: the Bloch modes at the edges of the band gap, and the imaginary part of the wave vector $\mathbf{K}''$. As we have seen in Sec. 3.3, in the bands at frequencies below and above the gap the wave vectors are completely real: $\mathbf{K} = \mathbf{K}'$ and $\mathbf{K}'' = 0$ and the waves are propagating. In the bandgap the wave vectors become complex $\mathbf{K} = \mathbf{K}' + i\mathbf{K}''$ thus the waves are exponentially damped as a result of Bragg diffraction. Here we apply our second new point of view to the waves in the band gap. We propose to write the waves in the bandgap as a Bloch function with a complex wave vector as follows:

$$\begin{aligned} \mathbf{E}^{pbg}_{\mathbf{K}}(\mathbf{r}) &= \bar{\mathbf{E}}_{\mathbf{K}}(\mathbf{r})e^{i\mathbf{K}\cdot\mathbf{r}} \\ &= \bar{\mathbf{E}}_{\mathbf{K}}(\mathbf{r})e^{i(\mathbf{K}'+i\mathbf{K}'')\cdot\mathbf{r}} \\ &= \bar{\mathbf{E}}_{\mathbf{K}}(\mathbf{r})e^{i\mathbf{K}'\cdot\mathbf{r}}e^{-\mathbf{K}''\cdot\mathbf{r}} \\ &= \hat{\mathbf{E}}^{int}_{\mathbf{K}'}(\mathbf{r})e^{-\mathbf{K}''\cdot\mathbf{r}} \end{aligned} \tag{3.5}$$

where the mode function $\hat{\mathbf{E}}^{int}_{\mathbf{K}'}(\mathbf{r})$ is periodic. In the gap the fields $\hat{\mathbf{E}}^{int}_{\mathbf{K}'}(\mathbf{r})$ are interpolated between the allowed Bloch modes at the band edges. This model describes that at a depth $\mathbf{r}$ inside a finite photonic band gap crystal the vacuum modes that enter the crystal in a certain direction $\mathbf{K}$ are exponentially damped by a factor $e^{-\mathbf{K}''\cdot\mathbf{r}}$, where $\mathbf{K}''$ is the imaginary wave vector for propagation in the direction with unit vector $\mathbf{K}$ and is considered such that the waves decay inside the crystal.

The black dashed line in the Fig. 3.5 shows how we interpolate the field inside the band gap of a 1D photonic crystal. We know that the fields at the band edges are propagating. Here the absolute value of the field has the same period as the crystal. In the band gap we use a linear interpolation of the position of the field maximum as a function of z and therefore of ω to interpolate the periodic part of the mode function into the gap. The field amplitude is also linearly interpolated from its value at the lower edge to the upper edge. While a linear interpolation of the position is not an exact description of the behavior shown in Fig. 3.5, we have chosen it as it is a simple type of interpolation, and therefore a robust one. The calculated maximum error in the LDOS due to the linear interpolation is proportional to $1 - exp(-2zK'')$ in the starting unit cell. This comes from the maximum difference between the exact field and the field calculated using the model (see Fig. 3.5). For the structure considered in our calculation the maximum normalized error is 12%. In the n^{th} unit cell, however, this error is multiplied by $exp(-2nK''a)$ and therefore becomes smaller. Since the geometry of the considered infinite structure is nearly a quarter-wave stack [29], the band gap is the widest band gap for such a structure. Therefore the difference between the interpolated and the exact field behavior is in this case the largest; in any other structure the gap is narrower and hence the difference is smaller. Simultaneously, it is encouraging that the resulting maximum field amplitude matches well with the exact result. When in future more insight is obtained in the behavior of fields in a higher-dimensional band gap crystal, the interpolation can be improved. By this interpolation we have obtained the periodic part of the field at each frequency $\hat{\mathbf{E}}^{int}_{\mathbf{K}'}(\mathbf{r})$. To obtain the complete field $\mathbf{E}^{pbg}_{\mathbf{K}}(z)$ we then multiply the interpolated field $\hat{\mathbf{E}}^{int}_{\mathbf{K}'}(\mathbf{r})$ with the corresponding decaying factor $e^{-\mathbf{K}''z}$ at each frequency, where $\mathbf{K}''(\omega)$ is obtained from the band structure calculations (see Fig. 3.3).

The physical situation that we consider is shown in Fig. 3.1. A light source is embedded in a finite photonic crystal. Using our Ansatz that was introduced at

Eq. 3.5 and inserting it in Eq. 3.1 we obtain a general expression for the LDOS in a finite one-dimensional photonic band gap crystal:

$$N^{pbg}(\omega, z) = \frac{1}{(2\pi)} \frac{1}{m} \sum_{i=1}^{n} \sum_{j=1}^{m} F(\omega - \omega_{i,j}) \cdot |\hat{\mathbf{E}}_{K'}^{int}(z)|^2 exp(-2zK'') \tag{3.6}$$

where $F(\omega - \omega_{i,j})$ is the function that describes how the modes broaden in a finite photonic crystal.

In Eq. 3.6 we have distinguished the summation over real wave vectors $\mathbf{K}'$ from the damping by imaginary wave vectors $\mathbf{K}''$, and the factor 2 in the exponential originates from the mode functions squared in the LDOS. Thus at frequencies in the photonic band gap a light source at position z in a photonic band gap crystal experiences a continuum of vacuum fluctuations, all exponentially damped depending on their directions. The expression Eq. 3.6 leads to the correct limit of perfect inhibition ($N^{pbg} = 0$) for an infinitely large band gap crystal - consistent with Eq. 3.1 - since a light source is then infinitely far away ($| z | \longrightarrow \infty$) from the surface.

3.5 LDOS in the band gap of a finite 1D periodic structure

We note that in the case of a finite 1D periodic structure the dipole orientation $\mathbf{e}_d$ is in the same direction as $\hat{\mathbf{E}}_{n,\mathbf{K}'}$. Fig. 3.8 shows the calculated LDOS in the band gap using Eq. 3.6 for two different crystal sizes of $m = 10$ and $m = 20$ unit cells. It is apparent from the figure that the LDOS is non-zero in the band gap of both finite crystals. In contrast, in the band gap of an infinite structure, the LDOS is zero independent of frequency. Furthermore the LDOS becomes position dependent in the band gap of a finite crystal, again in contrast to the infinite crystal case where the LDOS does not depend on position in the band gap. Finally, the LDOS in the band gap strongly depends on crystal size, namely exponentially. This observation can not even be contrasted to an infinite crystal, since crystal extent is then irrelevant. It is seen that the LDOS is modulated in the unit cell due to interferences between the reflections from different layers in the crystal. This spatial dependence of the LDOS in the gap of a finite crystal is in stark contrast with the independence of position in an infinite crystal. In addition, the LDOS decays exponentially as a function of position into the crystal and has a minimum near the center of the structure. The exponential decay is faster at frequencies at the center of the band gap as the damping rate depends on the magnitude of the imaginary part of the wave vector $\mathbf{K}''$. Beside this fast decay at the center of the gap, the LDOS magnitude becomes also smaller since the amplitude of the Lorentzian modes gets smaller in the middle of the band gap.

Fig. 3.8 (a) and (b) allow us to compare the LDOS for two different crystal sizes. The LDOS in the central layer of the larger crystal with $m = 20$ layers is lower compared to the crystal with $m = 10$ layers. This illustrates that if we have a light source in the center of a large crystal, the spontaneous emission inhibition is higher due to a better shielding of vacuum fluctuations than in a small crystal.

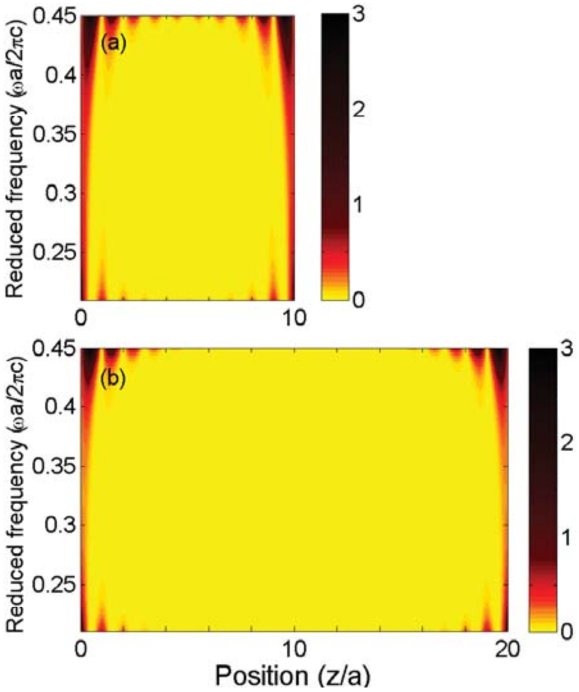

Figure 3.8: Local density of optical states (LDOS) in the frequency range of the band gap for (a) a finite crystal consisting of $m = 10$ periods and (b) a finite crystal consisting of $m = 20$ periods. In the band gap the envelope of the LDOS decays exponentially inside the structure with a minimum at the center of the structure. The attenuation of the LDOS is strongest at the center of the band gap because the imaginary part of the K'' vector is maximal. Moreover the summation over all $F(\omega - \omega_{i,j})$ is minimal at frequencies in the center of the band gap.

To verify our model for the LDOS in the band gap of a finite photonic band gap crystal, we compare the LDOS calculated using our model with the exact calculation of the LDOS in a finite 1D periodic structure. Fig. 3.7 shows both the exact LDOS calculations using transfer matrix method for a 1D, $m = 20$ periods structure and the LDOS calculated using our model for the same crystal at the same frequency. It is apparent in Fig. 3.7 that the result from the calculated LDOS using our Ansatz is in very good agreement with the exact LDOS. In both cases the LDOS shows the unit-cell modulations. The exponential decay in the LDOS at the same frequency is also the same and all curves are in good mutual agreement.

As a finite photonic crystal has an interface to the surrounding medium(see Fig. 3.2), there may exist surface modes at frequencies in the band gap [42]. These modes can play a role when one is investigating the LDOS on the surface of a photonic band gap crystal, for instance, when considering quantum emitters at the surface of a crystal. In our present study, we are investigating the LDOS as a function of depth in the bulk of a crystal where these modes are absent. Therefore we can safely neglect them in our study.

3.6 Conclusion

We have developed a new model to calculate the LDOS in the band gap of a finite photonic crystal. This model considers the broadening of the electromagnetic modes due to the finite size of the crystal. Our model also introduces an interpolation to calculate the electromagnetic field in the band gap using the band structure and the electromagnetic field at the band edge. A comparison with exact, analytical calculations for 1-dimensional periodic structures validates the model. From our results we have gained a better overview of the field behavior and especially the LDOS behavior in the band gap of a finite periodic structure. We find that inside the band gap of a finite structure the LDOS depends on frequency, position, and on crystal size, in contrast to an infinite structure where the LDOS is zero everywhere in the band gap independent of frequency and position.

Bibliography

[1] E. Yablonovitch, T. J. Gmitter, and K. M. Leung, *Photonic band stucture: the face-centered-cubic case employing nonspherical atoms*, Phys. Rev. Lett. **67**, 2295 (1991). — p.39.

[2] K. M. Ho, C. T. Chan, C. M. Soukoulis, R. Biswas, and M. Sigalas, *Photonic band gaps in three dimensions: new layer-by-layer periodic structures*, Solid State Commun. **89**, 413 (1994). — p.39.

[3] J. E. G. J. Wijnhoven and W. L. Vos, *Preparation of photonic crystals made of air spheres in titania*, Science **281**, 802 (1998). — p.39.

[4] Y. A. Vlasov, X.-Z. Bo, J. C. Sturm, and D. J. Norris, *On-chip natural assembly of silicon photonic bandgap crystals*, Nature **414**, 289 (2001). — p.39.

[5] A. Blanco *et al.*, *Large-scale synthesis of a silicon photonic crystal with a complete three-dimensional bandgap near 1.5 micrometres*, Nature **405**, 437 (2000). — p.39.

[6] S. Noda, K. Tomoda, N. Yamamoto, and A. Chutinan, *Full three-dimensional photonic bandgap crystals at near-infrared wavelengths*, Science **289**, 604 (2000). — p.39.

[7] J. Schilling, J. White, A. Scherer, G. Stupian, R. Hillebrand, and U. Gösele, *Three-dimensional macroporous silicon photonic crystal with large photonic band gap*, Applied Physics Letters **86**, 011101 (2005). — p.39.

[8] S. A. Rinne, F. García-Santamaría, and P. V. Braun, *Embedded cavities and waveguides in three-dimensional silicon photonic crystals*, Nature Photon. **2**, 52 (2007). — p.39.

[9] K. Aoki, D. Guimard, M. Nishioka, M. Nomura, S. Iwamoto, and Y. Arakawa, *Coupling of quantum-dot light emission with a three-dimensional photonic-crystal nanocavity*, Nature Photon. **2**, 688 (2008). — p.39.

[10] I. Staude, C. McGuinness, A. Frölich, R. Byer, E. Colby, and M. Wegener, *Waveguides in three-dimensional photonic bandgap materials for particle-accelerator on a chip architectures*, Opt. Expr. **20**, 5607 (2012). — p.39.

[11] J. M. van den Broek, L. A. Woldering, R. W. Tjerkstra, F. B. Segerink, I. D. Setija, and W. L. Vos, *Inverse-woodpile photonic band gap crystals with a cubic diamond-like structure made from single-crystalline silicon*, Adv. Funct. Mater. **22**, 25 (2012). — p.39.

[12] Z. Y. Li and Y. Xia, *Full vectorial model for quantum optics in three-dimensional photonic crystals*, Phys. Rev. A **63**, 043817 (2001). — p.39.

[13] K. Busch and S. John, *Photonic band gap formation in certain self-organizing systems*, Phys. Rev. E **58**, 3896 (1998). — p.39.

[14] M. D. Leistikow, A. P. Mosk, E. Yeganegi, S. R. Huisman, A. Lagendijk, and W. L. Vos, *Inhibited spontaneous emission of quantum dots observed in a 3D photonic band gap*, Phys. Rev. Lett. **107**, 1 (2011). — p.39.

[15] D. P. Fussell, R. C. McPhedran, and C. Martijn de Sterke, *Three-dimensional Greens tensor, local density of states, and spontaneous emission in finite two-dimensional photonic crystals composed of cylinders*, Phys. Rev. E **70**, 066608 (2004). — p.39.

[16] A. Moroz, *Minima and maxima of the local density of states for one-dimensional periodic systems*, Europhys. Lett. **46**, 419 (1999). — p.39.

[17] I. S. Nikolaev, W. L. Vos, and A. F. Koenderink, *Accurate calculation of the local density of optical states in inverse-opal photonic crystals*, J. Opt. Soc. Am. B **26**, 987 (2009). — p.39.

[18] J. M. Bendickson, J. P. Dowling, and M. Scalora, *Analytic expressions for the electromagnetic mode density in finite, one-dimensional, photonic band-gap structures*, Phys. Rev. E **53**, 4107 (1996). — p.39.

[19] A. A. Asatryan, K. Busch, R. C. McPhedran, L. C. Botten, C. Martijn de Sterke, and N. A. Nicorovici, *Two-dimensional Greens function and local density of states in photonic crystals consisting of a finite number of cylinders of infinite length*, Phys. Rev. E **63**, 046612 (2001). — p.39.

[20] M. Wubs and A. Lagendijk, *Local optical density of states in finite crystals of plane scatterers*, Phys. Rev. E **65**, 046612:1 (2002). — p.39.

[21] V. Prosentsov and A. Lagendijk, *The local density of states in finite size photonic structures, small particles approach*, Photonics and Nanostructures **5**, 189 (2007). — p.39.

[22] C. Hermann and O. Hess, *Modified spontaneous-emission rate in an inverted-opal structure with complete photonic bandgap*, J. Opt. Soc. Am. B **19**, 18 (2002). — p.39.

[23] R. Sprik, B. A. van Tiggelen, and A. Lagendijk, *Optical emission in periodic dielectrics*, Europhys. Lett. **35**, 265 (1996). — p.40.

[24] N. Vats, S. John, and K. Busch, *Theory of fluorescence in photonic crystals*, Phys. Rev. A **65**, 1 (2002). — p.40.

[25] W. L. Vos, A. F. Koenderink, and I. S. Nikolaev, *Orientation-dependent spontaneous emission rates of a two-level quantum emitter in any nanophotonic environment*, Phys. Rev. A **80**, 053802 (2009). — p.40.

[26] A. Yariv and P. Yeh, *Optical waves in crystal: Propagation and control of laser radiation* (John Wiley, New York, 1983). — p.42.

[27] V. Laude, Y. Achaoui, S. Benchabane, and A. Khelif, *Evanescent bloch waves and the complex band structure of phononic crystals*, Phys. Rev. B

80, 092301 (2009). — p.42.

[28] L. C. Botten, N. A. Nicorovici, R. C. McPhedran, C. M. d. Sterke, and A. A. Asatryan, *Photonic band structure calculations using scattering matrices*, Phys. Rev. E **64**, 046603 (2001). — p.42.

[29] J. D. Joannopoulos, S. G. Johnson, J. N. Winn, and R. D. Meade, *Photonic crystals - molding the flow of light, 2nd edition* (Princeton University Press, 2008). — p.42, 43, 49.

[30] P. St. J. Russell, T. A. Birks, and F. D. Lloyd-Lucas, in *Confined electrons and photons, edited by burstein, e. and weisbuch, c.*, edited by E. Burstein and C. Weisbuch (Springer US, 1995). — p.43.

[31] J. Als-Nielsen and D. McMorrow, *Elements of modern x-ray physics, second edition* (John Wiley, New York, 2011). — p.43.

[32] R. Newton, *Scattering theory of waves and particles* (Dover Publications, 1982). — p.46.

[33] J. Taylor, *Scattering theory: The quantum theory of nonrelativistic collisions* (Dover Publications, Incorporated, 2012). — p.46.

[34] S. Smolka, *Quantum correlations and light localization in disordered nanophotonic structures*, Ph.D. thesis, Technical University of Denmark (DTU), 2010. — p.47.

[35] H. Thyrrestrup, S. Smolka, L. Sapienza, and P. Lodahl, *Statistical theory of a quantum emitter strongly coupled to anderson-localized modes*, Phys. Rev. Lett. **108**, 113901 (2012). — p.47.

[36] L. Novotny and B. Hecht, *Principles of nano-optics* (Cambridge University Press. Cambridge, 2006). — p.48.

[37] E. S. C. Ching, P. T. Leung, A. Maassen van den Brink, W. M. Suen, S. S. Tong, and K. Young, *Quasinormal-mode expansion for waves in open systems*, Rev. Mod. Phys. **70**, 1545 (1998). — p.48.

[38] H. E. Türeci, A. D. Stone, and B. Collier, *Self-consistent multimode lasing theory for complex or random lasing media*, Phys. Rev. A **74**, 043822 (2006). — p.48.

[39] Y. Kopaev and W. Hanke, *Electronic phase transitions*, *Modern Problems in Condensed Matter Sciences* (Elsevier Science, 1992). — p.48.

[40] N. W. Ashcroft and N. D. Mermin, *Solid state physics* (Holt, Rinehart and Winston, New York, 1976). — p.48.

[41] In future, one might consider the Lorentzian width to depend on the dispersion relation. In the present work we already find a good agreement between our model and exact calculation of the LDOS, therefore we have not attempted to introduce dispersion in the width. — p.48.

[42] K. Ishizaki and S. Noda, *Manipulation of photons at the surface of three-dimensional photonic crystals*, Nature **460**, 367 (2009). — p.51.

CHAPTER 4

Finite size effects on a 3D photonic band gap; a cavity quantum electrodynamic approach

4.1 Introduction

Finite size effects are omnipresent in many different types of physical systems. A tangible example is the Ohm law $V = I.R$ for wires of different lengths. If we take a wire twice as long its resistance will double, since the resistance depends on the length L of the wire $R = R(L)$. Similarly many of the fascinating optical properties associated with nanophotonic systems such as a full 3D photonic band gap, weak and strong localization, and divergences in the densities of states are strongly depending on system size. Since finite-size effects are unavoidable in many different fields ranging from electronics and semiconductors to photonics and nano-structures, the understanding of these effects is crucial for the success of these fields, and will surely open up novel applications.

In quantum transport and in light transport the effect of finite sample size on transmission and on reflectivity has been extensively investigated experimentally and theoretically [1–5]. For a Bragg stack it is well-known that the percentage of reflected light in the stopgap depends on the number of layers in the stack. By increasing the number of layers a higher reflection is achieved.

Finite-size effects do not only modify the global properties of a system such as transmission and reflection, they also modify the local properties such as the local density of states (LDOS). In electronic systems, a well-known method to probe the LDOS is to employ a scanning tunneling microscope (STM) [6], see Fig. 4.1 (a). The working principle of the STM is based on the tunneling of the electron (or a hole) through a potential barrier between the STM tip and the sample surface. Due to the nature of an STM, however, such measurements are limited to spatial positions at the surface of a sample. With an STM, the LDOS is probed near the Fermi energy. By altering the voltage applied to the STM tip, it is possible to adjust the Fermi energy and hence probe the electronic LDOS at different energies [7]. At present, we are unaware of an experimental technique to study the electronic LDOS in bulk [*]. While there seems limited scope for theoretical interpretation of the LDOS in bulk, the electronic LDOS can be calculated from *ab-initio* theory such as tight-binding or plane-wave expansions.

In contrast in nanophotonics, it is possible to probe the LDOS in the bulk of a

---

[*] We thank dr. Geert Brocks for helpful discussions on this aspect.

crystal, as we will show in this chapter. We employ the feature that the photonic LDOS plays a central role in cavity quantum electrodynamics (QED) [8]. In the weak coupling approximation where Fermi's golden rule holds, the LDOS is proportional to the radiative emission rate that can be probed by time-resolved [9–13] or CW spontaneous emission [14, 15], see Fig. 4.1 (b). The LDOS does not only depend on frequency like the DOS, it also depends on position, and orientation of emitters' dipole moment with respect to the field. Here we are particularly interested in 3D photonic band gaps, in other words in the range of vanishing LDOS, where light is forbidden for all wave vectors and polarizations. The concept of a photonic band gap and its consequences for cavity QED were first introduced by Bykov in 1972 [16]. In 1987 it was brought to worldwide attention by the theoretical work of Yablonovich [17] and John [18]. Such band gaps are expected in 3D photonic crystals, *i.e.*, dielectric nanostructures with periodicities less than half the optical wavelength [19]. The present-day understanding of complex nanophotonic systems is heavily leaning on theories that describe infinite systems: $L \to \infty$. Well-known examples are random media and photonic crystals [20–24]. Therefore the predicted inhibition in the band gap only holds for infinite systems. In contrast, experiments are obviously performed on real devices with a finite extent. The question remains: Is a big photonic crystal the same as an infinite photonic crystal? After many efforts to fabricate 3D photonic band gap crystals the first experimental observation of inhibition in the band gap was performed by Leistikow *et al* in 2011 [11], showing a strong yet finite inhibition in a real photonic band gap crystal. Although there has been much study on photonic band gap crystals, to date there has not been any quantitative study on finite size effect in a real photonic band gap crystal. Moreover, to the best of our knowledge there is no theory for LDOS in a finite band gap crystal.

Our study here is the first ever systematic study of inhibition in a real photonic band gap crystal both experimentally and theoretically. We use the emission rate as a tool to investigate the finite size effect in photonic crystals. We map the quantum dots decay rate as a function of frequency through the photonic band gap. We observe up to 18-fold inhibition near the center of the band gap. Based on physical principles of the light propagation in a photonic crystal we develop a theory to interpret spontaneous emission rates measured on a finite photonic band gap crystal.

4.2 Experimental techniques

We have realized silicon inverse woodpile photonic band gap crystals by etching two sets of carefully aligned perpendicular pores using CMOS compatible methods. Fig. 4.2 (a) shows a micrograph of a typical 3D crystal [25]. The crystal has a diamond-like structure with an orthohombic lattice with parameters $a = 693$ nm and $c = 488$ nm ($a = \sqrt{2}c$). The 3D crystal extends over $L^3 = 12 \times 12 \times 12$ ac^2 which exceeds the Bragg attenuation length ℓ_{Bragg} in every direction [26]. As a result of multiple Bragg diffraction, frequency gaps form, known as stop gaps. If stop gaps in all directions overlap, a full 3D photonic band gap appears.

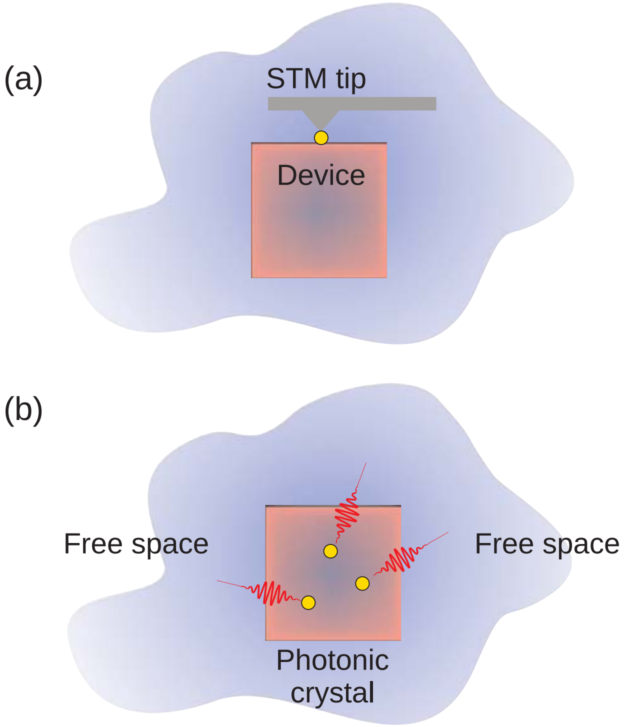

Figure 4.1: Schematic picture of a finite size system that has interaction with outside world and measuring LDOS for such systems. (a) An electronic device (pink gradient colored square). The gradient represents the gradual coupling to the environment. The only method to measure the LDOS in such a finite system is to use an STM. This only probes the LDOS on the surface. (b) Schematic representation of a finite photonic crystal in free space. Light sources (yellow dots) probe the LDOS deep inside the crystal.

Figure 4.2 (c) shows the band structure of an infinite inverse woodpile crystal made from silicon and infiltrated with toluene. The gray area shows the stop gap range of all crystal directions, which overlap in the range indicated with the yellow bar that is the full photonic band gap. The band gap range is in the near infrared and matches with the telecommunication range. The reflectivity spectra of 3D silicon inverse woodpile crystals reveal broad peaks with maximum reflectivity of 67% that are independent of the spatial position on the crystals. The spectrally overlapping reflectivity peaks for all directions and polarizations form the signature of a broad photonic band gap with a relative bandwidth up to 16% [26].

Here we measure decay rates of the PbS quantum dots in the band gap frequency range of an inverse woodpile photonic crystal. The PbS quantum dots have a wide emission spectrum ranging from 1300 to 1600 nm (see Ch. 2), overlapping with the band gap. PbS quantum dots are suspended in toluene. In order to infiltrate the quantum dots into the crystal we immerse the crystal in the quantum dots suspension. To measure the decay rate of quantum dots we have used the time-correlated single-photon counting method. The decay rate is

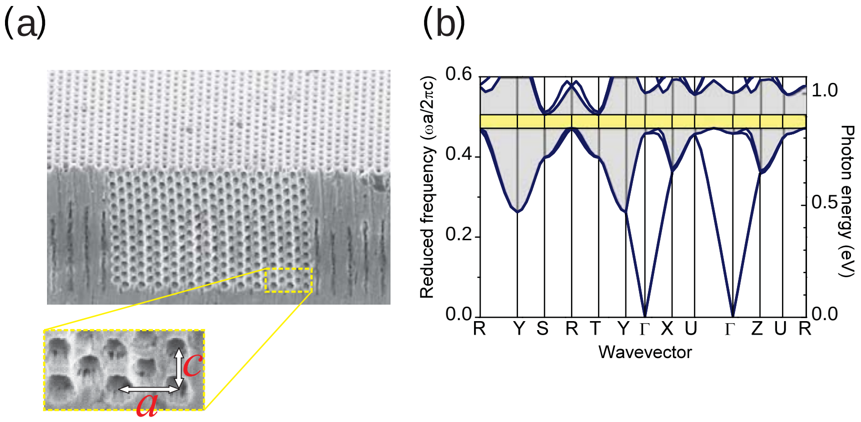

Figure 4.2: (a) Scanning electron micrograph of a 3D inverse woodpile silicon photonic crystal. The 3D crystal consists of two sets of perpendicularly etched pores, surrounded by a 2D crystal. (b) Band structure of an inverse-woodpile photonic crystal with pore radius 170 nm, $\varepsilon = 12.1$ for silicon and $\varepsilon = 2.25$ for toluene-filled pores. All stopgaps (shown with gray area) overlap, forming a full band gap indicated with the yellow bar

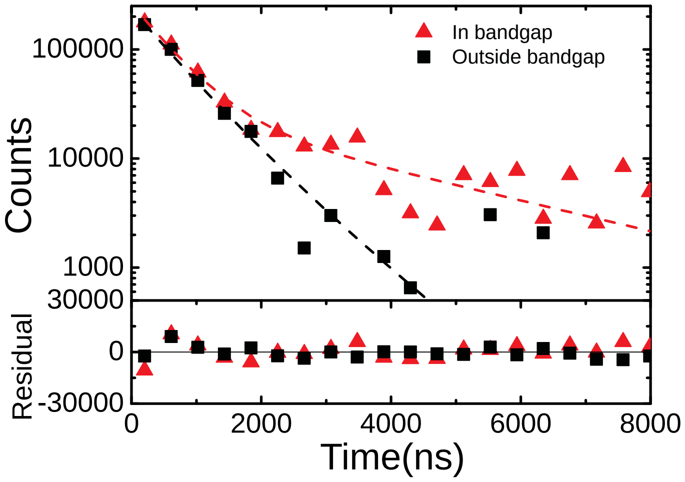

Figure 4.3: Time-resolved spontaneous emission measured on a PbS quantum dot suspension in a photonic crystal with the pore radius of 170 nm. The red triangles show the measured decay curve for the quantum dots at 0.853 eV in the band gap of the crystal. The black squares show the decay curve measured at 0.83 eV outside the band gap. Data is rebinned to 400 ns steps. Red and black dashed curves are bi-exponential fit to the data. Bottom panel: the residuals are random and symmetrically distributed around zero, indicating high quality fits.

obtained from the slope of the decay curve [27].

4.3 Experimental observations

Fig. 4.3 shows the time-resolved spontaneous emission of the quantum dots in the crystal at frequencies outside and inside the band gap. Outside the band gap quantum dots decay nearly exponentially, with a slope close to the one of the quantum dots in suspension. This is because outside the band gap the DOS of photonic crystal is similar to the DOS in free space and increases nearly quadratically with frequency, see Fig. 4.5. In the band gap we observe a non-single exponential decay for the quantum dots. As described in Ref. [11] the collected signal is a mixture of signal from the crystal and background signal from quantum dots outside the crystal. In the first 500 ns the decay rate is dominated by the fast decay rate of quantum dots in the suspension. It then deviates strikingly and shows a very slow decay rate, confirming suppression of spontaneous emission in the band gap. In our previous measurements [11] we have only measured up to 2000 ns time interval. Here by improving the signal-to-noise ratio of the setup we have been able to measure over a 4 times longer time extent, we could clearly observe a very slow decay as a result of inhibition in the band gap.

As we always collect a mixed signal from quantum dots outside the crystal and in the crystal, the decay curves always show one fast single exponential decay due to the suspension signal followed by a slow decay from quantum dots in the crystal. Therefore a bi-exponential model is a logical choice to model the time-resolved total count rate :

$$f(t) = I(S\ \gamma_0\ \ exp(-\gamma_0 t) + PC\ \gamma\ exp(-\gamma t)). \tag{4.1}$$

Here γ is the emission rate of quantum dots in the photonic crystal that we wish to obtain, and γ_0 is the rate of dots outside the crystal that is separately measured to be $\gamma_S = 1.7\ \mu s^{-1}$ (Fig. 2.3(b)). From the analysis done in Ch. 5 we find that this model is very robust. S and PC are relative factors for the signal from quantum dots in suspension or in the crystal and are fixed by scans of the detection focus, and only γ and I are adjusted [11]. In order to find S and PC, the detection objective is scanned once when it is positioned over the 3D crystal, and once when it is over the silicon wafer. By this method we find the amount of background light from other regions entering the detection objective.

Due to very low signal to noise ratio of the single photon detection in the near infrared, the data is collected for several hours for each decay curve which was feasible thanks to the great stability of our setup (Ch. 2). The background counts are substantial compared to the signal. Therefore we have performed a careful maximum likelihood analysis of the time-resolved data, see Ch. 5. The residuals from modeling the data are random and symmetric, centered around zero, indicating a good model to the data.

Thanks to the wide emission spectrum of the quantum dots we can measure the decay rate at several frequencies within the band gap range. In our experiment we measure the decay rate of quantum dots suspended in toluene γ_0 and also embedded in silicon inverse woodpile photonic crystals γ separately. In the band gap, we observed a strong inhibition of the total decay rate γ_0/γ of 18 times which is the largest ever inhibition observed in the band gap of a 3D photonic crystal. The 18 times inhibition is even an underestimate due to the fact that the simple bi-exponential model can not describe the slow decay component of the data. In time-resolved emission experiment we measure the total decay rate γ_{tot} which consists of both radiative γ_{rad} and non-radiative γ_{nrad} decay rate: $\gamma_{tot} = \gamma_{rad} + \gamma_{nrad}$. Interestingly, the maximum inhibition sets an upper bound to the non-radiative decay rate to be at most $\gamma_{nrad} \leq 0.05\gamma_0$. This non-radiative decay implies that the quantum dots have a quantum efficiency of at least 95%. In view of this very high room temperature efficiency we consider the upper bound to be the most reasonable estimate of γ_{rad}. The red data points in Fig 4.4 are the measured γ/γ_0 as a function of frequency throughout the band gap. The error bars indicate the credible interval of each data point stemming from the Bayesian statistical analysis on the data as discussed in Ch. 5. The credible interval is large at higher energies due to the small signal from the quantum dots. This is due to the fact that the emission spectrum of the quantum dots is not symmetric with respect to the band gap range and is very low at higher frequencies. At every frequency we have measured three times decay curves and extracted three γ/γ_0 which are in very close mutual agreement. This confirms the reproducibility of our measurements and stability of the setup in this challenging experiment.

By subtracting the upper bound γ_{nrad} from the total rate γ_{tot}, we arrive at the radiative rate γ_{rad} versus frequency that is shown in Fig. 4.4. At low frequency outside the band gap, the emission rate is slightly decreased, in agreement with infinite crystal theory. At the edge of the gap (0.845 eV) we observe a slightly enhanced emission rate. While this result has been reproduced several times, we have at this time no explanation for this result. At all frequencies in the 3D photonic band gap (0.845 to 0.905 eV), we observe a strong inhibition of the emission rate. The strongest inhibition seems to occurs at 0.867 eV, slightly off the center of the gap. Taking into consideration all measurements, the observed maximum inhibition appears to be about 50 to 100 times. These results are a stronger inhibition than the selected data from nano wire (Bleuse-PRL 2011 [13]) and for 2D photonic crystal slabs (Wang, Lodahl-PRL 2011 [28]), which for the first time ever confirms the old expectation on 3D band gaps (Yablonovitch 1987 [17], John 1987 [18]). Moreover, it is remarkable that the strong inhibition is observed for an ensemble of quantum emitters, with random dipole orientation [29], and not for a selected single emitter with optimized orientation or position. This result suggests that the ensemble contains emitters that experience both a weaker but also an even stronger inhibition than the average values quoted above.

4.4 Theory for 3D finite crystal

Photonic crystals redistribute the DOS both in frequency and space. The redistribution of the DOS in frequency is shown in Fig. 4.5, where the DOS is zero in the band gap and nearly quadratic with some peaks outside the band gap. The redistribution of the DOS in space is realized by the fact that inside a photonic band gap the DOS is zero while the total number of states is conserved so the DOS outside the gap has to increase in certain ranges. The spatial resolved or the

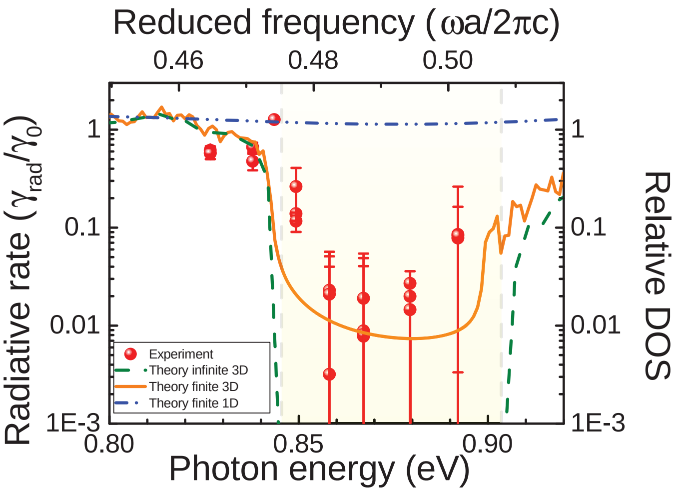

Figure 4.4: Comparing the data with the theory. The red circles are the measured γ/γ_0 of the quantum dots throughout the band gap. The bars are the credibility interval. The orange line is the calculated relative DOS. The calculation is for a 12 by 12 by 12 unit cells crystal (1728 k points in the Brillune zone) with pore radius $R = 170$ nm and $a = 693$ nm. The green dashed line is the relative DOS for an infinite crystal which goes to infinite in the band gap. The blue dot-dashed line is the calculated relative DOS following the 1D approach discussed in Sec. 4.4.

local density of states (LDOS) in the band gap of an infinite photonic crystal is zero as well as density of states (DOS). However, when the crystal becomes finite the concept of the DOS for an open finite photonic crystal is not very meaningful, since the volume of such a crystal is small compared to free space while we have to integrate over space to obtain the DOS. The DOS for a finite crystal is then the same as the DOS for free space. The LDOS, however, is defined for the crystal itself, since it is a function that depends on position anywhere either inside or outside the crystal. The LDOS is equal to the imaginary part of the Green function. Although there have been some efforts for calculating the LDOS in the band gap of 1D and 2D finite crystals [30–34], it becomes extremely challenging in 3D and to the best of our knowledge there is no analytic theory to calculate the LDOS for any class of crystal. For 3D light in a 3D inverse opal, Hermann and Hess have calculated the LDOS as a function of frequency, position, and for several position in the crystal by means of finite difference time domain (FDTD) simulations [35]. Kole has studied the LDOS by FDTD for finite opal crystals consisting of different number of spheres in clusters [36]. Unfortunately, however, these results can not be applied to other crystals, physical insights are not readily apparent, as is intrinsic to simulations. Finally such computer simulations require a lot of programming efforts and computational costs. Whittaker has calculated the transmission and the emission (but not LDOS) as a function of crystal thickness for a 3D photonic band gap crystal which is infinitely extended in two planar dimension, hence an infinite crystal volume [37]. Ishizaki *et al.* have simulated the emission rate that is proportional to the DOS in the middle layer of a finite 3D photonic band gap crystal. Therefore their calculations are

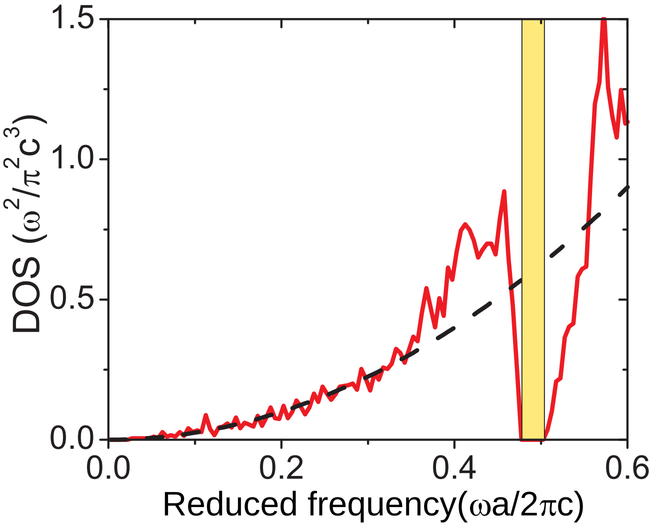

Figure 4.5: Density of states (DOS) per volume for the same crystal shown in Fig. 4.2 calculated with 10000 k points. The DOS vanishes in the band gap indicated with a yellow bar. Dashed curve: quadratic behavior in the low frequency limit.

limited to one particular position and do not describe the DOS over the whole volume supported by the crystal [38].

Here we introduce a new point of view on a finite 3D photonic band gap crystal. This original point of view enables us to develop a theory to calculate the finite support DOS in the band gap of a 3D finite photonic crystal. From the calculations performed in chapter 3 and published in Ref. [39] the LDOS depends on crystal size, frequency, and position in the crystal in the band gap of a finite crystal. The LDOS decreases exponentially in the band gap with position. In frequency domain the LDOS decreases from the band edge frequency toward the middle of the band gap. In addition to position and frequency the LDOS depends on the crystal size. The crystal size determines how much the modes in a crystal broaden and how many modes exist in a finite crystal. Due to the dependence of the LDOS on the crystal size, the LDOS is used to investigate the finite-size effects.

Since in our experiment the quantum dots are suspended in toluene they can move within the voids inside the crystal and diffuse everywhere. Since the diffusion time is in the order of micro second we assume that the density of particles is everywhere the same in the crystal. Therefore in our time resolved emission measurement we measure the LDOS averaged over all positions and dipole orientations in a unit cell. Our measurements are directly comparable with the finite support DOS that is a function of frequency and the crystal size and averaged over the emitters' position and orientation.

The physical situation in this case is the following: if we consider a light source deep inside a finite crystal, vacuum fluctuations can tunnel into the crystal and induce spontaneous emission. For the tunneling rate of vacuum fluctuation to inside or photons to outside we consider two different approaches as shown in

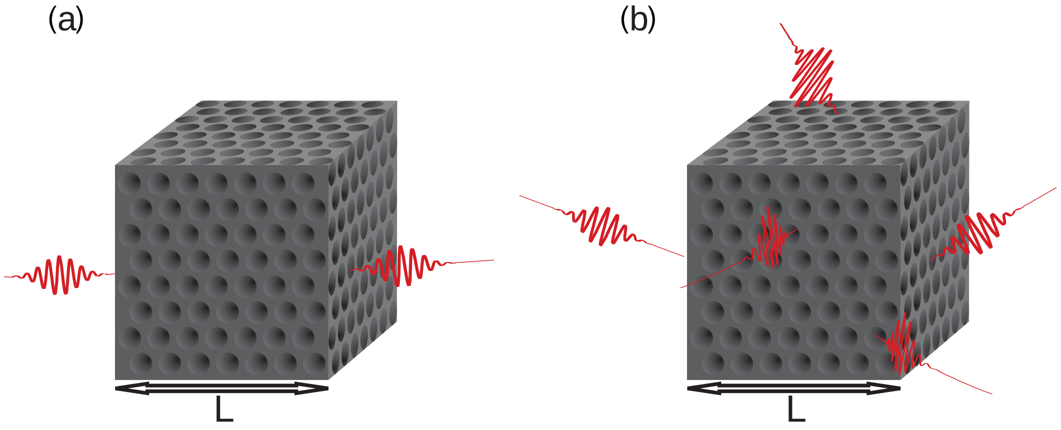

Figure 4.6: A schematic drawing of the physical situation of finite photonic crystals. (a) The first approach: a finite 3D photonic crystal with length L in every direction. The tunneling rate of vacuum fluctuation is set by the closest interface. (b) The second approach: the same crystal but the vacuum fluctuations (red wavelets) that are running around can tunnel into the band gap from all directions. The tunneling rate is set by the crystal volume.

Fig 4.6. In the first approach the rate depends on the closest vacuum-crystal interface to the emitter. This might seem logical since one possibly thinks that tunneling happens via the shortest distance to the emitter. This would mean that the LDOS length ℓ_{LDOS} [11] - the length in the crystal where the LDOS has decayed to the $1/e$ value of the LDOS outside the crystal - is the same as the Bragg length of the closest interface ℓ_{Bragg}. Therefore we only consider the number of unit cells in the direction of the nearest interface, which is equal to L/a with a the unit cell length and L the sample thickness. In this case light is considered to propagate only in one direction. Notice that the direction that has the shortest distance to the interface does not have necessarily the smallest Bragg length ℓ_{Bragg}.

In the second approach, light can propagate in all directions. Therefore the tunneling rate depends on the volume of the finite crystal or in other words on the total number of unit cells in the whole finite crystal volume. If we assume a cubic crystal with length L in each direction, the total number of allowed modes in a finite volume determines the volume per mode a^3/L^3 for such a 3D system. The volume per mode in the reciprocal lattice is inversely proportional to the real space volume of each unit cell in the crystal stemming from the $Born - von\ K\acute{a}rm\acute{a}n$ boundary condition in 3D [40].

Our starting point to calculate the finite support DOS is the definition of the

DOS for an infinite photonic crystal.

$$DOS(\omega) = \frac{1}{(2\pi)^3} \sum_n \int_{BZ} d\mathbf{K} \delta(\omega - \omega_{n,\mathbf{K}}), \tag{4.2}$$

where ω is the emission frequency. The integration over the real wave vector $\mathbf{K}$ is performed over the first Brillouin zone, and n is the band index. The modes in an infinite photonic crystal are delta functions at frequencies $\omega_{n,\mathbf{K}}$ that are the eigenvalues of the system. The eigen vectors in an infinite photonic crystal are Bloch modes that propagate throughout the whole crystal. These modes are absent in the band gap frequency range and therefore the DOS becomes zero in the band gap. If we extend the modes for infinite systems to represent finite-size effects then we have discrete number of modes that are broadened. The mode's shape becomes Lorentzian where linewidth depends on the crystal size. Here we assume that the crystal consists of m unit cells in every direction $L = m \cdot a$. These Lorentzian modes $F(\omega - \omega_{ij})$ have the following shape:

$$F(\omega - \omega_{ij}) = \frac{1}{(2\pi)} \left(\frac{\Delta_{ij}}{(\frac{\Delta_{ij}}{2})^2 + (\omega - \omega_{ij})^2} \right), \tag{4.3}$$

where Δ_{ij} is width of the Lorentzians and is taken to be the same for all the modes in a finite crystal. ω_{ij} is the central frequency of each mode and therefore the central frequency of each Lorentzian in a certain band (indicated by i) at a certain wave vector (indicated by j). The width Δ_{ij} and the number of the Lorentzian modes depends on whether we consider the 1D or 3D light propagation approach. If we consider the first one the number of Lorentzian modes is set by the crystal thickness and their width in the normalized unit is equal to:

$$\Delta_{\text{1D}} = \frac{a}{L}, \tag{4.4}$$

where L is the thickness, a is unit cell length, and therefore number of unit cells in one direction is $m_{\text{1D}} = L/a$.

If we consider the second approach (3D light propagation) then we should consider the total number of modes in the volume and their width in the normalized unit is:

$$\Delta_{\text{3D}} = \frac{a^3}{L^3}. \tag{4.5}$$

Following the same reasoning for 2D in-plane light propagation we have:

$$\Delta_{\text{2D}} = \frac{a^2}{L^2}. \tag{4.6}$$

Here the number of the unit cells in this finite volume determines the number of wave vectors in the Brillouin zone of such a finite crystal again following the *Born − von Kármán* boundary condition in solid state physics [40]. Since modes are now Lorentzian, for every wave vector we consider a Lorentzian mode and therefore we have m^3 Lorentzian modes for each band in a 3D light propagation, and m^2 and m for a 2D and a 1D propagation respectively.

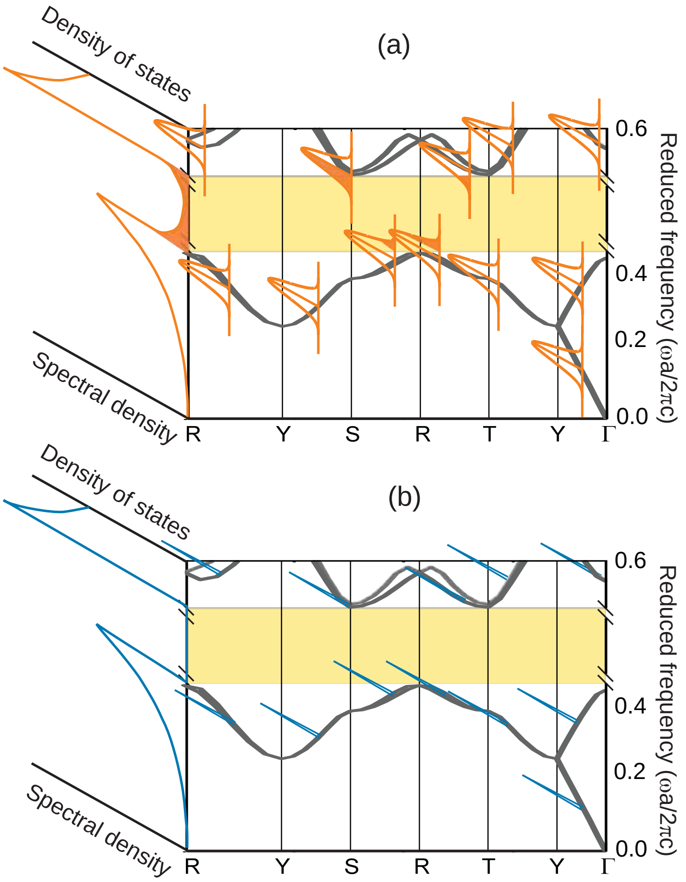

Figure 4.7: Schematic drawing of our theory for the density of states in a finite 3D crystal. We have used the band structure in Fig. 4.2. (a) In a finite crystal modes become Lorentzian functions (orange) that are broadened depending on the crystal size. The number of Lorentzian modes depends on the number of unit cells. Since modes are broadened they partially lie in the band gap range shown with the orange filled area. By adding all modes, we obtain a non-zero density of states in the band gap that gives rise to a finite inhibition as observed in our experiment. (b) In an infinite photonic crystal every individual mode is a delta function shown as blue spikes. Position and number of modes are chosen arbitrarily. Since there are no propagating modes in the band gap, no delta function extends into the photonic band gap. Hence the density of states, plotted in the third dimension at the left is zero in the band gap and only non zero outside the band gap. The spectral density elucidates the magnitude of each normalized mode.

The expression for the Lorentzian modes $F(\omega - \omega_{ij})$ tends to a Dirac delta function in the limit of an infinitely large crystal ($L \longrightarrow \infty$) in agreement with the theory of infinite photonic crystals [8, 22]. Due to the finite size of the crystal the modes become discrete. The averaged LDOS is thus the summation over all Lorentzian modes in the crystal volume normalized by the number of modes m^3

in the Brillouin zone:

$$N_{\text{finite}}^{\text{pbg}}(\omega - \omega_{ij}) = \frac{1}{m^3} \sum_{i=1}^{n} \sum_{j=1}^{m^3} F(\omega - \omega_{ij}) \tag{4.7}$$

Since the number of modes in a 3D crystal increases cubically with the number of unit cells in each direction, a cubic crystal of only $m = 12$ unit cells at every direction contains $m^3 = 1728$ modes. Therefore the volume per mode and thus the Lorentzians linewidth becomes cubically small.

Fig. 4.7 (a) illustrates our theory for a finite crystal where modes become Lorentzians. We use the calculated band structure in Fig. 4.2 (c) to illustrate the theory. The spectral density elucidates the magnitude of each mode, which is normalized. Here modes are shown with orange Lorentzians whose width is set by the crystal size. For simplification the number of modes is chosen arbitrarily. Since the modes are broad they partially extend into the band gap range which is indicated with the orange filled areas. By adding all the modes we end up with a non-zero density of states in the band gap. This non-zero density of states give rise to a finite inhibition in a finite photonic crystal as observed in our measurements. It is interesting to mention that Lorentzian linewidths are also considered for electrons [41]. In a crystal at finite temperature the electron scattering rate increases due to the electron-lattice interaction and electrons obtain Lorentzian spectral functions. The increased scattering rate can be also caused by lattice defects, impurity, doping, deformation of the structure, and structure rotation [3].

Fig. 4.7 (b) illustrates a similar scheme for the modes in an infinite photonic crystal, where every individual mode is a delta function shown as the blue spikes. Since there are no propagating modes in the band gap, there are no delta functions in the range of the photonic band gap. Since each mode function has zero width, no spectral density occurs in the band gap. The density of states is plotted on the third axis of the plot. As shown the density of states is zero in the band gap and non-zero outside the band gap.

4.5 Inhibition in the band gap

We have calculated the finite support DOS in the band gap of a finite photonic crystal. The DOS is a quantity that is proportional to the inhibition of the quantum dots in the band gap. If the DOS is below one then we expect that the quantum dots experience inhibition and if it is above one then they experience enhancement. Fig. 4.4 orange line shows the exact result of our Lorentzian theory. The finite support DOS is calculated for a finite silicon-toluene inverse woodpile photonic crystal consisting 12 unit cells in each direction, thus $12 \times 12 \times 12 = 1728$ k points in the Brillouin zone or 1728 modes. We have calculated the relative DOS in the band gap for the 1D and 3D approaches in comparison with the DOS calculated for a similar infinite structure. The range of the photonic band gap is indicated by the yellow bar.

The orange line in Fig. 4.4 shows the calculated inverse DOS when the width of each Lorentzian mode is proportional to the total number of modes following the 3D approach. The 3D theory is remarkably good in showing inhibition in the band gap range it also shows an excellent agreement with the measured data, validating the 3D theory. This is confirming that for a 3D crystal the *Born − von Kármán* boundary condition should be considered for all boundaries confining the crystal within its volume. Since inhibition is a unitless quantity that does not depend on the surrounding environment refractive index, we therefore calculate the finite support DOS also relative to the long wavelength range DOS of the crystal. The blue dot-dashed line in Fig. 4.4 shows the calculated DOS for the 1D approach when tunneling happens only in one direction. The calculation following the 1D approach not only gives rise to a DOS above one in the band gap(enhancement) that is non-physical, it is also far from the experimental data. We conclude that in a 3D finite crystal it is not only the closest interface that leads to tunneling of the vacuum fluctuations, but it is every direction in the crystal volume that determines the volume per mode and that determines the tunneling strength. For comparison the DOS calculated for the infinite crystal (green dashed line) is also shown in in Fig. 4.4. The infinite DOS tends to zero in -as expected- strong disagreement with our measurements on a real finite size band gap crystal.

It is remarkable that the density of states (DOS), which is strictly zero in the band gap of an infinite crystal irrespective of frequency (within the gap of course) and position, becomes strongly dispersive in a finite crystal. We expect that our theory is applicable to a wide range of complex nanophotonic metamaterials, and condensed matter that have a band gap for many different classes of waves.

4.6 How big should a photonic band gap crystal be?

In this section we investigate how the maximum inhibition in the band gap depends on the crystal size. Figure 4.8 shows the maximum inhibition in the band gap calculated for crystals with different volume. We considered crystals made of 7 layers (343 unit cells), 10 layers (1000 unit cells), 11 layers (1331 unit cells), and 12 unit cells (1728 unit cells). The DOS decreases linearly with the number of unit cells. Remarkable that a (photonic) crystal property depends algebraically on size and not exponentially. It is reminiscent of Ohm's law where conductance also depends linearly on size as mentioned in the introduction.

The linear behavior of the the DOS versus crystal size is supported by the following: Let's consider the Lorentzian mode function $F(\omega - \omega_{ij})$:

$$F(\omega - \omega_{ij}) = \frac{1}{(2\pi)}\left(\frac{\Delta_{ij}}{(\frac{\Delta_{ij}}{2})^2 + (\omega - \omega_{ij})^2}\right), \tag{4.8}$$

with ω_{ij} the central frequency of the Lorentzian, and Δ_{ij} the bandwidth that we chose to be inversely proportional to volume: $\Delta_{ij} = a^3/L^3 = 1/m^3$ with a the lattice parameter. Let's consider that we are in the bandgap at a constant

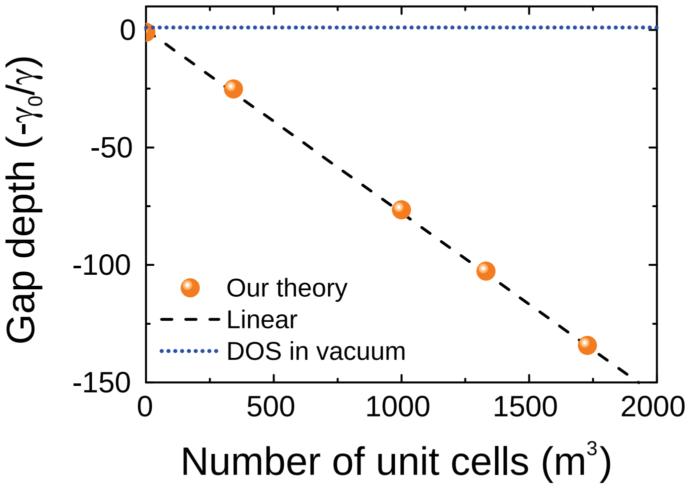

Figure 4.8: The gap depth or the minimum relative DOS in the band gap as a function of crystal size is shown in comparison with DOS in vacuum. The DOS in the photonic band gap crystal decreases only weakly with crystal size (proportional to the total number of unit cells).

detuning $(\omega - \omega_{ij}) \equiv c$. Now we can rewrite our Lorentzian as

$$F(\omega - \omega_{ij}) \propto \frac{(1/m)^3}{((1/m)^3)^2 + c^2} = \frac{(1/m)^3}{(c^2 + (1/m)^6)} \tag{4.9}$$

This result shows that the Lorentzian mode function goes with m^3, and this is exactly what we see in Fig. 4.8.

Our observation does not agree with the expected exponential decrease of the DOS with crystal size as shown by Ishizaki *et al* [38], or Kole [36]. This difference is understandable, since in their calculation they consider the position dependency in the crystal, while our calculation is averaged over position and is based on number of modes in crystal volume. Since there is no position dependency in the DOS, there is absolutely no reason for exponential positions dependence. The DOS is only determined by the Lorentzians, that decreases as $1/m^3$ inside the band gap. The finite support DOS decreases only weakly with crystal size (proportional to the total number of unit cells), we therefore conclude that in practice there is no finite crystal that effectively behaves as an infinite crystal. We believe that our quantitative understanding can be used not only for the photonic systems also in any condensed-matter system where the transport mean free path is longer than system size such as electrons in (semi)conductors, or Cooper pairs in superconductors or phonons and magnons in crystals. If the mean free path is shorter than the system size the propagator such as photon or electron does not see the effect of the interface since it loses its memory of one interface before it reaches the other interfaces.

4.7 Conclusion and discussion

We have studied the finite size effect on the density of states in photonic crystals both experimentally and theoretically. We have measured time-resolved emission of semiconductor quantum dots that emit in the telecom range within the band gap of silicon 3D photonic crystals. Finally, the long-searched inhibition in the photonic band gap crystal is observed. The inhibition is strong, yet finite, suggesting a finite-size effect on the inhibition. To interpret our experimental observation we have devised an original theory that allows the models for infinite systems to be extended to represent finite-size effects, without actually reducing the size of the infinite system. The method is based on an extension of the wave-vector space of the eigenmodes into the complex plane. A remarkable result is that the density of states (DOS), which is strictly zero in the band gap of an infinite crystal irrespective of frequency becomes strongly dispersive in a finite crystal. Interestingly, the DOS decreases linearly with the crystal volume. This weak dependency of the DOS to the crystal size suggests that no finite crystal behaves as an infinite crystal. Our theory for finite size 3D photonic band gap crystal shows that we are in the position to explain our experimental observations on the nonzero and frequency-dependent LDOS inside the 3D photonic band gap. We expect that our theory is applicable to a wide range of complex nanophotonic metamaterials such as in lasers, fibers, and sensors. We believe that our quantitative understanding can be used not only for the photonic systems also in any condensed-matter system where the transport mean free path is long such as electrons in (semi)conductors at low temperature, or Cooper pairs in superconductors, or phonons, and magnons in crystals. If the mean free path is shorter than the system size the propagator such as photon or electron does not see the effect of the interface since it loses its memory of one interface before reaches the other interfaces.

Bibliography

[1] F. J. Pinski, P. B. Allen, and W. H. Butler, *Calculated electrical and thermal resistivities of Nb and Pd*, Phys. Rev. B **23**, 5080 (1981). — p.55.

[2] S. Y. Savrasov and D. Y. Savrasov, *Electron-phonon interactions and related physical properties of metals from linear-response theory*, Phys. Rev. B **54**, 16487 (1996). — p.55.

[3] S. Datta, *Quantum transport: Atom to transistor* (Cambridge University Press, 2013). — p.55, 66.

[4] J. F. Bertone, P. Jiang, K. S. Hwang, D. M. Mittleman, and V. L. Colvin, *Thickness dependence of the optical properties of ordered silica-air and air-polymer photonic crystals*, Phys. Rev. Lett. **83**, 300 (1999). — p.55.

[5] B. Harbecke, *Coherent and incoherent reflection and transmission of multilayer structures*, Appl. Phys. B **39**, 165 (1986). — p.55.

[6] G. Binnig and H. Rohrer, *Scanning tunneling microscopy from birth to adolescence*, Rev. Mod. Phys. **59**, 615 (1987). — p.55.

[7] J. Li, W.-D. Schneider, R. Berndt, and B. Delley, *Kondo scattering observed at a single magnetic impurity*, Phys. Rev. Lett. **80**, 2893 (1998). — p.55.

[8] R. Sprik, B. A. van Tiggelen, and A. Lagendijk, *Optical emission in periodic dielectrics*, Europhys. Lett. **35**, 265 (1996). — p.56, 65.

[9] D. Englund, D. Fattal, E. Waks, G. Solomon, B. Zhang, T. Nakaoka, Y. Arakawa, Y. Yamamoto, and J. Vučković, *Controlling the spontaneous emission rate of single quantum dots in a two-dimensional photonic crystal*, Physical review letters **95**, 013904 (2005). — p.56.

[10] P. Anger, P. Bharadwaj, and L. Novotny, *Enhancement and quenching of single-molecule fluorescence*, Phys. Rev. Lett. **96**, 113002 (2006). — p.56.

[11] M. D. Leistikow, A. P. Mosk, E. Yeganegi, S. R. Huisman, A. Lagendijk, and W. L. Vos, *Inhibited spontaneous emission of quantum dots observed in a 3D photonic band gap*, Phys. Rev. Lett. **107**, 193903 (2011). — p.56, 59, 63.

[12] M. R. Jorgensen, J. W. Galusha, and M. H. Bartl, *Strongly modified spontaneous emission rates in diamond-structured photonic crystals*, Phys. Rev. Lett. **107**, 143902 (2011). — p.56.

[13] J. Bleuse, J. Claudon, M. Creasey, N. S. Malik, J.-M. Gérard, I. Maksymov, J.-P. Hugonin, and P. Lalanne, *Inhibition, enhancement, and control of spontaneous emission in photonic nanowires*, Phys. Rev. Lett. **106**, 103601 (2011). — p.56, 60.

[14] A. F. Koenderink, L. Bechger, H. Schriemer, A. Lagendijk, and W. L. Vos, *Broadband fivefold reduction of vacuum fluctuations probed by dyes in photonic crystals*, Phys. Rev. Lett. **88**, 143903 (2002). — p.56.

[15] S. Ogawa, M. Imada, S. Yoshimoto, M. Okano, and S. Noda, *Control of light emission by 3d photonic crystals*, Science **305**, 227 (2004). — p.56.

[16] V. Bykov, *Spontaneous emission in a periodic structure*, Sov. Phys. JETP **35**, 269 (1972). — p.56.

[17] E. Yablonovitch, *Inhibited spontaneous emission in solid-state physics and electronics*, Phys. Rev. Lett. **58**, 2059 (1987). — p.56, 60.

[18] S. John, *Strong localization of photons in certain disordered dielectric superlattices*, Phys. Rev. Lett. **58**, 2486 (1987). — p.56, 60.

[19] J. D. Joannopoulos, S. G. Johnson, J. N. Winn, and R. D. Meade, *Photonic crystals - molding the flow of light, 2nd edition* (Princeton University Press, 2008). — p.56.

[20] S. John and J. Wang, *Quantum electrodynamics near a photonic band gap: Photon bound states and dressed atoms*, Phys. Rev. Lett. **64**, 2418 (1990). — p.56.

[21] Z. Y. Li and Y. Xia, *Full vectorial model for quantum optics in three-dimensional photonic crystals*, Phys. Rev. A **63**, 043817 (2001). — p.56.

[22] N. Vats, S. John, and K. Busch, *Theory of fluorescence in photonic crystals*, Phys. Rev. A **65**, 1 (2002). — p.56, 65.

[23] X. H. Wang, B. Y. Gu, R. Z. Wang, and H. Q. Xu, *Decay kinetic properties of atoms in photonic crystals with absolute gaps*, Phys. Rev. Lett. **91**, 113904 (2003). — p.56.

[24] P. T. Kristensen, A. F. Koenderink, P. Lodahl, B. Tromborg, and J. Mork,

Fractional decay of quantum dots in real photonic crystals, Opt. Lett. **33**, 1557 (2008). — p.56.

[25] J. M. van den Broek, L. A. Woldering, R. W. Tjerkstra, F. B. Segerink, I. D. Setija, and W. L. Vos, *Inverse-woodpile photonic band gap crystals with a cubic diamond-like structure made from single-crystalline silicon*, Adv. Func. Mater. **22**, 25 (2012). — p.56.

[26] S. R. Huisman, R. Nair, L. A. Woldering, M. D. Leistikow, A. P. Mosk, and W. L. Vos, *Signature of a three-dimensional photonic band gap observed on silicon inverse woodpile photonic crystals*, Phys. Rev. B **83**, 205313 (2011). — p.56, 57.

[27] D. V. O'Connor and D. Philips, *Time correlated single photon counting* (Academic Press, 1984). — p.58.

[28] Q. Wang, S. Stobbe, and P. Lodahl, *Mapping the local density of optical states of a photonic crystal with single quantum dots*, Phys. Rev. Lett. **107**, 167404 (2011). — p.60.

[29] W. L. Vos, A. F. Koenderink, and I. S. Nikolaev, *Orientation-dependent spontaneous emission rates of a two-level quantum emitter in any nanophotonic environment*, Phys. Rev. A **80**, 053802 (2009). — p.60.

[30] J. M. Bendickson, J. P. Dowling, and M. Scalora, *Analytic expressions for the electromagnetic mode density in finite, one-dimensional, photonic band-gap structures*, Phys. Rev. E **53**, 4107 (1996). — p.61.

[31] A. A. Asatryan, K. Busch, R. C. McPhedran, L. C. Botten, C. Martijn de Sterke, and N. A. Nicorovici, *Two-dimensional Greens function and local density of states in photonic crystals consisting of a finite number of cylinders of infinite length*, Phys. Rev. E **63**, 046612 (2001). — p.61.

[32] M. Wubs and A. Lagendijk, *Local optical density of states in finite crystals of plane scatterers*, Phys. Rev. E **65**, 046612:1 (2002). — p.61.

[33] D. P. Fussell, R. C. McPhedran, and C. Martijn de Sterke, *Three-dimensional Greens tensor, local density of states, and spontaneous emission in finite two-dimensional photonic crystals composed of cylinders*, Phys. Rev. E **70**, 066608 (2004). — p.61.

[34] V. Prosentsov and A. Lagendijk, *The local density of states in finite size photonic structures, small particles approach*, Photonics and Nanostructures **5**, 189 (2007). — p.61.

[35] C. Hermann and O. Hess, *Modified spontaneous-emission rate in an inverted-opal structure with complete photonic bandgap*, J. Opt. Soc. Am. B **19**, 18 (2002). — p.61.

[36] S. Kole, *New methods for the numerical solution of maxwell's equations*, PhD Thesis, Rijksuniversiteit Groningen, 2003. — p.61, 68.

[37] D. M. Whittaker, *Inhibited emission in photonic woodpile lattices*, Opt. Lett. **25**, 779 (2000). — p.61.

[38] K. Ishizaki, M. Okano, and S. Noda, *Numerical investigation of emission in finite-sized, three-dimensional photonic crystals with structural fluctuations*, J. Opt. Soc. Am. B **26**, 1157 (2009). — p.62, 68.

[39] E. Yeganegi, A. Lagendijk, A. P. Mosk, and W. L. Vos, *Local density of optical states in the band gap of a finite one-dimensional photonic crystal*,

Phys. Rev. B **89**, 045123 (2014). — p.62.

[40] N. W. Ashcroft and N. D. Mermin, *Solid state physics* (Holt, Rinehart and Winston, New York, 1976). — p.63, 64.

[41] K. Gilmore, *Precession damping in itinerant ferromagnets*, PhD Thesis, Montana State University, 2007. — p.66.

CHAPTER 5

Statistical analysis of time-resolved emission in the near infrared

5.1 Introduction

Spontaneous emission of light is a fundamental process that plays an essential role in many phenomena in nature and forms the basis of many applications. As is described by Fermi's "golden rule" [1], spontaneous emission of light is not only a property of the emitter itself but also depends on the environment [2]. To study the light-matter interactions in time, it is essential to study the decay dynamics of sources. This is obtained from time-resolved emission experiments. A time-resolved emission experiment consists of a histogram of photon arrival times over multiple cycles of laser excitation and photon detection. In order to obtain not only the fluorescence decay time but also the decay curve shape with sufficient statistics, one needs sufficient dynamic range, corresponding to several decay times in the time domain.

The use of near infrared spontaneous emission is receiving growing attention in many fields [3, 4] such as silicon technology [5], in photonic band gap crystals [6, 7], solar energy harvesting [8], lasing [9–11], light emitting diodes [12], telecommunication [13], opto-electronic devices [14], and has attracted a lot of interest in biomedical imaging in living tissue [15–17]. There is a growing interest to improve quantum efficiency and tune luminescence toward the infrared range by changing size and material composition of quantum dots [18, 19] or to modify and control the near-infrared emission by placing emitters in cavities and photonic crystals [20].

Unfortunately, however, photon detection in the near infrared is much more difficult than in the ubiquitous visible range due to the following reasons. Firstly, from Fermi's "golden rule" the decay rate of emitters is proportional to the frequency cubed, ω^3. Decay rates of emitters in the near infrared range are therefore much lower than in the visible range [1]. If we consider typical near-infrared emitters that emit at a wavelength around 1500 nm, the decay rate is about 27 times lower than for typical visible emitters at 500 nm. As a consequence the number of collected photons per time unit is much lower in the infrared as compared to the visible range. Figure 5.1 shows typical time-resolved emission data in the near infrared and in the visible spectral range. Figure 5.1(a) shows a decay curve measured for PbS quantum dots inside a 3D photonic band gap in the near infrared spectral region. It is clear from the figure that the signal level is very small compare to the background. Figure 5.1(b) shows the decay curve for R6G dye molecules in the visible spectral region. The signal is typically 3 orders of magnitude greater than the background.

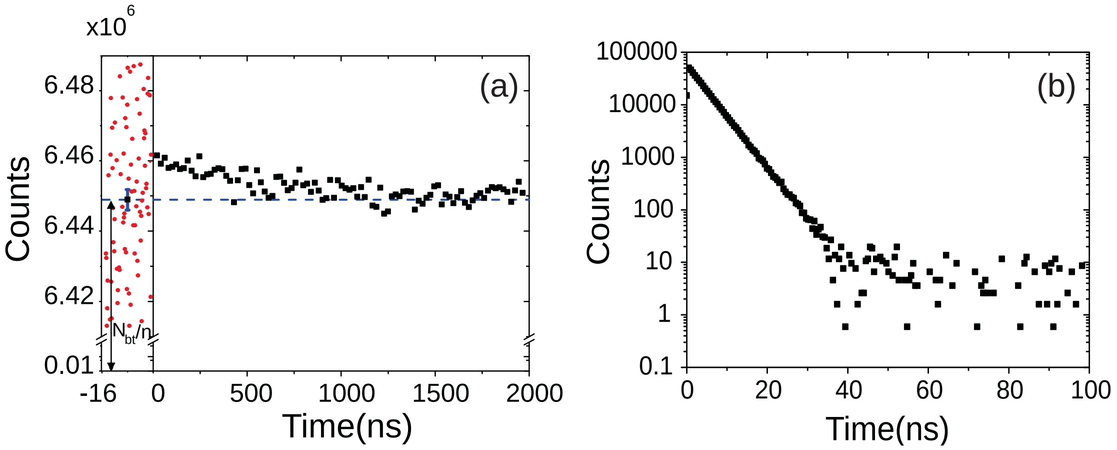

Figure 5.1: Comparison of time-resolved emission experiments in different spectral ranges. (a) Time-resolved emission measurement of PbS quantum dots in a 3D photonic band gap crystal in the near infrared range at 0.9 eV. In addition to a high background level due to detector dark count the signal is very low due to the 3D bandgap. The red dots at negative times show the counts used to calculate the background. The background counts are multiplied by the bin-reduction factor used for signal bin-reduction. The single black square at negative time and the blue dash-line show the average background value and the error bar shows one standard deviation (σ) of the background. (b) Time-resolved emission of R6G dye in water in the visible range at $\lambda = 563nm$. The signal level is about 3 orders of magnitude higher than the background level.

Secondly, to obtain a statistically reliable histogram of photon arrival times the repetition rate of the excitation laser must be at least 5 times lower than the decay rate under study [21]. The low decay rates in the near infrared limit the maximum laser repetition rate and thereby further reduce the signal rate.

Thirdly, another difficulty in the near infrared range originates from high background level due to the high dark count rates of near infrared photon-detectors. Photo-multiplier tubes typically display 2000 times more dark counts and a 20 times lower quantum efficiency in the near infrared as compared to silicon detectors for the visible * [22]. The background detector counts are subject to Poissonian statistics leading to inevitable fluctuations in signal counts. The standard deviation of Poissonian noise is equal to the square root of the average number of events and therefore by increasing the background level the noise level in the signal also increases.

Therefore due to the above mentioned reasons, in the near infrared spectral range the photon arrival time histograms are measured with a very low signal to noise ratio. After measuring the histogram one is interested in obtaining the

---

* Superconducting single photon detectors SSPDs are sensitive to single photons. These detectors show a low dark count rate in the infrared range yet they are highly specialized since they require cryogenic temperature [23]

decay rate, but the huge background level makes this extraction difficult. Since subtracting a wrong background will lead to a wrong decay rate, estimation of the correct background level in the near infrared time-resolved experiments is of key importance. Therefore looking at statistics and including prior information about background for data analysis becomes significant.

In this chapter we discuss a statistical analysis of photoluminescence measurements done by time-correlated single-photon counting method. We propose to estimate the background value by using a maximum *a posteriori* estimation (MAP) method [24–27]. This powerful method allows us to refine the decay rate using *a priori* knowledge about the background. Data are accepted (or discarded) if the decay curves are modeled assuming a dark rate that lies inside (or outside) the credibility interval imposed by purely statistical arguments. We illustrate our method by applying it to the decay dynamics of PbS quantum dots in suspension and to PbS quantum dots inside 3D photonic band gap crystals, see Fig. 5.1(a).

5.2 Bayesian analysis of time-resolved emission measurement

5.2.1 Bayesian method

A decay curve $\mathcal{F}(t;\{p_i\},B)$ is a histogram of the photon arrival times t after many excitation-detection cycles [21, 28, 29]. After measurement, the histogram is modeled with a decay function $f(t;\{p_i\})$ from which the parameters ($\{p_i\}$) such as decay rate of the emission is deduced, plus a true background value B:

$$\mathcal{F}(t;\{p_i\},B) = f(t;\{p_i\}) + B. \tag{5.1}$$

In principle B is also a parameter, but since it is a property of the optical setup we treat it separately. In the simplest case when the system is characterized by a single decay rate, the decay function is described by a single exponential:

$$f(t;\{\gamma_s, I\}) = Iexp(-\gamma_S t), \tag{5.2}$$

where I and γ_S are the model parameters $\{p_i\}$. Here γ_S is the emitters decay rate that we wish to obtain. Figure 5.1 (b) shows an example of such single exponential decay. A normal fitting routine such as least square can be used to extract model parameters. If the background level is relatively low compared to the signal level then background can be one of the model parameters, or the average value of the background can be subtracted from the data before the analysis. Figure 5.1(b) is an example of time-resolved emission data with high signal to noise ratio. In this case the average value of the background is subtracted and the decay curve is modeled using Eq. (5.2) resulting in $I = 50000$ and $\gamma_S = 0.23\ ns^{-1}$. However, in the case which the signal level is very low compared to the huge background as is shown in figure 5.1(a), the conventional background subtraction may lead to a wrong parameter determination. It is therefore important to have a background measurement independent of the model. If the background measurement itself has a significant statistical uncertainty, however, we must proceed carefully. In this case *a priori* information of the background can be used to refine the best estimate for the decay rate. To include *a priori* information we use Bayesian analysis that is one of the fundamental approaches to statistical analysis.

Bayesian analysis is based on Bayes' theorem [25]. The usual form of Bayes' theorem is

$$P(A|B) = \frac{P(A|B)P(A)}{P(B)} \tag{5.3}$$

where $P(A|B)$ is the *a posteriori* probability which is the probability for A after taking into account B, $P(B|A)$ is probability of finding A under the condition of B and known as likelihood, $P(A)$ is prior probability of A, $P(B)$ is probability of a given evidence which is fixed.

For the example of the decay curve Bayes' theorem can be written as

$$P(B, \{p_i\}|\{y_i\}, N_{bt}) = \frac{P(\{p_i\})P(B|N_{bt})}{P(\{y_i\})} P(\{y_i\}|\{p_i\}, B), \tag{5.4}$$

where $\{y_i\}$ are the measured data, and N_{bt} is the measured background. $P(\{p_i\})$ is the prior distribution of model parameters, and $P(B|N_{bt})$ is the prior distribution of the background under condition of the measured background which are both known. $P(\{y_i\})$ is a normalization constant, $P(\{y_i\}|\{p_i\}, B)$ is the probability of data given the parameters, which is also known as likelihood of the parameters, and $P(B, \{p_i\}|\{y_i\}, N_{bt})$ is the *a posteriori* probability distribution that we wish to obtain.

In conventional fitting routines, such as least square minimization that is widely used to model the decay dynamics, the likelihood is maximized and no prior information is included. Bayesians statistics, however, is concerned with generating the posterior distribution of unknown parameters, given both the data and prior information for these parameters. The main equation of Bayesians statistics known as Bayes' theorem, combines prior information and the likelihood of the parameters to reach the posterior distribution for the model parameters, where this posterior distribution is maximized to extract the parameters of interest. For data with a low signal-to-noise ratio, a Bayesians analysis can strongly improve the analysis by including any prior probability distribution of parameters that are available before the data analysis [26]. In contrast, conventional fitting procedures only give a most likely parameter estimate and often make the implicit assumption that the data are normal distributed. Here we present a proper analysis of time-resolved emission measurement of data with low signal to noise ratio based on a Bayesian method.

5.2.2 A priori estimation of the background

To use Bayes' theorem Eq. (5.4), first we need to find *a priori* information of the background $P(B|N_{bt})$ given a measured background. We can obtain the prior information for B from the measured decay curve at $t < 0$ before the excitation laser pulse arrives, where we have only background counts. Let us assume that the true ensemble average dark level (in counts per time bin) is B. If we average a number n of background bins, the expected total number of dark counts is $< N_{bt} >= Bn$, which is Poisson distributed. Since the number of counts is large we may approximate the Poisson distribution with a Gaussian distribution:

$$P(B|N_{bt}) = \frac{1}{\sqrt{2\pi}} \frac{n}{\sqrt{N_{bt}}} e^{-(N_{bt}-Bn)^2/2N_{bt}}. \tag{5.5}$$

In other words, the measurement of N_{bt} causes the probability distribution of B to become a Gaussian with center N_{bt}/n and the standard deviation $\sigma = \sqrt{N_{bt}}/n$. The true value of the dark count rate B is expected to lie with 70% probability in the so-called credibility interval equal to [27]:

$$\frac{N_{bt} - \sqrt{N_{bt}}}{n} < B < \frac{N_{bt} + \sqrt{N_{bt}}}{n}. \tag{5.6}$$

5.2.3 A posteriori estimation for model parameter, and goodness-of-fit

To interpret the time-resolved emission measurements the next step is to find a good model which explains data. The model validation is one of the most important steps in the model building sequence. Here we assume for simplicity that the model is known, namely single exponential decay for a suspension of light sources, or for light sources embedded in a photonic bandgap crystal.

Assuming Gaussian noise with known standard deviation σ for the measured data y_i, we define the goodness of fit χ^2 as

$$\chi^2 \equiv \sum \frac{(\{y_i\} - \{f(t_i; \{p_i\}, B))^2}{\sigma_i^2}, \tag{5.7}$$

where y_i^{th} are the corresponding model points. A direct probability interpretation is possible [30]: If we suppose the model parameters $\{p_i\}$ are known exactly, then the probability density of measuring the dataset $\{y_i\}$ is equal to

$$P(\{y_i\}|\{p_i\}, B) = \frac{1}{\prod_i^N \sigma_i \sqrt{2\pi}} e^{-\chi^2/2}. \tag{5.8}$$

considering that data points are independent. By inserting Eq. (5.8) and Eq. (5.5) in Eq. (5.4) and considering $P(\{p_i\})$ and $P(\{y_i\})$ to be constant, and their ratio $P(\{p_i\})/P(\{y_i\}) = c$, we find the overall *a posteriori* probability function of background under condition of measured data to be:

$$P(B, \{p_i\}|\{y_i\}, N_{bt}) = c\frac{n}{\sqrt{2\pi N_{bt}}} \frac{1}{\prod_i^N \sigma_i \sqrt{2\pi}} e^{-(N_{bt}-Bn)^2/2N_{bt}} e^{-\chi^2/2}, \tag{5.9}$$

This overall *a posteriori* distribution includes all possible values for all parameters $\{p_i\}$ in the parameters' space. If we subtract the background B from the decay curve, keep the background fixed, and then minimize χ^2 with respect to all free parameters we obtain the maximum *a posteriori* distribution of the tru background and parameters, given the measured data and the background

$$P_{max}(B,\{p_i\}|\{y_i\},N_{bt}) = c\frac{n}{\sqrt{2\pi N_{bt}}}\frac{1}{\prod\limits_{i}^{N}\sigma_i\sqrt{2\pi}}e^{-(N_{bt}-Bn)^2/2N_{bt}}e^{-\chi^2_{min}/2}. \quad (5.10)$$

Maximizing the *a posteriori* distribution limits the value of parameters $\{p_i\}$ to the ones which are the most likely.

In the frequently used fitting routines by minimizing χ^2 the probability density is maximized, while when using Bayes theorem by including the *a priori* probability, *a posteriori* probability is maximized. The extra information that we include as prior information in the *a posteriori* distribution refines the parameters and therefore gives a more reliable result.

5.2.4 χ^2 credible interval and model consistency

The complete procedure for obtaining a parameter estimate from an arrival time histogram consists of the following three steps: First, we establish the *a priori* distribution probability of the background B Eq. (5.5). Second, within the credible region of background (Eq. (5.6)) we select background values and we calculate the best fit of the model to the data for each background value. Third, at each of the background values we calculate χ^2_{min} and obtain $P_{max}(B,\{p_i\}|\{y_i\},N_{bt})$. The maximum of this *a posteriori* probability defines the best fit value of the parameters.

χ^2 has a probability distribution known as "chi-square distribution". As the degrees of freedom, that is, the number of data used in the modeling procedure-increase, the chi-square distribution approaches a normal distribution and therefore the χ^2 credible interval is given by:

$$1-\sqrt{\frac{2}{n}} < \frac{\chi^2}{n} < 1+\sqrt{\frac{2}{n}}. \quad (5.11)$$

where n is the degrees of freedom. Time-resolved emission data sets are taken to be consistent, and thus maintained in the analysis, only if the minimum of χ^2 coincides within the credible region of the dark rate (Eq. 5.6) **and** the value of χ^2 lies within its own credible region (Eq. 5.11).

5.3 Experiment and applications

Time resolved emission of PbS quantum dots in the near infrared spectral range has been studied. The PbS quantum dots are suspended in toluene with concentration of 2.10^{-6} M/L. The quantum dots are excited by short laser pulses with a 11 ps duration at a wavelength of $\lambda = 532$ nm. The laser was operated at a repetition rate of 409 kHz. The dots emit at photon energies between 0.8 to 0.9 eV. Time-resolved emission is detected by means of time correlated single photon counting (TCSPC)[21, 29].

We have also performed time-resolved emission measurement of the same PbS quantum dots in 3D photonic band gap crystals [7]. The crystals are made of silicon and have a wide 3D band gap in the near infrared spectral region fabricated by CMOS-compatible method [31–34]. The photonic band gap is a range of frequencies in which light propagation is prohibited and therefore the spontaneous emission of light sources in the band gap is inhibited [35]. Therefore in addition to all difficulties mentioned in the introduction, the signal is further reduced due to a strong inhibition.

5.3.1 Near infrared quantum dots in suspension

To extract the decay rate of the quantum dots in suspension the decay curve is modeled using a single exponential model with two adjustable parameters, namely the overall intensity I and the decay rate γ_S (eq. (5.2)). We first fit the data using the conventional fitting method without considering any *a priori* information. To obtain the background we average over a few hundred time bins before the excitation laser pulse arrives. Subtracting the average background and keeping the background fixed results in a decay rate of $\gamma = 1.53 \mu\ s^{-1}$ with a goodness of fit $\chi^2_{red} = 0.898$.

We now examine the maximum *a posteriori* (MAP) method as described, to find the best fit to the data by using *a priori* information from the background. The background has a Gaussian distribution with mean value of averaged number of the background time bins and calculated standard deviation(σ). Due to the Gaussian probability distribution we expect the true value of the background to lie within the credible range of the background($\frac{N_{bt}}{n}$) ± one standard deviation with, 70% probability. We start from $B = \frac{N_{bt}}{n} - \sigma$, where $\sigma = \sqrt{N_{bt}}/n$, subtract it from the data and fit our single-exponential model to the data. From the fit we extract parameters and the goodness of fit and we calculate the posterior probability corresponding to this fit. We change the background in steps of $\sigma/6$ and smaller to cover the background confidence interval. For each background value optimize the rest of the parameters using a least square fitting routine, and then calculate $P_{max}(B, \{p_i\}|\{y_i\}, N_{bt})$.

Figure 5.2 shows the *a posteriori* probability function $P_{max}(B, \{p_i\}|\{y_i\}, N_{bt})$ as a function of background parameter B that is varied within its credible range. The *a posterior* probability is low for most B, indicating that these values are not relevant. Between 0 to $\sigma/6$ background values, the posterior probability is maximum giving the best parameter estimate where the decay rate is $\gamma = 1.53\ \mu s^{-1}$. For other background values the posterior probability is small. The decay rate changes only from $\gamma = 1.54\ \mu s^{-1}$ for $\frac{N_{bt}}{n} - \sigma$ to $\gamma = 1.52\ \mu s^{-1}$ for $\frac{N_{bt}}{n} + \sigma$ background that is not very different compared to the best estimated decay rate. The goodness of fit lies within its credible range. Therefore the result of this fitting gives $\gamma = 1.53\ \mu s^{-1}$ as decay rate for the most likely fit with goodness of fit 0.898. As we see the result from the Bayesian analysis matches very well with the normal fitting and in the both cases we obtain the same decay rate. Therefore we conclude that when the background level is high and there is a high signal on top of the background, the results of the conventional fitting procedure agrees with the Bayesian method.

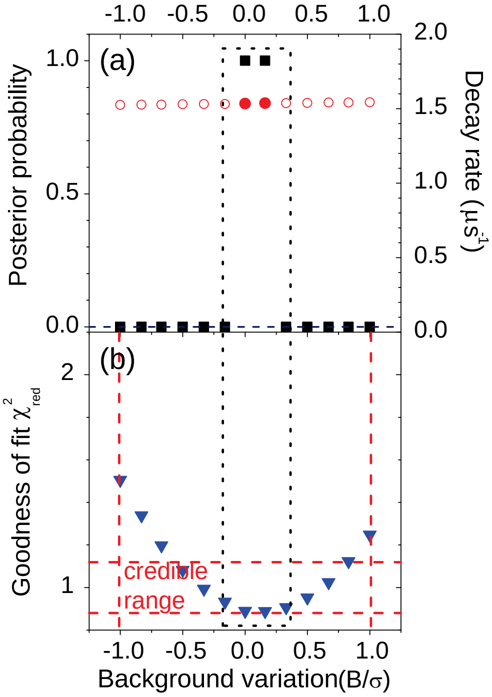

Figure 5.2: Maximum *a posteriori* estimation analysis of the time-resolved emission of the suspension of PbS quantum dots in the near-infrared range. (a) Overall *a posteriori* probability function $P_{max}(B, \{p_i\}|\{y_i\}, N_{bt})$ (black squares) versus background parameter B normalized to background standard deviation σ. The background is varied within the credible range given by Eq. (5.6). Red circles show the decay rate (right axis). The probability is maximum for two backgrounds value, determining the most probable background values and decay rates. (b) Reduced goodness of fit χ^2_{red} (blue inverted triangles) versus B. The black dashed rectangle emphasizes the range of B where simultaneously the probability is 1 and the goodness of fit is within its credible range, thus determining the consistent decay rate range.

5.3.2 Near infrared quantum dots in a 3D photonic band gap

In this subsection we examine the method for data sets, where in addition to the high background the signal level is very low. To probe the density of states inside a photonic band gap crystal we immersed the 3D silicon crystal in a diluted suspension of quantum dots in toluene. The crystal is surrounded by quantum dots suspension, therefore always some emission signal that originates from the suspension is collected and contributes to the time-resolved data. We have measured-time resolved emission at different energies within the quantum dot spectrum where the spectrum overlaps with the photonic band gap. Since the emission originates both from quantum dots in the crystal and in suspension, we model the time-resolved emission with a double-exponential [7]:

$$f(t) = I_0(S \cdot \gamma_0 \cdot exp(-\gamma_0 t) + PC \cdot \gamma \cdot exp(-\gamma t)). \tag{5.12}$$

Here γ is the emission rate of quantum dots in the photonic crystal that we wish to obtain, and γ_0 is the rate of dots outside the crystal that is separately measured to be $\gamma_0 = 1.53\ \mu s^{-1}$. S and PC are relative factors fixed by scans of the detection focus, and only γ and I are adjusted parameters. We call the ratio of decay rate of dots inside the crystal to the decay rate of dots outside the crystal (γ/γ_0) as inhibition [7]. We examine the analysis on two data sets which correspond to the wavelengths in the band gap of the photonic crystal where the number of detected photon is very low compare to huge number of background. Time-resolved emission data was obtained at 0.893 eV, in two different photonic crystals. Based on Bayes' theorem we analyzed the data to find the true value of the background and therefore the correct decay rate.

Figure 5.3(I) shows the *a posteriori* probability function $P_{max}(B, \{p_i\}|\{y_i\}, N_{bt})$ for the 1st set as a function of background parameter B that is varied within its credible range. By changing the background the γ and therefore the inhibition changes. The *a posteriori* probability is low for most B, indicating that these values are not relevant. Between 0.5 to 0.75, however, the probability is 1, therefore the concomitant inhibitions appear credible. Indeed, the corresponding goodness of fit also lies within its credible range as set by Eq. (5.11). Therefore, we conclude for this data set that the credible inhibition lies between 2.8 and 17.3, yielding a final result $\gamma_0/\gamma = 10.0 \pm 7.2$.

Figure 5.4 illustrates result of fitting the same data set with two different background subtractions. Figure 5.4 (a), we subtract $\frac{N_{bt}}{n} + 3\sigma/4$ as background, and fit a bi-exponential function, obtaining $\gamma_0 = 17.3\gamma$. The residuals are centered around zero and minimized χ^2_{red} close to 1 and within its credible range, indicating a good fit. As all the conditions are satisfied we accept this value of the background as true background value. In figure 5.4 (b), we subtract $\frac{N_{bt}}{n} - \sigma/2$ as background, and fit with a bi-exponential function, obtaining $\gamma_0 = 3\gamma$. The residuals are not centered around zero and minimized χ^2_{red} lies outside the credible range, indicating a bad fit and a wrong background value as illustrated in Fig. 5.3(I).

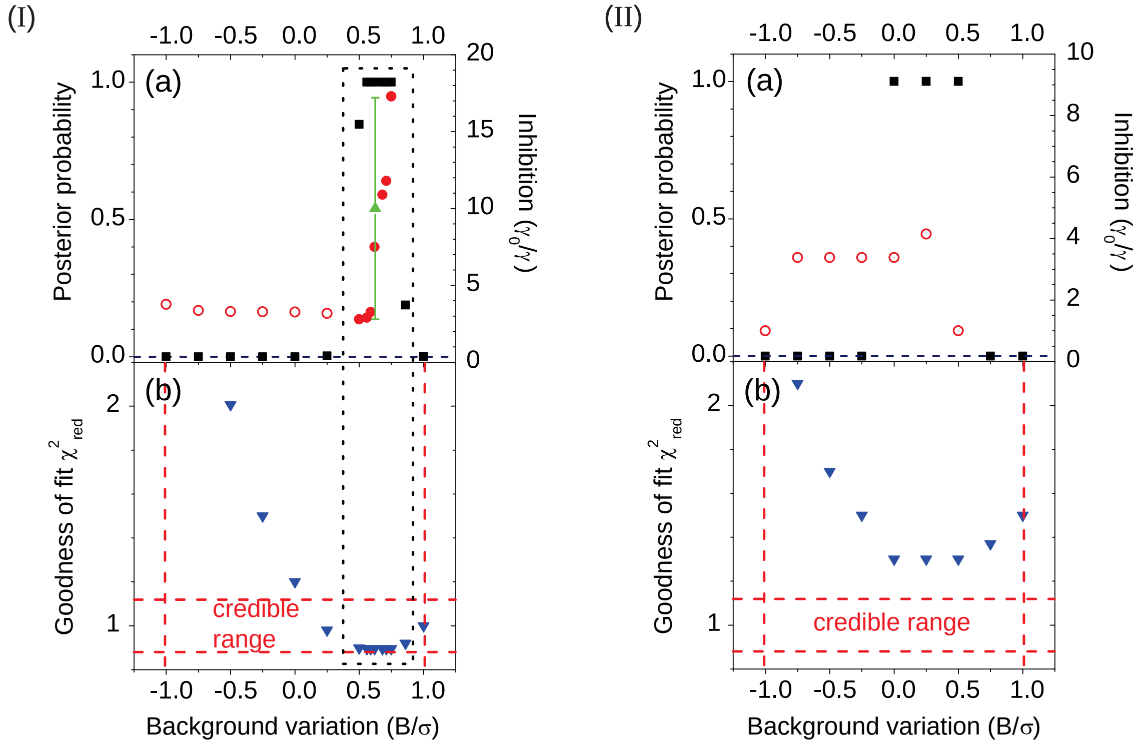

Figure 5.3: Maximum *a posteriori* estimation analysis of the time-resolved emission of the near-infrared PbS quantum dots in a 3D photonic band gap crystal. I(a) Overall *a posteriori* probability function $P_{max}(B, \{p_i\}|\{y_i\}, N_{bt})$ (black squares) versus background parameter B normalized to background standard deviation σ for emission data obtained at 0.893 eV. The background is varied within the credible range given by Eq. (5.6). Red circles show the simultaneously resulting inhibition γ_0/γ (right axis). Red closed circles are credible inhibitions that yield the final result shown as the green triangle with error bars. I(b) Reduced goodness of fit χ^2_{red} (blue inverted triangles) versus B. The black dashed rectangle emphasizes the range of B where simultaneously the posterior probability is high and the goodness of fit is within its credible range, thus determining the consistent inhibition range. II(a) Overall *a posteriori* probability function $P_{max}(B, \{p_i\}|\{y_i\}, N_{bt})$ (black squares) versus background parameter B/σ. The background is varied within the credible range. Red open circles show the simultaneously resulting inhibition γ_0/γ (right axis). II(b) Reduced goodness of fit χ^2_{red} (blue inverted triangles) versus B. Since the minimum of the χ^2_{red} is not within its credible range, this data set is inconsistent with the assumptions and thus excluded.

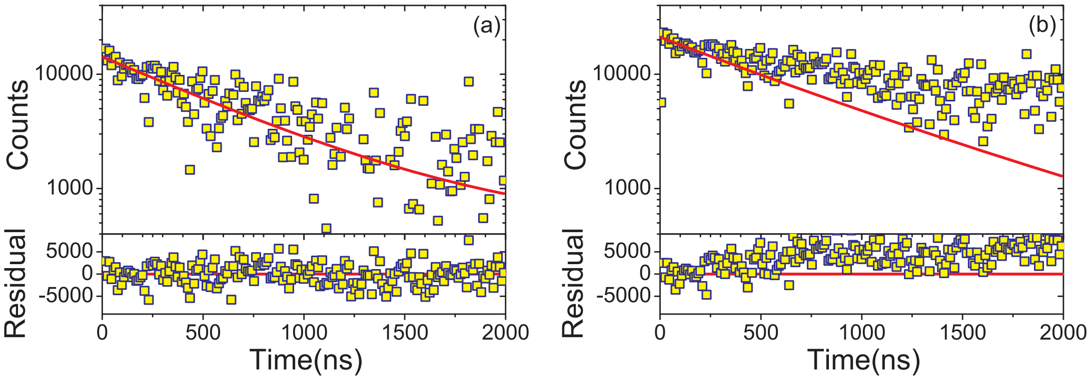

Figure 5.4: comparison of one near infrared data set ($\lambda = 1390nm$) with different background subtraction. (a) Subtracting of ($\frac{N_{bt}}{n} + 3\sigma/4$) as background yields the best fit with residuals centered around zero and a minimized χ^2_{red} within credible range. (b) Subtracting of ($\frac{N_{bt}}{n} - \sigma/2$) as a background yields residuals that are not centered around zero and a χ^2_{red} outside the credible range.

Figure 5.3(II) shows the *a posteriori* function $P_{max}(B, \{p_i\}|\{y_i\}, N_{bt})$ for the 2nd data set of the time-resolve emission measurement of PbS quantum dots in the photonic bandgap crystal versus background parameter B within its credible range. *A posteriori* probability is maximized for background values within 0 to 0.5 as χ^2_{red} is minimized. As we explained in Eq. 5.11, χ^2 has a credible range and data is credible if minimum of χ^2 is within this range. While here for this data set the minimum value for goodness of fit is outside of its credible range, hence this data set is excluded as a possible observation of inhibition in the photonic band gap.

Using this criteria about 40% of the data sets of time resolved measurements in the band gap for the near infrared range yielded inconsistent fits, which is only slightly higher than statistically expected. These results were thus excluded. Since we only include one standard deviation of the Gaussian distribution, and probability of finding the true background value within one standard deviation for a Gaussian distribution is 68%, therefore theoretically with 32% probability we get an inconsistent fit. There are several possible reasons for the extra inconsistency. In a number of our time-resolved emission measurements, we have observed that drifts of alignment and count rate occur, due to environmental changes during the long hours data collection time. This leads to non-Poissonian systematic errors in the measured data, giving rise to skewed residuals and elevated values of χ^2, and an inconsistency between the dark measurement and the histogram. In addition, our model for the time-resolved emission in the near infrared range gives the simplest possible description for emission in a photonic band gap crystal. Therefore, the model does not capture possible effects such as inhomogeneous spatial distribution of light sources, or slow non-exponential decay of the quantum dots predicted by Ref. [36, 37].

5.4 Simulation

Up to now we have investigated the situation where among all parameters only background has an significant uncertainty. In cases where other parameters also have uncertainty then we should process those parameters in the same way that we used here for the background. Here we present a Markovian Chain Monte Carlo (MCMC) simulation technique that is used in the more general cases where we have a multi-parameters model and there exist more than one parameter with uncertainty. Given a set of data, model and prior information for parameters, all MCMC algorithms generate the posterior probability distribution. The desired posterior distribution is sampled by constructing a random walk in the model parameter space, such that the probability for being in a region of the space is proportional to the posterior density for that region. Here the random walk is accomplished using a Markov chain. In the case of a decay curve with 3 parameters namely background, decay rate and overall intensity we have a 3 dimensional parameter distribution, but we can plot such a parameter distribution for each 2 parameters in a 2 dimensional plot. Figure 5.5 shows a 2 dimensional posterior parameter correlation distribution plot of the background and the decay rate for the data set shown in Fig. 5.1.

Figure 5.5 illustrates the effect of including prior information of the background on the posterior parameters distribution. From Bayes' theorem the posterior parameter correlation distribution is proportional to product of prior distribution and likelihood of the parameters. If no prior information is given then the posterior density region is the same with likelihood density distribution that is optimized when using conventional fitting routines. Figure 5.5 shows the effect of including prior information in the analysis procedure. In Fig. 5.5(a) a uniform distribution has been used for the background B as prior information. A uniform distribution is a distribution that has a constant probability. Since the uniform distribution is a flat distribution, applying it as a prior probability distribution does not change the posterior probability distribution compared to the likelihood of the parameters that would be maximized in conventional fitting routine. For this example the posterior probability is widely distributed over a large range of decay rates with three high probability regions indicated with black arrows. As we see from Fig. 5.5 even if we estimate the background correctly we can end up with any value for the decay rate since the decay rate is widely distributed with high probability.

In figure 5.5(b) the prior background distribution is a normal distribution with center of the average background value calculated from the data. Multiplying this prior background distribution to the likelihood of the parameters, pushes the posterior probability down and changes the distribution. The posterior distribution becomes more concentrated in a more confined range of decay rates indicated with the black arrow. In this parameter probability distribution we can estimate the decay rate more precisely since we have only one region of high probability if we estimate the correct background. Incorporating this *a priori* information also illustrates the advantage of using Bayesian method rather than the conventional fitting routine. This posterior distribution contour also helps to visualize how the parameters are distributed and how they are correlated.

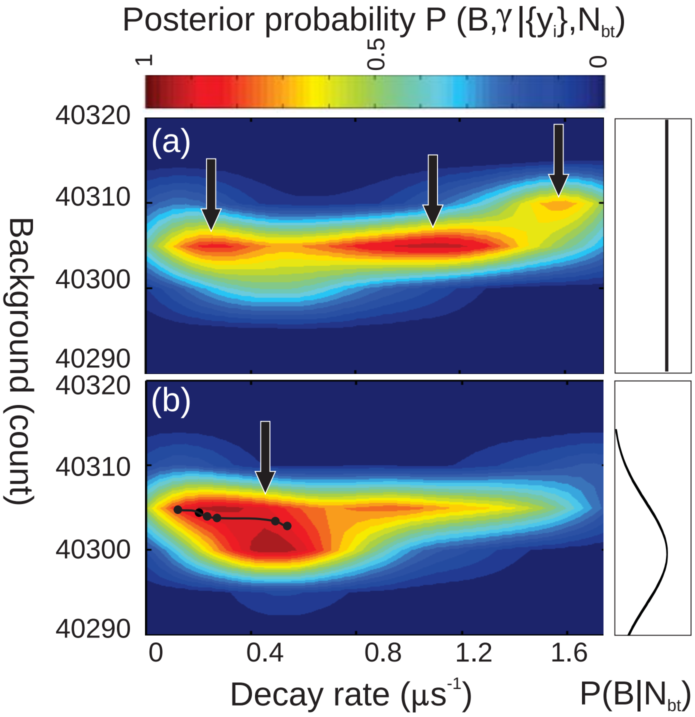

Figure 5.5: Posterior probability distribution plotted for two different prior distributions (Eq. 5.9). (a) Prior distribution is a uniform distribution. Since a uniform distribution is a flat distribution, the posterior distribution in this case is comparable with likelihood of the parameters that in conventional fitting routine would be maximized. The black arrows indicate the high probability regions. (b) Prior distribution is a normal distribution with center of average background value. By applying the normal distribution as prior the posterior distribution has changed and becomes more concentrated in a range of decay rate values. The black circles show maximized posterior probability of decay curve where background is kept fixed.

5.5 Conclusion

We have investigated the difficulties encountered in time-resolved emission measurements in the near infrared which are caused by low intrinsic count rate and high intrinsic background. Clearly, extracting parameters from the time-resolved emission measurement is much more difficult in the near infrared spectral region than in the visible. We discussed the importance of statistical analysis in the case of low signal to noise ratio in the infrared range. The high level of background in the near infrared measurement can lead to a wrong decay time determination, therefore it is crucial to find the true value of the background. Using Bayesian method, by incorporating prior information on the background, we are able to find the true background and estimate the most likely decay rate. This method provides a robust analysis and interpretation of the near infrared time-resolved emission when the background level is high and the signal level is low. We have illustrated our method with the successful analysis of time-resolved emission of PbS quantum dots in suspension and in 3D photonic band gap crystals.

Bibliography

[1] E. Fermi, *Quantum theory of radiation*, Rev. Mod. Phys. **4**, 87 (1932). — p.73.

[2] L. Novotny and B. Hecht, *Principles of nano-optics* (Cambridge University Press, New York, 2006). — p.73.

[3] E. Lifshitz, M. Brumer, A. Kigel, A. Sashchiuk, M. Bashouti, M. Sirota, E. Galun, Z. Burshtein, A. Q. Le Quang, I. Ledoux-Rak, and J. Zyss, *Air-stable PbSe/PbS and PbSe/PbSexS1-x core-shell nanocrystal quantum dots and their applications.*, J. Phys. Chem. B **110**, 25356 (2006). — p.73.

[4] E. H. Sargent, *Infrared quantum dots*, Adv. Mater. **17**, 515 (2005). — p.73.

[5] G. T. Reed, *Elements of modern x-ray physics, second edition* (John Wiley, Chichester, UK, 2008). — p.73.

[6] S. Ogawa, M. Imada, S. Yoshimoto, M. Okano, and S. Noda, *Control of light emission by 3d photonic crystals*, Science **305**, 227 (2004). — p.73.

[7] M. D. Leistikow, A. P. Mosk, E. Yeganegi, S. R. Huisman, A. Lagendijk, and W. L. Vos, *Inhibited spontaneous emission of quantum dots observed in a 3D photonic band gap*, Phys. Rev. Lett. **107**, 193903 (2011). — p.73, 79, 80, 81.

[8] R. D. Schaller and V. I. Klimov, *High efficiency carrier multiplication in pbse nanocrystals: Implications for solar energy conversion*, Phys. Rev. Lett. **92**, 186601 (2004). — p.73.

[9] K. Inoue, H. Sasaki, K. Ishida, Y. Sugimoto, N. Ikeda, Y. Tanaka, S. Ohkouchi, Y. Nakamura, and K. Asakawa, *InAs quantum-dot laser utilizing GaAs photonic-crystal line-defect waveguide*, Opt. Express **12**, 5502 (2004). — p.73.

[10] N. Yamamoto, K. Akahane, S. Gozu, A. Ueta, and N. Ohtani, *1.55 μm-waveband emissions from Sb-based quantum-dot vertical-cavity surface-emitting laser structures fabricated on GaAs substrate*, Jpn. J. Appl. Phys. **45**, 3423 (2006). — p.73.

[11] S. Hoogland, V. Sukhovatkin, I. Howard, S. Cauchi, L. Levina, and E. H. Sargent, *A solution-processed 1.53 μm quantum dot laser with temperature-invariant emission wavelength*, Opt. Express. **14**, 3273 (2006). — p.73.

[12] N. Tessler, V. Medvedev, M. Kazes, S. Kan, and U. Banin, *Efficient near-infrared polymer nanocrystal light-emitting diodes*, Science. **22**, 1068153 (2002). — p.73.

[13] C. E. Finlayson, A. Amezcua, P. J. A. Sazio, P. S. Walker, M. C. Grossel, R. J. Curry, D. C. Smith, and J. J. Baumberg, *Infrared emitting pbse quantum-dots for telecommunications-window applications*, J. Mod. Optics. **52**, 955 (2005). — p.73.

[14] E. Holder, N. Tesslerb, and A. L. Rogach, *Hybrid nanocomposite materials*

with organic and inorganic components for opto-electronic devices, J. Mater. Chem. **18**, 1064 (2008). — p.73.

[15] A. P. Alivisatos, *Less is more in medicine*, J. Sci. Am. **285**, 66 (2001). — p.73.

[16] R. Weissleder and M. J. Pittet, *Imaging in the era of molecular oncology*, Nature. **452**, 580 (2008). — p.73.

[17] X. Michalet, F. F. Pinaud, L. A. Bentolila, A. M. Wu, S. S. Gambhir, and W. S., *Quantum dots for live cells, in vivo imaging, and diagnostics*, Science. **307**, 538 (2005). — p.73.

[18] R. E. Bailey and S. Nie, *Alloyed semiconductor quantum dots: Tuning the optical properties without changing the particle size*, J. Am. Chem. Soc. **23**, 7100 (2003). — p.73.

[19] H. Qian, C. Dong, J. Peng, X. Qiu, Y. Xu, and J. Ren, *High-quality and water-soluble near-infrared photoluminescent CdHgTe/CdS quantum dots prepared by adjusting size and composition*, J. Phys. Chem. C **45**, 1685216857 (2007). — p.73.

[20] K. Aoki, D. Guimard, M. Nishioka, M. Nomura, S. Iwamoto, and Y. Arakawa, *Coupling of quantum-dot light emission with a three-dimensional photonic-crystal nanocavity*, Nature Photon. **2**, 688 (2008). — p.73.

[21] W. Becker, *Advanced time-correlated single photon counting techniques* (Springer, New York, 1992). — p.74, 75, 78.

[22] D. Stucki, G. Ribordy, A. Stefanov, H. Zbinden, J. G. Rarity, and T. Wall, *Photon counting for quantum key distribution with peltier cooled InGaAs/InP APDs*, J. Mod. Opt. **48**, 1967 (2001). — p.74.

[23] S. N. Dorenbos, P. Forn-Diaz, T. Fuse, A. H. Verbruggen, T. Zijlstra, T. M. Klapwijk, and V. Zwiller, *Low gap superconducting single photon detectors for infrared sensitivity*, Appl. Phys. Lett. **98**, 251102 (2011). — p.74.

[24] B. P. Roe, *Probability and statistics in experimental physics* (Springer, New York, 1992). — p.75.

[25] P. M. Lee, *Bayesian statistics* (Hodder, London, 2004). — p.75, 76.

[26] P. C. Gregory, *Bayesian logical data analysis for physical science, a comparative approach with mathematica support* (Cambridge University Press, England, 2005). — p.75, 76.

[27] C. P. Robert, *The bayesian choice: From decision theoretic foundations to computational implementation* (Springer, New York, 2007). — p.75, 77.

[28] A. F. van Driel, I. S. Nikolaev, P. Vergeer, P. Lodahl, D. Vanmaekelbergh, and W. L. Vos, *Statistical analysis of time-resolved emission from ensembles of semiconductor quantum dots: Interpretation of exponential decay models*, Phys. Rev. B **75**, 035329 (2007). — p.75.

[29] J. Lakowicz, *Principles of fluorescence spectroscopy* (Kluwer Academic, New York, 1999). — p.75, 78.

[30] A. Sen and M. Srivastava, *Regression analysis* (Springer, New York, 1990). — p.77.

[31] S. R. Huisman, R. Nair, L. A. Woldering, M. D. Leistikow, A. P. Mosk, and W. L. Vos, *Signature of a three-dimensional photonic band gap observed on silicon inverse woodpile photonic crystals*, Phys. Rev. B **83**, 205313 (2011).

— p.79.

[32] L. A. Woldering, R. W. Tjerkstra, H. V. Jansen, I. D. Setija, and W. L. Vos, *Periodic arrays of deep nanopores made in silicon with reactive ion etching and deep UV lithography*, Nanotechnology **19**, 145304 (2008). — p.79.

[33] R. W. Tjerkstra, L. A. Woldering, J. M. van den Broek, F. Roozeboom, I. D. Setija, and W. L. Vos, *Method to pattern etch masks in two inclined planes for three-dimensional nano- and microfabrication*, J. Vac. Sci. Technol. B **29**, 061604 (2011). — p.79.

[34] J. M. van den Broek, L. A. Woldering, R. W. Tjerkstra, F. B. Segerink, I. D. Setija, and W. L. Vos, *Inverse-woodpile photonic band gap crystals with a cubic diamond-like structure made from single-crystalline silicon*, Adv. Funct. Mater. **22**, 25 (2012). — p.79.

[35] E. Yablonovitch, *Inhibited spontaneous emission in solid-state physics and electronics*, Phys. Rev. Lett. **58**, 2059 (1987). — p.79.

[36] N. Vats, S. John, and K. Busch, *Theory of fluorescence in photonic crystals*, Phys. Rev. A **65**, 043808 (2002). — p.83.

[37] P. T. Kristensen, A. F. Koenderink, P. Lodahl, B. Tromborg, and J. Mork, *Fractional decay of quantum dots in real photonic crystals*, Opt. Lett. **33**, 1557 (2008). — p.83.

CHAPTER 6

Probing photonic crystals with shaped wavefronts

6.1 Introduction

Photonic crystals are periodic structures with a period in the order of the wavelength of light [1]. In an infinite photonic crystal a wave can propagate only when it satisfies the Bloch condition due to periodicity. Therefore all modes in an infinite crystal are Bloch modes. Due to the constructive interference of light which is reflected from certain families of lattice planes, stop gaps appear: frequency ranges where no mode propagates inside the crystal in a particular direction. A real crystal has of course a finite extent as studied in 3 and Ch. 4. To investigate light transport in a real photonic crystal, light is typically shone on the crystal from free space. The first interaction of light with the crystal takes place at the surface, where light can partially couple into the crystal depending on the position where light is launched as well as the wavelength and polarization [2, 3]. Light that enters the crystal couples to many Bloch modes and propagates in different directions inside the crystal. In addition to surface effects, a real photonic crystal has structural variation in size and position of the building blocks. Although with state of the art fabrication the disorder and defects are very well controlled, fabrication of a perfect periodic structure without disorder is impossible. These deviations from perfect periodicity cause scattering, and hence exponential attenuation of coherent beams propagating through photonic crystals [4, 5]. Therefore in a real photonic crystal with disorder, transport of the coupled light into crystals results in an interplay between diffuse scattering due to the disorder and Bloch wave propagation. This fact influences the industrial applications of photonic crystal devices such as high-efficiency light emitting diodes [6], low threshold lasers [7], ultralow-loss waveguides, and corrupts the functionality of photonic integrated circuits [5, 8].

Photonic crystals are made either by self-assembly processes such as opal crystals [9–14] or by top-down procedures such as etching or deposition that yields for instance woodpile and inverse woodpile photonic crystals [15–23]. Artificial opals are synthesized from a relatively high concentration of nanoparticles in suspension. Particles in the suspension sediment in time to form a colloidal crystal. When the liquid between the particles is evaporated, one obtains an opal photonic crystal consisting of close-packed particles with air in between. Even under controlled conditions such as controlled temperature, humidity, and particle concentration, disorder is introduced by size polydispersity of the particles. On top of that during the liquid evaporation cracks may appear in the crystals,

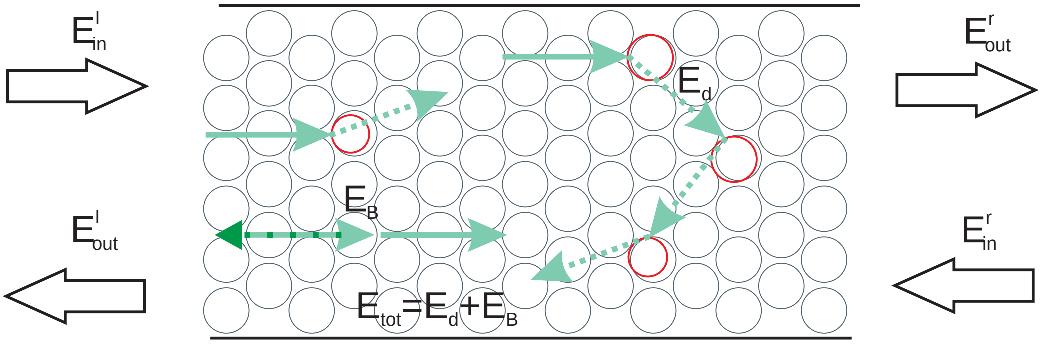

Figure 6.1: Schematic representation of light scattering in a real photonic crystal. The red circles show the deviations from a perfect crystal and are representing disorder. The incoupled field E_{tot} consists of Bloch waves E_{B} typical of propagation in a perfect crystal and the scattered field E_{d} due to the disorder in the crystal. E^r_{in} and E^l_{in} are the fields in free space incident on the sample from right and left, respectively and E^r_{out} and E^l_{out} are the outgoing fields in free space on right and left side, respectively.

breaking the large colloidal single crystal into smaller grains, although several groups have made good progress to “crack-free opals” [24]. If crystals are made using top-down fabrication methods, the disorder can be controlled within a few nanometer resolution. Crystals such as inverse woodpiles that have been studied in this thesis are fabricated with a procedure to reduce the size polydispersity and position disorder of the pores. Since in this case the crystal size depends on the mask size and the fabrication procedure, the crystal is a single crystal throughout the entire crystal volume.

In this chapter we study different processes involved in light transport in both opals and two-dimensional silicon photonic crystals using a correlation microscopy method. We aim to distinguish the two different processes of light propagation in photonic crystals after it has entered inside the crystal. We denote by E_{tot} the total field inside the crystal transmitted through the surface, which consists of the sum of Bloch wave propagation typical of a perfect crystal with field E_{B}, and randomly scattered light due to disorder with field E_{d}:

$$E_{\text{tot}} = t_{\text{surf}} E_{\text{in}} = E_{\text{B}} + E_{\text{d}} \tag{6.1}$$

where t_{surf} is the fraction of light that enters to the crystal through the surface, and E_{in} is the incident field. Figure 6.1 shows a schematic representation of incident and transmitted field in a real photonic crystal sample. Inspired by mesoscopic wave propagation in optics or in electronics, we propose to use the scattering matrix representation to consider the scattering matrix of the crystal [25] to quantitatively interpret our results.

$$\begin{pmatrix} E^l_{\text{out}} \\ E^r_{\text{out}} \end{pmatrix} = S \begin{pmatrix} E^l_{\text{in}} \\ E^r_{\text{in}} \end{pmatrix} \tag{6.2}$$

with E^r_{in} and E^l_{in} the fields in free space incident on the sample from right and left, respectively, and E^r_{out} and E^l_{out} are the outgoing fields in free space on the right and left side, respectively. S is the scattering matrix equal to

$$S = \begin{pmatrix} R^l & T^{rl} \\ T^{lr} & R^r \end{pmatrix} \tag{6.3}$$

with R^l the reflection matrix on the left side of the sample, R^r the reflection matrix on the right side of the sample, T^{rl} the transmission matrix from right to the left and T^{lr} the transmission matrix from left to the right. In this chapter only R^l is considered. For simplicity we represent R^l as R and call it the reflection matrix of the sample, where $E^l_{\text{out}} = RE^l_{\text{in}}$. Using singular value decomposition, the reflection matrix R can be written as a product of three matrices [26]

$$R = U\mathcal{R}U^\dagger. \tag{6.4}$$

Here, the matrices U and $U^\dagger$ are the unitary matrices with complex elements which represent the incoupling to the crystal from free space and the outcoupling from the crystal to free space, respectively, and $\mathcal{R}$ is a diagonal matrix with real, positive elements which are singular values corresponding to reflection eigenchannels of the crystal. We propose $\mathcal{R}$ is an addition of singular values $\mathcal{R}_\text{B}$ originating from the stop gaps, and singular values $\mathcal{R}_\text{d}$ due to the disorder. The contribution of a Bloch mode to the maximum reflectivity channel is given by the innerproduct of the spatial field profile of the Bloch mode with the field distribution of the channel in the spirit of Ref. [27].

By measuring the reflected field from the crystal we observe optical correlations in the wave structures which are attributed to the Bloch propagating field E_B and scattered field due to disorder E_d. The disorder in a crystal, such as size or position variations, results in the scattering of a Bloch mode. The scattered light is likely distributed over all other Bloch modes. This picture assumes that the scattering mean free path is greater than the Bragg length $\ell_\text{sc} > \ell_\text{Bragg}$, which is physically reasonable since otherwise a photonic crystal is so disordered that it does not reveal gaps anymore, see Ref. [5]. Since disorder is randomly distributed throughout the crystal, the E_d fields are Bloch modes, their contribution is random with position in the crystal. Here we neglect the waves that have a very large Bragg length and therefore propagate a long distance inside the crystal before they couple to a Bloch mode. Our aim is to distinguish the fraction of E_B and E_d in different photonic structure and understand the complex behavior of light propagation in photonic crystal due to long range order and disorder in the structures. We investigate short range and long range order in both opal and 2D silicon crystals and we compare our results with a completely random structure. We also probe the transport of light in the crystals with different wavefronts using wavefront shaping method. The wavefront shaping and focusing of light into the crystal help to understand how light goes inside and how it behaves inside a real crystal.

6.2 Wavefront shaping setup and samples

The measurements described in this chapter have been performed using a setup which is notably used for wavefront shaping experiments [28]. Figure 6.2 shows a

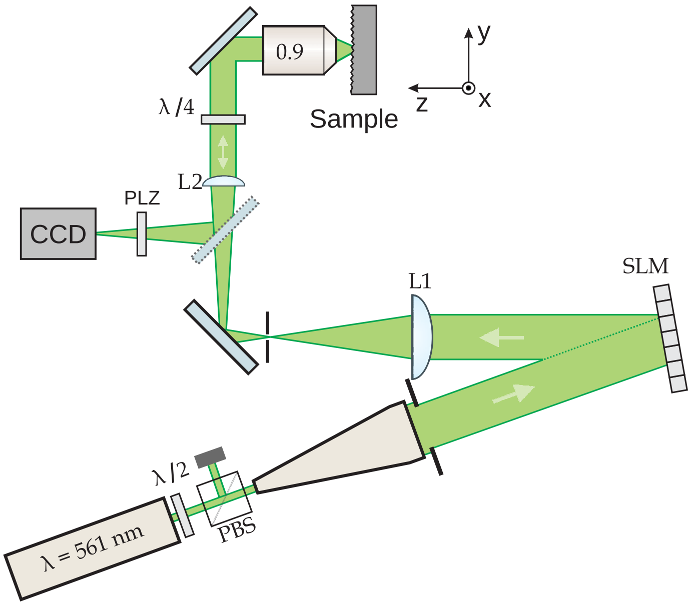

Figure 6.2: Schematic illustration of the wavefront shaping setup. A laser with wavelength $\lambda = 561\ nm$ is used as light source. The laser beam passes through a half wave plate ($\lambda/2$) and a polarizer beam splitter (PBS) to obtain a known incident polarization. The beam is expanded using a beam expander to cover an area of 8 mm by 8 mm on the spatial light modulator (SLM). Light that is reflected back from the SLM passes through $L1$ lens and is spatially filtered using an aperture. The laser light is then focused on the sample surface using a high numerical aperture objective with $NA = 0.9$. A camera is in the imaging configuration to image the sample surface. A polarizer and a quarter wave-plate are placed in the reflection path to filter the direct reflection from the sample surface. For alignment purposes a white light source illuminates the sample surface.

schematic illustration of the setup. A $\lambda = 561\ nm$ cw laser is used as light source. The laser beam passes through a polarizer beam splitter (PBS) and a half wave plate ($\lambda/2$) to obtain a known incident polarization. The laser beam is expanded using a beam expander to cover a 8 mm by 8 mm area on the spatial light modulator (SLM, Holoeye phase only). In case the SLM is “on” we modulate the wavefront of light to a desired wavefront, otherwise it is “off” and acts as a reflecting mirror. Light that is reflected back from the SLM passes through $L1$ and is spatially filtered using an aperture. The laser light then is focused on the sample surface using a high numerical aperture objective with NA=0.9. The diameter of focus is calculated to be about 300 nm. A CCD camera (Dolphin F-145B) is in the imaging configuration to image the sample surface. A polarizer and a quarter wave-plate are placed in the reflection path to filter the direct reflection from the sample surface as well as single single scattering from the sample [29, 30]. For alignment purposes a white light source is used to illuminate the sample surface [28].

In the experiments we have studied synthesized opals made of silicon dioxide colloidal spheres with radius $R = 349\ nm$ grown on silicon wafer, as studied

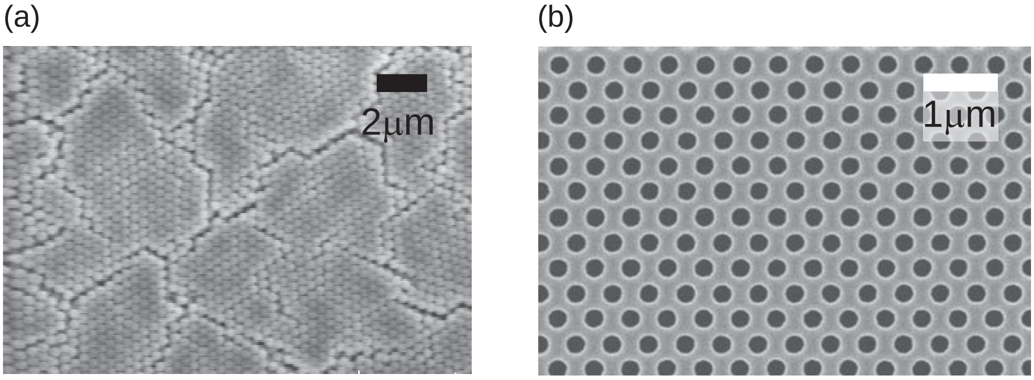

Figure 6.3: (a) Scanning electron micrograph of a 3D opal crystal of silicon dioxide spheres with radius $R = 349$ nm grown on a silicon wafer. The opal crystal consists of a lot of small islands separated by grain boundaries. (b) Scanning electron micrograph of top-down fabricated two dimensional silicon photonic crystal with centered rectangular lattice.

in Ref. [31, 32]. The opals have a stop gap of only 5% relative band width in the $\Gamma - L$ direction. Figure 6.3 (a) shows a scanning electron microscope image of an opal crystal grown on a silicon wafer. The opal crystal consists of small grains of typically $5 \mu m$ in diameter which are created during the growth process. The $\lambda = 561$ nm laser light used for the illumination has a energy close to the second stop gap of the opal crystal. To compare samples with small crystal domains with large single crystals, we also perform measurements on two-dimensional (2D) silicon crystals with centered rectangular lattice as shown in Fig. 6.3 (b). The 2D crystal is realized by etching pores using reactive ion etching in silicon wafers [21, 33]. The large single crystal is defined by deep UV step scan lithography [33]. The measurements on 2D crystals are done in the perpendicular out of plane direction with zero in-plane wavevector where the crystal has a stop gap at the Γ point. The $\lambda = 561$ nm laser light used for the illumination has a higher energy than the 2D silicon stop gap.

The sample is fixed on a two dimensional stage that has a travel range of 100 μm by 100 μm with a step size of 100 nm in the plane perpendicular to the optical axis of the objective. For the focusing and alignment purpose the objective is mounted on a manual stage with accuracy of 0.1 μm.

For the reference measurements we have used a completely random and disordered sample of polydisperse ZnO nanoparticles with average grain size of 200 nm. The ZnO sample is a 10 μm thick layer of dense nanoparticles deposited on a microscope glass slide by spray painting [28]. Considering the transport mean free path of the ZnO layer that is 0.7 ± 0.2 μm this thickness is sufficient to make the sample multiple scattering.

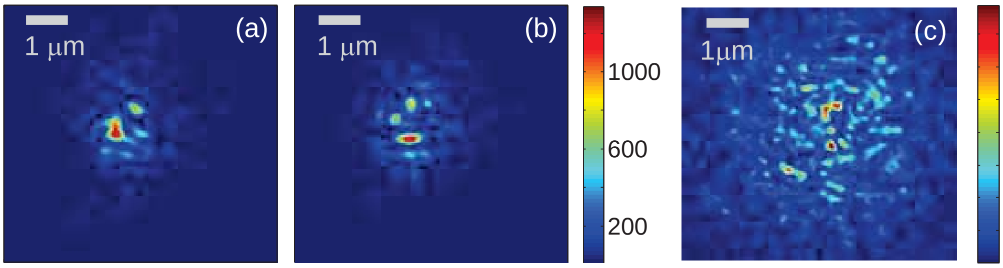

Figure 6.4: CCD camera images of the opal and ZnO samples illuminated with laser light. (a) and (b) recorded images at two different positions on the opal. The CCD images show a main bright intensity spot in the middle surrounded with random scattered light with no obvious periodicity. (c) Speckle pattern recorded from ZnO sample when illuminating with the laser light.

6.3 Multiple scattering in presence of long-range order

In this section we will distinguish light propagation due to long-range order and disorder in real photonic crystals. First, we use opal photonic crystals grown on the silicon wafer for the experiments. Collimated plane waves are sent to the back aperture of the illumination objective to focus light on the surface of the photonic crystal. The Gaussian beam that is sent to the sample partially couples into the Bloch waves in the crystal and propagates inside the crystal in different directions and partially scatters to other Bloch modes and change direction due to scattering by disorder. The recorded reflected intensities at two different positions on the crystal surface are shown in Figs. 6.4 (a) and (b). The images consist of a bright focus in the middle surrounded by scattered light. Fig. 6.4 (c) is the reflected speckle pattern from the ZnO sample. Although the scattered light from the photonic crystal sample looks (very) random due to the contribution of E_d, it is strikingly different from speckle pattern obtained from ZnO scattering layer. First of all due to the smaller amount of randomness in the crystal, the mean free path is longer resulting in a deeper traveling of the light inside the sample and a slower diffusion compared to the ZnO sample, thus the whole intensity pattern from the crystal has a smaller area than the one from the ZnO. Secondly, in the middle of the crystals' pattern a main reflected spot is seen that is absent in the ZnO sample. The main reflected spot is mostly caused by the periodicity in the crystal.

To quantitatively compare the scattered light patterns we have plotted the intensity distribution of the scattered light obtained from the opal crystal and the ZnO layer in Fig. 6.5. The distribution of speckle intensity of a random multiple scattering medium shows an exponential trend with the intensity. It is known that the distribution of the speckled light from random media follows a Rayleigh distribution [34]. We therefore fit a Rayleigh distribution model to the data with a mean value $< I >= 108.5$ calculated from the data, that matches excellently to the Rayleigh statistics. To compare the intensity distribution from

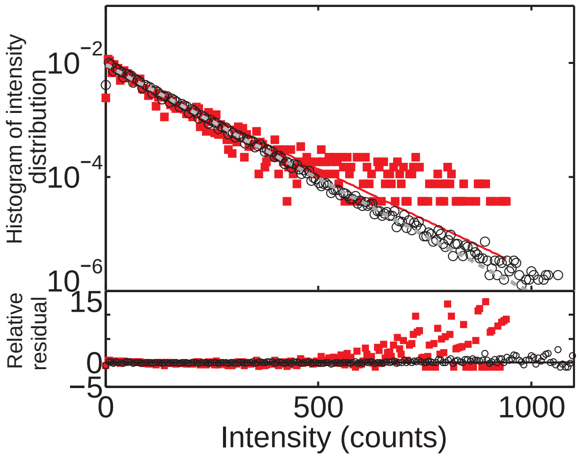

Figure 6.5: Histogram of the intensity distribution from the ZnO (black circles) and opal photonic crystal (red rectangles). The dashed gray line and the solid red line show the Rayleigh statistics and the bottom panel shows the residual; deviation of each distribution from the Rayleigh statistics.

the photonic crystal with the ZnO layer, we plot the histogram of the intensity distribution obtained from the photonic crystal sample. A Rayleigh distribution with mean value $< I >= 121.9$, obtained from the intensity histogram, is fitted to the data. In the low intensity limit below 500 counts, the distribution follows the Rayleigh statistics, manifesting the random intensity distribution of the low intensity light originating from the randomness in the crystal. At higher intensity above 500 counts, a striking deviation from the Rayleigh distribution is observed. The relative residuals in the bottom panel of Fig. 6.5 show the deviations from the Rayleigh distributions more clearly. The goodness of fit for the ZnO sample is χ^2=0.51 showing a very good agreement with the Rayleigh statistics and for the opal crystal is χ^2=6.4 indicating a huge deviation from the Rayleigh distribution. These observations confirm that the high intensity spots observed in the reflected light (see Fig. 6.4) originate from the periodicity in the crystal E_b as they do not match the random distribution. For an ideal photonic crystal without imperfection, multiple intense peaks from different Bragg planes are expected that do not necessarily follow the Rayleigh statistics.

6.4 Intensity correlations in presence of long-range order

The deviations from Rayleigh statistics are a clear sign of correlations in the intensity distribution of the photonic crystal sample. To quantify these correlations we have studied the auto-correlation of the scattered light from both random scattering sample and the opal photonic crystal. The auto-correlation $[I \star I]$ of the camera image of the reflected light with itself is given by:

$$[I \star I](\Delta x, \Delta y) \equiv \int_{-\infty}^{\infty} \int_{-\infty}^{\infty} dxdy\; I(x,y)I(x+\Delta x, y+\Delta y) \tag{6.5}$$

where $I(x, y)$ is the measured reflected intensity, and x and y are the spatial coordinates.

Fig. 6.6 (a) and (b) show the auto-correlation plots of the images taken at two different positions on the sample separated by two lattice constants $\Delta x = 2a$ where we clearly see a hexagonal pattern with a periodicity that matches with the crystal periodicity. The two images are very similar except that one is slightly rotated with respect to the other one. This might be due to the fact that the translation is not along the crystal axis and therefore after translating 2 lattice constants we do not arrive at a similar position as before translation. In these two plots contribution of E_B is clearly seen, resulting in a periodic wave structure. In Fig. 6.6 (c) the auto-correlation averaged over one crystal unit-cell is presented. Here we moved the crystal 700 nm to the next unit-cell in steps of 100 nm. At every step the reflected light is recorded, the auto-correlation of each image is calculated, and eventually the auto-correlations are averaged resulting in Fig. 6.6 (c) in which the periodicity is partially averaged out. This is because due to complicated profile of the fields in 3D crystals, at every position in the unit-cell different Bloch modes can couple and propagate inside the crystals. However, these Bloch modes at different positions are still correlated, resulting in a different periodicity in the averaged auto-correlation.

Figure 6.6 (d) shows the auto-correlation of the ZnO speckle pattern. The speckle pattern is recorded when the ZnO sample is placed in the setup with the same configuration and is illuminated with the laser light. The auto-correlation looks very different from the auto-correlation obtained from the photonic crystal sample. The decorrelation here is much slower than for the photonic crystal sample. This is because the speckle pattern from the ZnO sample is much wider than the scattered light from the photonic crystal. The bright peak in the middle is also present here. The width of the bright peak in the middle is the same for both crystals and the ZnO sample and is set by the smallest feature that can be resolved with the setup and therefore it is a diffraction limited spot. As the light transport in the ZnO sample takes place with random multiple scattering, no periodic correlation is seen.

6.5 Response of photonic crystals to a shaped wavefront

In order to probe both the surface and the depth inside the crystal we have used two different approaches. In the first approach we send a Gaussian beam focused on the crystal surface and measure the crystal response to this wavefront as presented in the previous sections. Here the Gaussian beam can be represented as many different plane waves,as modes in free space, with different wave vectors that are sent to the photonic crystal. In the second approach we use wavefront shaping. Wavefront shaping is a technique pioneered in our group [35, 36], that is capable of controlling waves in space and time for imaging and focusing in complex media such as random scattering materials. Using feedback algorithms the illumination wavefront is optimized such that the scattered light is focused

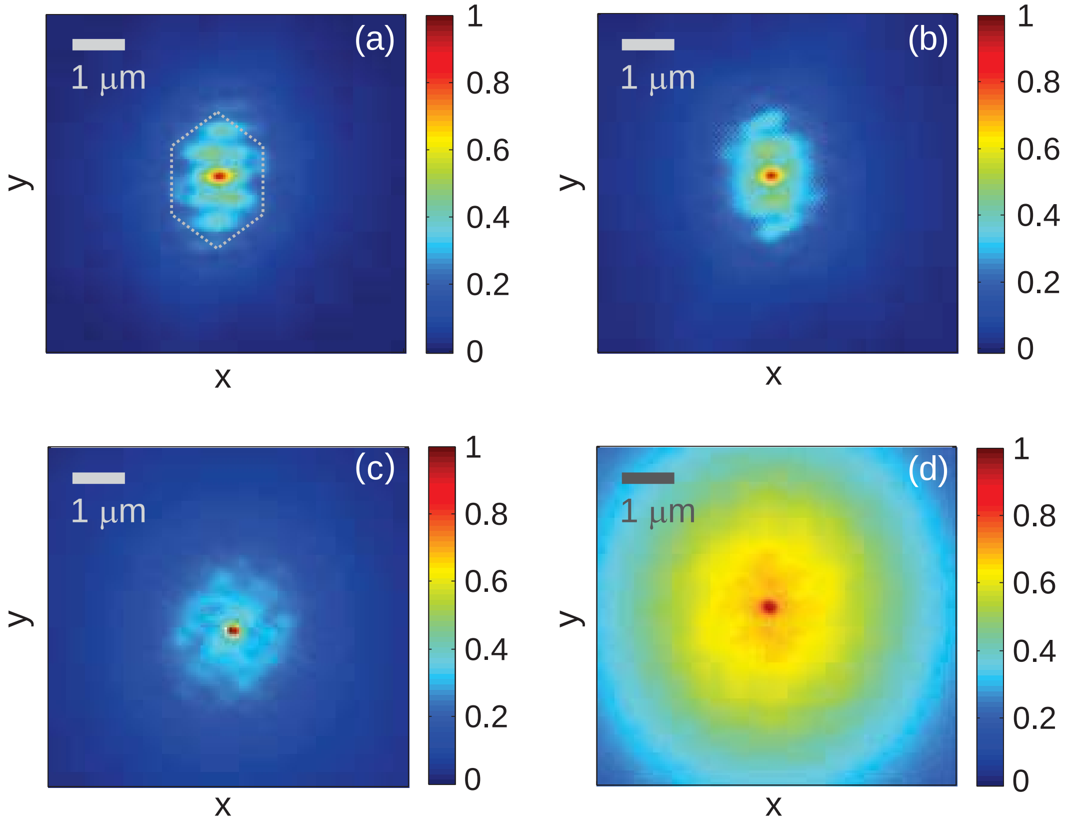

Figure 6.6: The auto-correlated image of the scattered light from the opal photonic crystal and the ZnO layer. (a) and (b) auto-correlations at two different positions on the opal that are 2 lattice constants apart from each other. (c) The averaged auto-correlation over one crystal unit-cell.(d) Auto-correlation of speckle pattern from the multiple scattering ZnO sample.

after passing through the sample or even when reflecting back from the sample. This method is very flexible in sending a desired wavefront into the crystal. The wavefront is modulated using a spatial light modulator (SLM). The main difference between the two approaches is that in the first approach the wave front has a smooth phase, while in the second approach the wavefront has random phase. The details of each approach are discussed below including advantages and disadvantages of each method.

6.5.1 Focusing light on the surface

To study the light propagation at different positions in the sample we translate the sample in the xy plane perpendicular to the optical axis, while everything else is fixed. We record one camera image per translation step. Figure 6.7 blue dashed line shows the result of maximum intensity (at every translation step) as a function of translation when we send a Gaussian beam to the sample. The maximum intensity of the camera image shows periodicity that matches with the lattice periodicity. This indicates that the wave structure repeats itself after translating over one period. Here we eliminate the direct surface reflection

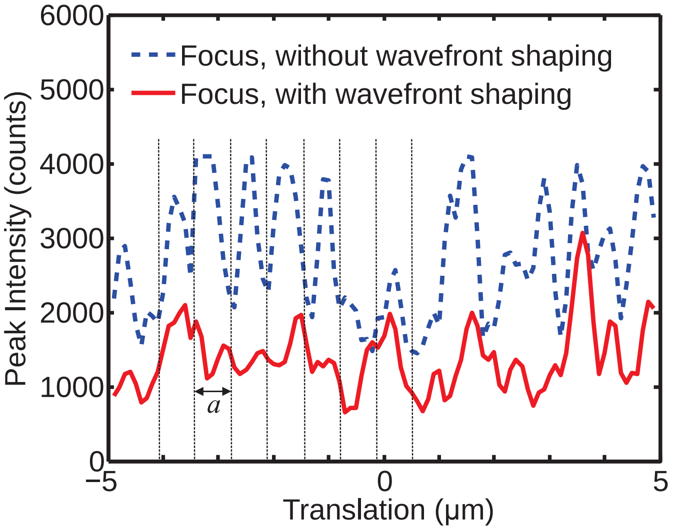

Figure 6.7: The maximum peak intensity of the focus on the sample versus the translation. The translation is over a distance of 10 μm with steps of 100 nm. The blue dashed line is the the maximum focus intensity without wavefront shaping. The unit-cell modulation of the intensity is clearly seen. The red curve is the maximum intensity of the wavefront shaped focus, showing less periodicity.

and single scattering events by using a cross polarization detection to filter the polarization maintained lights. Therefore the recorded intensity is a combination of E_{B} the light that is reflected from the periodic structure and E_{d} the scattered light by the randomness. Thus in Fig. 6.7 the observed periodicity is assigned to E_{B}, and the deviations from the periodic intensity pattern are attributed to E_{d}.

6.5.2 Wavefront shaping

We performed wavefront shaping on both opal and silicon inverse-woodpile photonic crystals. Light that is sent to the sample has the optimized wavefront to make a bright focus on a desired position on the crystal surface. The reflected light is recorded with a camera which is in the image plane of the sample surface. Wavefront shaping redistributes most of randomly scattered light to the focus, producing a new single bright focus different from the initial focus. Figure 6.8 shows the optimized focus on the crystal surface. The random scattered light around the focus are redistributed to the focus, resulting in an enhanced focus.

After light is focused on the sample surface we translate the sample in lateral direction with respect to the illumination objective. The crystal is translated over a distance of 10 μm with steps of 100 nm. Again at every step the camera records images of the sample's surface. From the position of the first optimization we first translate to the right in x direction, then the sample is moved back to its initial position, and then we translate the sample to the opposite direction. To compare the wavefront shaped illumination with the non-wavefront shaped one, we repeat the same measurements shown in Fig. 6.7 at the same position on the crystal. The red curve shows the maximum intensity of the wavefront shaped

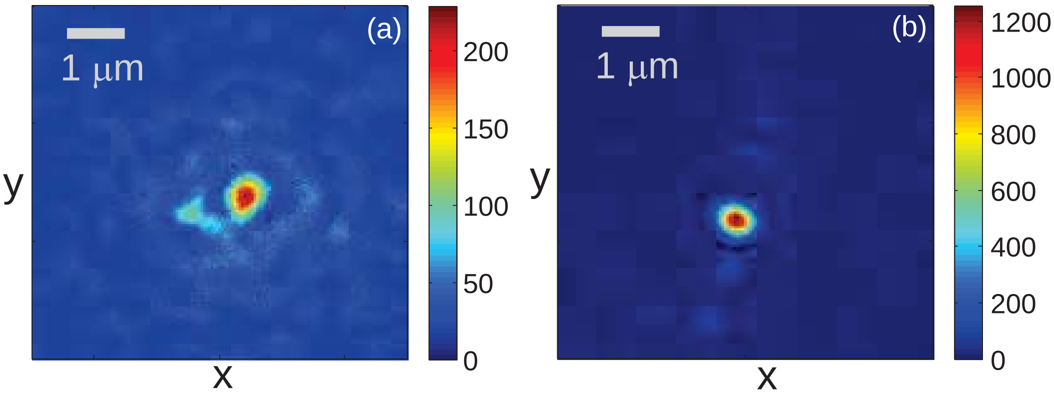

Figure 6.8: The intensity map of the scattered light from the surface of an opal photonic crystal, when (a) a plane wave is sent to the objective and is focused on the sample, and (b) a shaped wavefront is sent to the objective and an optimized focus is made on the sample surface.

focus versus translation. The observed periodicity matches well with the periodic signal from the non-wavefront shaped focus. The maximum intensity of the wavefront shaped data is more random than the non-wavefront shaped one. Since the wavefront shaping optimizes the light propagating through the maximum reflectivity channels in the sample it therefore affects the random scattered light E_d rather than the Bragg reflected light E_B. This results in increasing the effects from the randomness in the sample and thus less periodicity as seen in the figure. The wavefront shaping can be specially a more powerful method when a sample has a broad stop gap or a band gap since then the light can not propagate deep inside and probe the complex internal structure of the crystal.

Figure 6.9 shows two different wavefront shaping scans on different initial positions on the sample. The wavefront is shaped at the zero translation position, and it is kept fixed while translation. The red curve shows clear periodicity on both sides, but for the blue curve, periodicity disappears by translation on the left side. We believe that for these translations on the sample surface we have moved from one grain to a neighboring grain, where the grain has a different crystal orientation as the initial one. It is remarkable that the intensity does not quickly drop with the translation, as in a random medium.

6.6 Optical correlations in photonic crystals

In our study we develop a new method to measure how identical the wave structure inside a photonic crystal is. Our method is capable of probing deep inside the crystal and finding the structural wave correlations in photonic crystals independent of the crystal structure. We have measured the long range order of waves in both self-assembled opal photonic crystals and top-down fabricated silicon photonic crystals.

We make a 2D raster scan on the crystal surface. The raster scan is automated and is done by translating the sample in rows parallel to each other. With this

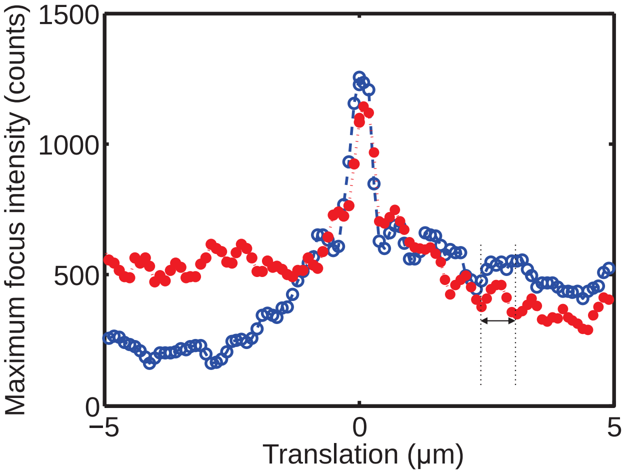

Figure 6.9: Maximum focus intensity for two different wavefront shaping realizations on different positions on the opal crystal. The red curve shows periodicity on both sides, confirming the similarity in the crystal structure over a distance of 10 μm. The periodicity is indicated with a double sided arrow. The blue curve shows periodicity only in one side and a drop in the intensity on the other side. This is probably because on the left side the focus has moved to a different grain.

scan we cover an area of 16 by 16 μm with translating the sample in steps of 100 nm and recording one camera image at every step. Such a scan including recording the camera images takes about 48 hours. In order to have a stable alignment the sample was mounted in the setup 6 hour prior to the measurements and a stability check was performed by measuring the speckle auto-correlations in time. The intensity fluctuations of laser source is measured to be only 0.4%.

After the data are collected, we choose one camera image of the reflected light taken at an arbitrary position (n, m) on the sample surface $I_{n,m}$ and cross correlate all other images $I'_{n',m'}$ with this image. The cross correlation function is written as follows:

$$[I_{n,m} \star I'_{n',m'}](\Delta x, \Delta y) \equiv \int_{-\infty}^{\infty} \int_{-\infty}^{\infty} dxdy \; I^*_{n,m}(x, y) I'_{n',m'}(x + \Delta x, y + \Delta y) \quad (6.6)$$

This enables us to make a map of cross correlation over the entire translation area. Figure 6.10 shows the cross-correlation maps for both the opal and the 2D silicon crystal. Depending on the initial image for the cross correlations we get different cross correlation maps. Light reflected at positions of higher correlations are more similar to each other than the light reflected from positions of lower correlations.

Figure 6.10 (a) shows the cross correlation for the opal photonic crystal. An overall view on the figure shows periodicity of a=0.6 μm that matches the crystal periodicity. In the middle of the scan an island of high correlation, more that 0.9, is seen. The island is extending in x direction from x=-8 to x=6 μm and in y direction it is confined between y=-4 μm to y=2 μm. This shows that within one grain the wave structure is more similar than the neighboring grain separated

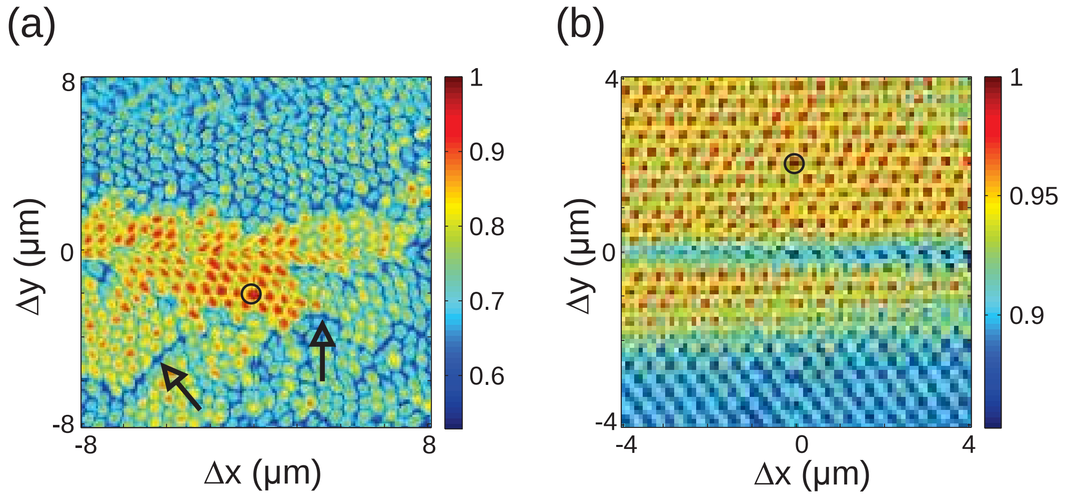

Figure 6.10: Cross correlation of the camera images of the reflected light from the opal and the silicon photonic crystal when illuminating the samples with laser light. (a) Cross correlation of opal photonic crystal over an area of 16 μm by 16 μm. Individual particles are seen in the image that look like small spheres with diameter of about 0.6 μm. In the middle of the image an area of high correlation is seen indicating one grain in the opal crystal. The dark blue lines between particles correspond to the grain boundaries in the opal (indicated by black arrows). (b) Cross correlation of silicon photonic crystal over an area of 8 μm by 8 μm. Periodicity is seen in the entire range which matches with the crystal periodicity at both directions. The black circles indicate the starting points of the cross correlations (n,m).

with grain boundaries. The crystal grain boundaries are observable in dark blue *e.g.*, as indicated with black arrows. Fig. 6.10 (b) shows the cross correlation for the 2D silicon crystal. The map shows periodicity in the entire image. For this crystal depending on the scan direction the periodicity is different. From the SEM images the two lattice constants are calculated to be $a = 693 \pm 10$ and $c = 488 \pm 11$ nm and our observations here matches with the crystals' parameters. At some part in the image the correlation is lower than the other parts. This might be due to some drift in the setup during the long scan, or the sample surface has a small curvature resulting in an out of focus of the sample. Since the correlation scan is done symmetrically with respect to the y=0 line, an instability can not cause an asymmetric correlation, we therefore attribute the low correlation region to the samples' surface.

To compare the correlation from the two different samples we look at one line profile of the cross correlation. For reference we repeat our experiment on a random ZnO layer and plot the cross correlation as a function of translation. Figure 6.11 shows the one line cross correlation for the silicon photonic crystal, the opal crystal and the random scattering layer of ZnO. The reference ZnO decorrelates to a level of about 0.2, and no periodicity is seen, as expected for random media. The 0.2 level is still a high correlation for ZnO compared to the correlation of less than 0.1 in the transmission configuration. Since the ZnO layer has a glass substrate we think that the reflection from the substrate increases

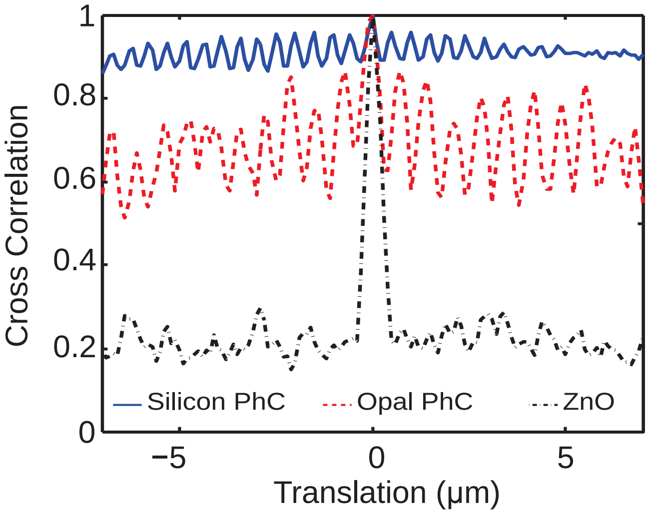

Figure 6.11: One line profile of the cross correlation of the reflected light shown in Fig. 6.10 for opal and silicon crystals, and random scattering sample of ZnO. For both crystals periodicity is seen which matches with the crystal periodicity. The decorrelation in the silicon photonic crystal is only about 0.14, indicating a very good crystal quality. For the opal crystal correlation is to a minimum of around 0.6, which shows contribution of more disorder compared to the silicon crystal. For reference cross correlation of random scattering sample of *ZnO* is presented, showing a decorrelation of about 0.8.

the correlation. For the opal crystal the correlation level is as high as 0.6, and periodicity is seen over the entire range of the translation. This higher level of correlation compare to the random ZnO layer is due to contribution of the periodicity E_{B}. Remarkable results are obtained from silicon photonic crystals. The silicon crystal shows clear periodicity on top of an even higher correlation level of 0.9. This high correlation level is obtained by the major contribution of E_{B}. The single crystalline structure and the extreme control of disorder in top-down fabrication method of the silicon photonic crystal results in an nearly perfect crystal structure.

The lower correlation in opal compared to the silicon crystal is expected due to multiple grain crystalline structure of the opal and size polydispersity of the nano-particles used in the synthesize which yield a grater contribution of E_{d} in the opal crystal. Since the field due to disorder E_{d} is random with respect to position it does not contribute to the correlations in the structure, therefore the more disorder in the structure leads to a higher E_{d} and a lower correlation. Since the focus size is in the order of one crystal unit cell or smaller, we believe that in this experiment we probe both the long range and the short range correlations. In the next section we quantitatively distinguish the decorrelation due to the short range and long range order.

In the correlation map we usually have a high correlation peak in the middle then there is a tail with a slight decorrelation over a long translation range on top of a relatively constant correlation level. In order to have a measure for the correlation in the photonic crystal we define a correlation length, which is

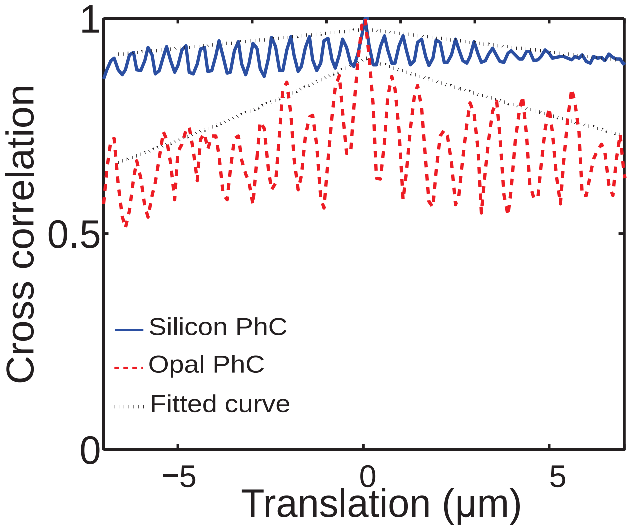

Figure 6.12: One line cross correlation for both opal(red dashed line) and silicon (blue solid line) photonic crystal, and the fitting curves. The opal photonic crystal shows a faster decorrelation, indicating a shorter correlation length.

the length where the correlation decreases to $1/e$ of the maximum cross correlation [37]. To obtain the correlation length we exclude the central peak and fit the tail with an exponential model. For the fitting only the maxima of the cross correlations has been taken into account. Figure 6.12 shows the fitted curve together with the cross correlation curve. The model has two free parameters namely the correlation length and the overall correlation. By averaging the correlation lengths obtained from several fits at different cross sections, we obtain a correlation length of $l_{cor} = 26 \pm 1.7\ \mu m$ for the opal and $l_{\rm cor} = 95 \pm 3\ \mu m$ for the silicon photonic crystal. The reason that the $l_{\rm cor}$ for the opal crystal is longer than the averaged grain size of the opal is that grains have the same directionality and therefore they are correlated. For the 2D silicon crystal due to single crystal structure we expect a longer $l_{\rm cor}$. The reason for observing a shorter $l_{\rm cor}$ can be due to the short scan range in our measurement, much shorter than the $l_{\rm cor}$, that causes an uncertainty in calculating the $l_{\rm cor}$. From this we conclude that the silicon photonic crystal has about 4 times less disorder than the synthesized opal photonic crystal. This disorder includes both size polydispersity and position variation.

6.6.1 Long range correlation in opal photonic crystals

Most opal crystals exist in polycrystalline form rather than as a single crystal. They are composed of hundreds of grains (small crystals) packed together to fill all space. Each individual grain has a different orientation than its neighbors. Although long-range order exists within one grain, at the boundary between grains, the ordering may change direction. For the opal crystals grown on silicon, the SEM images show that the long range order is mostly maintained since different grains have the same directions. In order to measure the long range correlation in photonic crystals we place the sample out of the objectives' focus so that the incident light on the sample covers an area with a diameter of 3 μm. We then translate the sample, record images at every step, and perform the cross correlation analysis. The large focus probes a larger area in the sample and therefore is less sensitive to the short range order in the sample. The cross correlation of the scattered light from the out of focus sample is plotted together with the in-focus sample in figure 6.13. Interestingly the cross correlation peak broadens but the correlation level indicated by B drops only by 0.05. This suggests that this correlation level is due to the long range order in the crystal and as expected is not sensitive to the focus size.

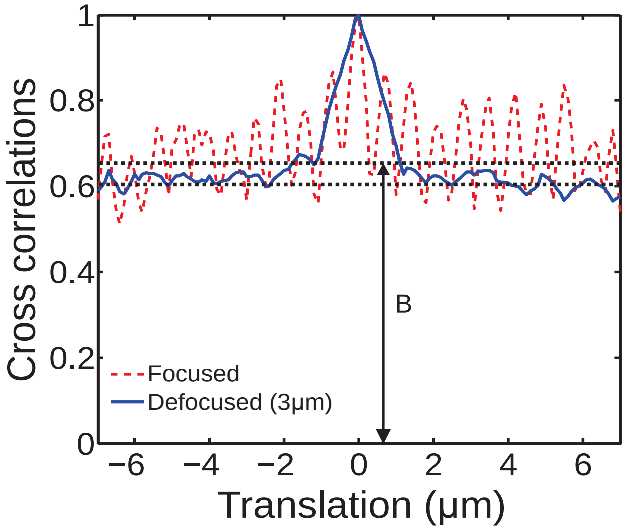

Figure 6.13: Cross correlation of the reflected light over one line translation for in focus (red dashed line) and out of focus opal sample (blue solid line). The correlation is on top of correlation background B, and does not depend on the focus size.

From these measurements we conclude that the high correlation level of the silicon photonic crystal is due to the long range order as it is expected due to monocrystalline form of the top-down crystals. For the opal crystals the long range order is reduced due to slight changes in the crystal directions in different grains. For both crystals the deviation of the cross correlation from one, is the result of random scattering E_{d}.

6.7 Summary and conclusion

In this chapter we studied the light transport inside real photonic crystals. A real photonic crystal is of finite extent and therefore has interfaces with free space. Since only Bloch waves can propagate inside a photonic crystal the illuminated wave front to the crystal couple to the Bloch modes. Due to the photonic crystal surface impedance the external wavefront can not couple to all available Bloch modes. After the light is partially coupled to the crystal it propagates inside the crystal with two different processes: the Bloch propagation due to perfectly periodic crystal, and randomly scattered light due to disorder. Our remarkable results about probing the photonic crystal structure with correlation microscopy method, show the interplay between random scattering E_{d} and the Bloch propagation E_{B}. We have studied the histogram of intensity distribution of the reflected light from photonic crystals, which shows clear deviations from the Rayleigh distribution expected for random scattering matterials. Until now intensity statistics have not been reported for photonic crystals. To the best of our knowledge our study here is the first study of intensity distribution from ordered photonic structures. From the auto-correlation of the reflected intensity we have observed the contribution of E_{B} giving rise to a periodic pattern in the auto-correlation with a period that matches the crystal unit-cell length. We have illuminated the crystals with a wavefront shaped light, and we observed more contribution from the crystal disorder. The auto-correlations of the reflected light from both opal and silicon crystals yield in a high correlation level with a periodic correlations. The periodicity and the high correlation level are attributed to the E_{B} and the small decorrelation from 1, which is expect for a perfect crystal is caused by E_{d}. The results are very complex due to the fact that photonic crytals are a combination of both order and disorder structures. We believe that our results are a major step in understanding the light transport in real photonic crystals.

Bibliography

[1] J. D. Joannopoulos, S. G. Johnson, J. N. Winn, and R. D. Meade, *Photonic crystals - molding the flow of light, 2nd edition* (Princeton University Press, 2008). — p.89.

[2] M. Notomi, *Theory of light propagation in strongly modulated photonic crystals: Refractionlike behavior in the vicinity of the photonic band gap*, Phys. Rev. B **62**, 10696 (2000). — p.89.

[3] M. Doosje, B. J. Hoenders, and J. Knoester, *Scattering of light on the surfaces of photonic crystals*, Opt. Commun. **206**, 253 (2002). — p.89.

[4] S. Fan, P. R. Villeneuve, and J. D. Joannopoulos, *Theoretical investigation of fabrication-related disorder on the properties of photonic crystals*, J.Appl. Phys. **78**, 1415 (1995). — p.89.

[5] A. F. Koenderink, A. Lagendijk, and W. L. Vos, *Optical extinction due to intrinsic structural variations of photonic crystals*, Phys. Rev. B **72**, 153102 (2005). — p.89, 91.

[6] J. J. Wierer, A. David, and M. M. Megens, *III-nitride photonic-crystal light-emitting diodes with high extraction efficiency*, Nature Photon. **3**, 163 (2009). — p.89.

[7] M. Loncar, T. Yoshie, A. Scherer, P. Gogna, and Y. Qiu, *Low-threshold photonic crystal laser*, Appl. Phys. Lett. **81**, 2680 (2002). — p.89.

[8] S. Hughes, L. Ramunno, J. F. Young, and J. E. Sipe, *Extrinsic optical scattering loss in photonic crystal waveguides: role of fabrication disorder and photon group velocity*, Phys. Rev. Lett. **94**, 033903 (2005). — p.89.

[9] J. V. Sanders, *Colour of precious opal*, Nature **204**, 1151 (1964). — p.89.

[10] H. Mıguez, C. Lopez, F. Meseguer, A. Blanco, L. Vázquez, R. Mayoral, M. Ocana, V. Fornés, and A. Mifsud, *Photonic crystal properties of packed submicrometric SiO2 spheres*, Appl. Phys. Lett. **71**, 1148 (1997). — p.89.

[11] K. Lin, J. C. Crocker, V. Prasad, A. Schofield, D. A. Weitz, T. C. Lubensky, and A. G. Yodh, *Entropically driven colloidal crystallization on patterned surfaces*, Phys. Rev. Lett. **85**, 1770 (2000). — p.89.

[12] O. D. Velev, A. M. Lenhoff, and E. W. Kaler, *A class of microstructured particles through colloidal crystallization*, Science **287**, 2240 (2000). — p.89.

[13] G. A. Ozin and S. M. Yang, *The race for the photonic chip: colloidal crystal assembly in silicon wafers*, Adv. Func. Mater. **11**, 95 (2001). — p.89.

[14] P. Yang, T. Deng, D. Zhao, P. Feng, D. Pine, B. F. Chmelka, G. M. Whitesides, and G. D. Stucky, *Hierarchically ordered oxides*, Science **282**, 2244 (1998). — p.89.

[15] K. M. Ho, C. T. Chan, C. M. Soukoulis, R. Biswas, and M. Sigalas, *Photonic band gaps in three dimensions: new layer-by-layer periodic structures*, Solid State Commun. **89**, 413 (1994). — p.89.

[16] J. G. Fleming and S. Y. Lin, *Three-dimensional photonic crystal with a stop band from 1.35 to 1.95 µm*, Opt. Lett. **24**, 49 (1999). — p.89.

[17] S. Noda, K. Tomoda, N. Yamamoto, and A. Chutinan, *Full three-dimensional photonic bandgap crystals at near-infrared wavelengths*, Science **289**, 604 (2000). — p.89.

[18] M. Qi, E. Lidorikis, P. T. Rakich, S. G. Johnson, J. D. Joannopoulos, E. P. Ippen, and H. I. Smith, *A three-dimensional optical photonic crystal with designed point defects*, Nature **429**, 538 (2004). — p.89.

[19] J. Schilling, J. White, A. Scherer, G. Stupian, R. Hillebrand, and U. Gösele, *Three-dimensional macroporous silicon photonic crystal with large photonic band gap*, Appl. Phys. Lett. **86**, 011101 (2005). — p.89.

[20] M. Hermatschweiler, A. Ledermann, G. A. Ozin, M. Wegener, and G. von Freymann, *Fabrication of silicon inverse woodpile photonic crystals*, Adv. Func. Mater. **17**, 2273 (2007). — p.89.

[21] L. A. Woldering, *Fabrication of photonic crystals and nanocavities*, PhD Thesis, University of Twente, 2008. — p.89, 93.

[22] A. Tandaechanurat, S. Ishida, K. Aoki, D. Guimard, M. Nomura, S. Iwamoto, and Y. Arakawa, *Demonstration of high-q (>8600) three-dimensional photonic crystal nanocavity embedding quantum dots.*, Appl. Phys. Lett. **94**, 171115 (2009). — p.89.

[23] D. J. Shir, E. C. Nelson, D. Chanda, A. Brzezinski, P. V. Braun, J. A. Rogers, and P. Wiltzius, *Dual exposure, two-photon, conformal phase mask lithography for three dimensional silicon inverse woodpile photonic crystals*, J. Vac. Sci. Technol. B **28**, 783 (2010). — p.89.

[24] A. A. Chabanov, Y. Jun, and D. J. Norris, *Avoiding cracks in self-assembled photonic band-gap crystals*, Appl. Phys. Lett. **84**, 3573 (2004). — p.90.

[25] E. P. Wigner, *Mathematical proceedings of the cambridge philosophical society*, **47**, 790 (1951). — p.90.

[26] C. W. J. Beenakker, *Random-matrix theory of quantum transport*, Rev. Mod.

Phys **69**, 731 (1997). — p.91.

[27] S. F. Liew, S. M. Popoff, A. P. Mosk, W. L. Vos, and H. Cao, *Transmission channels for light in absorbing random media: from diffusive to ballistic-like transport*, Phys. Rev. B **89**, 224202 (2014). — p.91.

[28] I. M. Vellekoop, *Controlling the propagation of light in disordered scattering media*, PhD Thesis, University of Twente, 2008. — p.91, 92, 93.

[29] P. N. den Outer, *Multiple light scattering in random discrete media*, PhD Thesis, University van Amsterdam, 1995. — p.92.

[30] S. P. Morgan and I. M. Stockford, *Surface-reflection elimination in polarization imaging of superficial tissue*, Opt. Lett. **28**, 114 (2003). — p.92.

[31] A. Hartsuiker and W. Vos, *Structural properties of opals grown with vertical controlled drying*, Langmuir **24**, 4670 (2008). — p.93.

[32] A. Hartsuiker, *Ultrafast all-optical switching and optical properties of microcavities and photonic crystals*, PhD Thesis, University of Twente, 2009. — p.93.

[33] L. A. Woldering, R. W. Tjerkstra, H. V. Jansen, I. D. Setija, and W. L. Vos, *Periodic arrays of deep nanopores made in silicon with reactive ion etching and deep UV lithography*, Nanotechnology **19**, 145304 (2008). — p.93.

[34] J. W. Goodman, *Statistical optics* (John Wiley, Newyork, 2000). — p.94.

[35] I. M. Vellekoop and A. P. Mosk, *Focusing coherent light through opaque strongly scattering media*, Opt. Lett. **32**, 2309 (2007). — p.96.

[36] A. P. Mosk, A. Lagendijk, G. Lerosey, and M. Fink, *Controlling waves in space and time for imaging and focusing in complex media*, Nature Photon. **6**, 283 (2012). — p.96.

[37] B. E. Warren, *X-ray diffraction* (Courier Dover Publications, 1969). — p.103.

CHAPTER 7

Light transport in silicon two-dimensional photonic crystals

7.1 Introduction

A periodic structure of materials with differing indices of refraction on the order of the wavelength is called a photonic crystal. These photonic crystals strongly affect the dispersion relation of light due to interference effects resulting from Bragg diffraction inside the crystal [1]. As a consequence, certain light frequencies are forbidden to propagate inside the crystal, resulting in a stopgap for these light frequencies. For all three spatial dimensions the latter is referred to as a photonic band gap [2]. A photonic structure which exhibits a band gap for light is relevant for various applications as for instance to trap light or to control the rate of spontaneous emission of light sources [3, 4], resulting in a broad spectrum of possible applications. The interaction of light with periodic lattice of the photonic crystals gives rise to distinct optical phenomena as for instance an enhanced optical reflectivity in the stopgaps [5–8]; frequency range where the incident light decays exponentially inside the crystal due to the Bragg diffraction.

In practice photonic crystals tend to suffer from unavoidable imperfections like size polydispersity and position variation [9–11]. A perfect photonic crystal has an infinitely large transport mean free path; the distance which light travels before losing its coherence. However, a real photonic crystal has always imperfections and therefore a finite transport mean free path. Therefore measuring the extinction length and transport mean free path indicates how much imperfection a crystal has. A convenient method to measure the extinction length and mean free path was developed by Johnson *et al* [12] who determined the mean free path by measuring the out-of-plane scattering. A similar configuration is used by Avoine *et al* [13], who characterized photonic crystal cavity modes. Here we use the out-of-plane scattering technique to determine the extinction length in a photonic crystal. Besides the scattering of light due to imperfections, yet another important difference between a strong scattering material and a photonic crystal needs to be taken into account, wherein the stop gap light decays exponentially due to the Bragg diffraction.

In this chapter we investigate the mean free path of two dimensional silicon photonic crystal by means of out-of-plane scattering within a broad frequency range covering both inside and outside the stop gaps. We compare the results from the photonic crystal with a multiple scattering sample of Teflon polymer to characterize the extinction length and the Bragg length of the crystal.

7.2 Theory

In a collection of scatterers the scattering mean free path (l_{sc}) is the average distance between two consecutive scattering events. The intensity of the incident beam decays exponentially within the scattering material with a decay according to the extinction length (l_{ex}), which is determined by the scattering mean free path and the absorption length (l_{ab}) as $l_{ex}^{-1} = l_{sc}^{-1} + l_{ab}^{-1}$ [14].

$$I(x) = I_0 e^{-\frac{x}{l_{ex}}}, \tag{7.1}$$

where $I(x)$ is the intensity along the traveled path of light and I_0 is the incident intensity. If a sample is thinner than one mean free path this coherent, unscattered beam has an exponentially large contribution in the detected intensity, and the Beer-Lambert-Bouguer law determines the extinction length.

When the sample is thicker than one mean free path $d > l_{sc}$ the scattering exhibits a preferred scattering angle, which is described with the scattering function. Depending on the scattering function the direction of light will be random after one or more l_{sc}. The distance at which the intensity distribution becomes isotropic due to scattering is given by the transport mean free path l_{tr}. When $l_{sc} \leq l_{tr} << d$ the diffuse light becomes detectable. The diffuse light is well described by the diffusion equation [15]

$$\frac{\partial W}{\partial t} - D\nabla^2 W = S, \tag{7.2}$$

where W is the energy density of light, D is the diffusion constant indicating the speed at which light diffusely spreads out and S is the function describing the source of diffuse light. Therefore if the sample is thicker than the mean free path, a combination of both coherent light and the diffuse light is detectable. In Ref. [12] a method to fully characterize diffuse transport of light is presented. There light is assumed to be tightly focused on one side of a diffuse material. On another surface out-of-plane scattered light is measured parallel and perpendicular to the direction of the incident light.

Since the feature size in a photonic crystal is in the range of wavelength of probe light, it is reasonable to assume that light scattering in a photonic crystal is anisotropic. Herein a second assumption is that the scatterers are randomly distributed. For light frequencies outside the stopgap frequencies, normal scattering of light is expected. For light frequencies within the stopgap, diffusion theory breaks down since these frequencies of light are not expected to propagate inside the crystal. Therefore, light with these frequencies will not penetrate

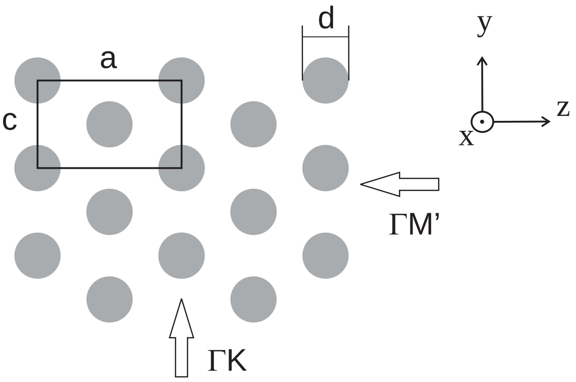

Figure 7.1: Schematic representation of the top view of the periodic nanostructure. The indicated centered rectangular lattice is characterized by lengths of $a = 693 \pm 10$ and $c = 488 \pm 11$ nm respectively. The diameter of the pores is $d = 310 \pm 10$ nm. Access to both the ΓK and the $\Gamma M'$ direction is ensured by cleaving the crystal parallel to the sides of the rectangular Bravais lattice.

far into the sample, or propagates in oblique allowed directions [16]. We perform experiments in order to describe the propagation of different randomly scattered light in a photonic crystal in a qualitative manner.

7.3 Sample selection

The out-of-plane scattering experiments are performed on two types of samples. Firstly the out-of-plane scattering of light is investigated on a two-dimensional photonic crystal. The 2D photonic crystal is etched in the corner of a piece of silicon wafer which exhibits a length and width of approximately 10 mm and 5 mm respectively and a thickness of 260 μm.

In Fig.7.1 a schematic representation is depicted of the top view of the two-dimensional photonic crystal. The figure outlines the centered rectangular lattice of the crystal. The lattice parameters for the used photonic crystal are $a = 693 \pm 10$ and $c = 488 \pm 11$ nm respectively. The photonic structure is characterized by a pore diameter of $d = 310 \pm 16$ nm and a pore depth of 5806 ± 170 nm. For characterization of the specified two-dimensional photonic crystal by means of reflectivity measurements, the selected crystal was cleaved along two different high symmetry directions along the crystal lattice. This enables both the ΓK and the $\Gamma M'$ direction of the photonic crystal to be accessible for out-of-plane scattering experiments. In the out-of-plane scattering experiments presented here only the $\Gamma M'$ direction of the two-dimensional photonic crystal is addressed.

The light sent to the crystal is polarized in two linear orthogonal directions. Incident light perpendicular to the air cylinders in the material is referred to transverse electric (TE) polarization. The radiation incident parallel to the etched rods is called transverse magnetic polarized (TM).

In Fig. 7.2 the measured reflectivity of the two-dimensional photonic crystal sample as function of the frequency for TE and TM-polarized light is depicted.

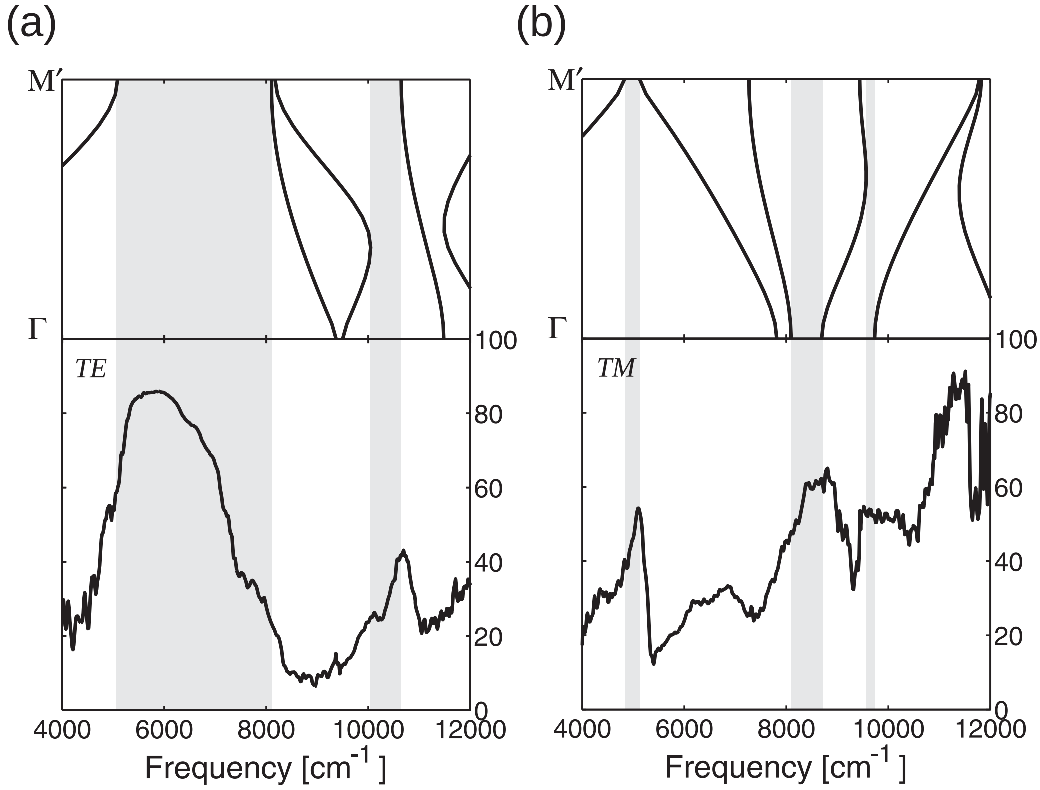

Figure 7.2: Calculated band structure and measured reflectivity of the two-dimensional photonic crystal sample (sample code Ad3c-28112008) as function of frequency for (a) TE and (b) TM polarized light incident along the $\Gamma M'$ direction of the photonic crystal [17]. The gray bars indicate the calculated stop gaps.

The data are taken from Ref. [17, 18]. The data show the reflectivity measured along the $\Gamma M'$ direction of the photonic crystal sample. For the spectral range covered in the experiments, *i.e.*, frequencies between ν=6000 and 9000 cm^{-1}, a significant variation in the reflectivity for TE and TM polarized light is observed. For TE-polarized light a reflectivity peak is present between frequencies of 5000 and 7000 cm^{-1}. A corresponding effect for an orthogonal TM-polarization is observed for light frequencies between 8000 and 8800 cm^{-1}, which are in a very good agreement with the calculated band structures.

7.4 Experimental procedure

In Fig. 7.3 a schematic representation of out-of-plane scattering is shown. Incident light illuminates the crystal from side, and in the perpendicular direction the induced scattering is collected. By measuring the intensity distribution of this out-of-plane scattered light, the extinction length is determined.

The experimental setup used during the experiments is the NIR setup described in chapter 2, where for the light source we have used a pulsed supercontinuum laser source (Fianium SC450-2) with a repetition rate 20 MHz, 2 W power over

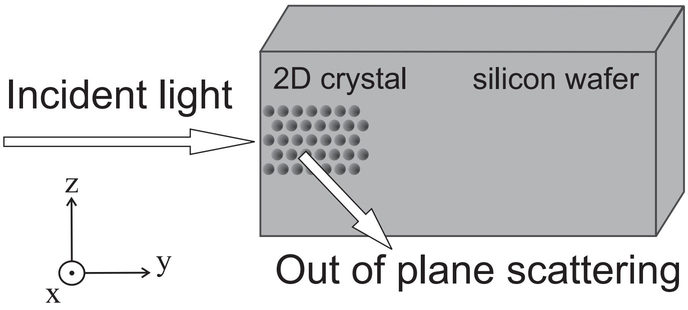

Figure 7.3: Schematic representation of a typical out-of-plane scattering scheme. Incident light illuminates the crystal from the x-z face. In the perpendicular direction the resulting out-of-plane scattering is collected.

the full spectrum. In addition to chapter 2 the light beam is sent through a reflective beam expander to increase the beam size. An aperture is placed in the expander to increase the spatial quality of the beam profile. For alignment purposes, the optical path of the supercontinuum white light source is forced to overlap with a pre-aligned Helium Neon laser (HeNe). A reflecting microscope objective with a numerical aperture (NA) of 0.28 is implemented to couple in the incident light to the sample. A Glan-Taylor Calcite polarizer (Thorlab SM05 PM5) is situated in front of the illumination objective to select linear polarization directions with respect to the orientation of the sample. Perpendicular to the illumination objective an infinity corrected microscope objective ($o1$) is situated to collect the out-of-plane scattering of the in-coupled laser light on the sample. The sample is placed in a home-built sample holder which is fixed on the sample stage. This device gives rise to a spatial scan range of several centimeters with a spatial resolution of 50 nm on the sample. Position of the sample is initialized using a hand-held controller unit (Newport, XPS-RC). The illuminating and collecting microscope objectives are aligned with respect to the sample by imaging both sides of the sample alternatively. The position of the sample is varied via a three-dimensional micro controlled translational stage. This procedures enable to address a pre-assigned location on the sample and determine the location of the excitation spot of the supercontinuum laser on the photonic crystal. The out-of-plane scattered light is sent to the grating spectrometer. This enables to resolve the scattering spectrally for light frequency ranging from 6000 to 9000 cm^{-1}. The exposure time of the spectrometer is set to collect maximum scattering without saturating the array detector. During the out-of-plane experiments the exposure time ranges typically between 2 and 10 s. As some diodes in the detector array are broken, collecting the spectra of the out-of-plane scattering inherently means that there is some spectral information lost. In the experiments the internal alignment of the spectrometer is set for the damaged diodes to correspond to a central wavelength of 1400 nm (7140 cm^{-1}).

As our photonic crystal exhibits stop gaps in the covered spectral range (see Fig. 7.2), this enables to compare the spectral dynamics of incident light for different regimes: outside and inside the stopgaps. For reference as well as for

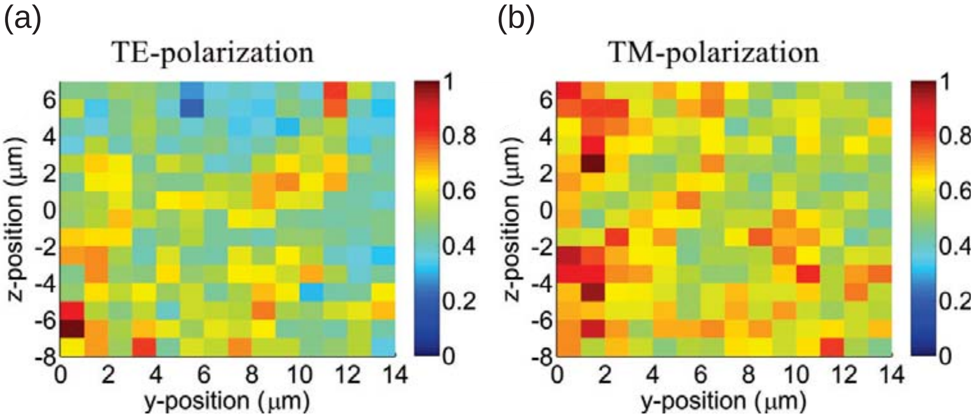

Figure 7.4: Intensity resolved out-of-plane scattering of the Teflon sample at a mean frequency of ν=7394 cm^{-1} for (a) TE-polarization and (b) TM-polarization. The sample is illuminated at coordinates y=0 and z=0, and the incident light is propagating parallel to the y-direction. The intensity is normalized to the maximum observed intensity in the operated scan range. Here the blue color represents minimum and the red shade stands for the maximum intensity.

comparison of experimental outcomes of out-of-plane scattering experiments on the photonic crystal, the out-of-plane scattering of light is studied on a solid block of Teflon. The length, width and thickness of this random scattering medium are approximately 50, 30, and 20 mm respectively.

7.5 Experimental results and discussion

For illumination along the $\Gamma M'$ direction of the photonic crystal, stop bands are expected for both transverse electric (TE) and transverse magnetic (TM) polarizations. It is expected that the presence of stopgaps strongly influence the spectrum of the induced out-of-plane scattering of the photonic crystal.

In a strongly scattering material the polarization of the incident light is of little importance since the polarization is not likely to be conserved due to multiple scattering. The dispersion relation of light in a photonic crystal, however, strongly depends on the polarization and the direction via which light is coupled to the period structure. It is expected that the mean free path will therefore also be strongly polarization and direction dependent. But when scattering occurs, the polarization of the incident light may not be conserved. In a crystal this may result in an undefined polarization with respect to a pre-selected reference frame. This can make it difficult to distinguish the influence of the polarization of the incident light on the mean free path.

7.5.1 Out-of-plane scattering on a Teflon sample

For the Teflon sample two types of experimental results are presented. By measuring the spectra over a fixed lateral extent at the out-of-plane surface of the

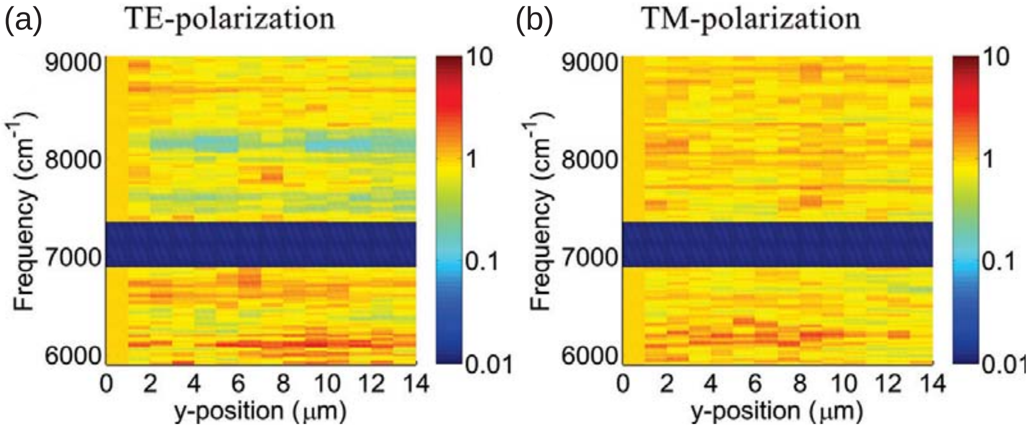

Figure 7.5: Intensity and frequency resolved out-of-plane scattering of the Teflon sample for (a) TE-polarization and (b) TM-polarization. The wide dark blue line is due to the broken diodes in the detection array, corresponding to a frequency of 6900 to 7350 cm^{-1}. The blue color represents minimum and the red shade stands for maximum intensity of the out-of-plane scattered light. For a direct comparison, the color bar is kept the same as for the measurements on photonic crystals.

sample, the spatial profile of the scattering is resolved in both intensity and frequency. Secondly, over a single line of side parallel to the propagation direction of the illumination, the intensity is monitored as function of the lateral dimension of the sample.

Fig.7.4 shows the normalized out-of-plane scattering intensity of the Teflon sample for both polarizations at a randomly chosen mean frequency of ν=7394 cm^{-1}. The illumination spot is located at y=0 and light is propagating parallel to the y-direction. The spot size in z direction is estimated to be about 25 μm. The measurements extend both 15 μm in the lateral y and z direction. Here the intensity is normalized to the maximum observed scattering intensity in the operated scan range. The optical mappings are acquired using a scan resolution of 1 μm. This quantity is optimized considering the lower limit of the spatial resolution of the collecting microscope objective. This results in an optimized duration of the experiments without loss of spatial information. In order to minimize the effects of spectral fluctuations, the data in Fig. 7.4 are averaged over a frequency interval of 50 cm^{-1}. A relative experimental error in the scattering intensity can be mostly caused by time-to-time fluctuations of the supercontinuum light source. The intensity distribution of the scattering at the probed plane shown in Fig.7.4 behaves as expected for a uniform random scattering material. The observed out-of-plane light is random, resulting in the formation of speckle: an intensity pattern formed by the interference of out-of-plane scattered waterfronts. Moreover, there are minimal observed differences between the two orthogonal polarization directions of the incident radiation, supporting the random scattering character of the Teflon sample.

In order to understand the behavior of the transport of the in-coupled light in the Teflon sample, single line intensity distributions of the out-of-plane scattered light are monitored. In figure 7.5 the intensity and frequency resolved data of the out-of-plane scattering experiment for (a) TE-polarization and (b) TM-polarization incident light over a single line at z=0 are shown. The wide dark blue lines are the broken diodes of the detection array. This precludes the out-of-plane scattering measurements between frequencies of 6900 and 7350 cm^{-1}. The data are normalized to the initial scattering intensity at the beginning of the scan. As the observed excitation spot on the Teflon sample is relatively large compared to the scanned range, corresponding data as presented in figure 7.5 are not analyzed for the direction perpendicular to the propagation direction of the incident light. This means that it is not possible to draw conclusions about the isotropic character of the sample under investigation from the data shown in Fig. 7.5. The first observation made from Fig. 7.5 (a) and (b) is the similarity between the intensity distributions of the scattering induced by the two orthogonal polarization states of the incident light. Note that some differences in the intensity are due the experimental error caused by time-to-time fluctuations of the light source. It is concluded that the sample is weakly disordered, resulting in the formation of speckle and a very long extinction length. Both polarizations scatter in the material similarly, in agreement with the expectations for a random scattering material.

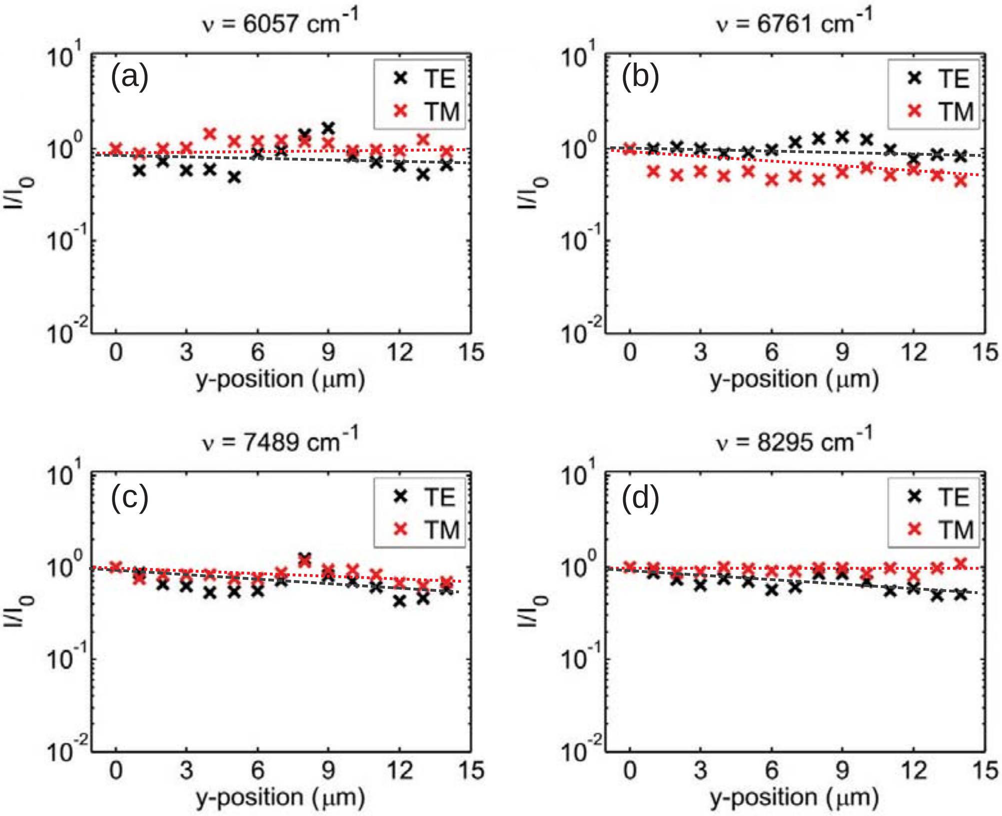

Figure 7.6: Intensity of the out-of-plane scattering of the Teflon sample as function of the lateral y-position of the collecting aperture. (a) though (d) show the intensity distribution for TE (black cross) and TM (red cross) polarized incident light at mean frequencies of ν=6057, 6761, 7489 and 8295 cm^{-1} respectively. The dashed red and black lines are guides to the eyes.

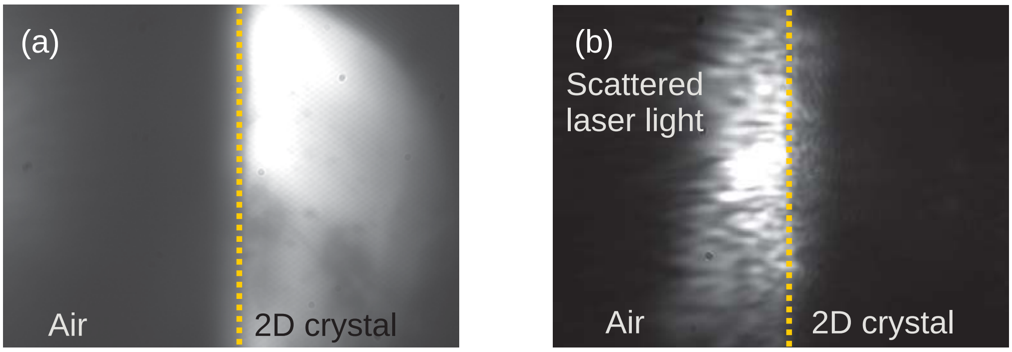

Figure 7.7: CCD image of the out-of-plane side of the 2D photonic crystal. (a) Crystal is illuminated with white LED via the detection objective, and (b) illuminated with the supercontinuum laser light via the illumination objective. Laser light is scattered from the edge of the sample and partially penetrates in the crystal. The yellow dashed line indicates the crystal-air edge.

In figure 7.6 typical intensity distributions for the out-of-plane scattered light of the Teflon sample over a single line for TE and TM polarized incident light are depicted. Fig. 7.6 (a) through (d) represent spectral cross-section of the data outlined in Fig. 7.5 for mean frequencies of ν=6057, 6761, 7489, and 8295 cm^{-1} respectively. The data are averaged over a frequency bandwidth of 50 cm^{-1}. The character of the intensity distribution of the induced scattering is in detail compared for the two orthogonal polarizations of the incident light. Again, taking into account the speckle formation, no significant differences between the frequencies of the incident radiation are perceived. Secondly, the general character of the intensity change in different frequencies of the scattering is comparable, as for both polarizations and for different frequencies no clear decay in the intensity profile is seen. Therefore it is concluded that all incident light frequencies are able to couple into the sample. Here the formation of speckle is due to multiple scattering events in the material. Over the implemented scan range the intensity of the out-of-plane scattering remains almost constant. This means that the extinction of the scattering exceeds the covered lateral scan range on the sample. The averaged extinction length for these 4 frequencies is calculated to be 42 μm, which matches with the weakly scattering character of Teflon.

7.5.2 Out-of-plane scattering of silicon two-dimensional photonic crystals

Figure 7.7 shows CCD images of a 2D photonic crystal in the setup. The images are recorded by the CCD camera situated in the detection path of the experimental setup. Fig. 7.7 (a) shows the photonic crystal when illuminating with LED via the detection objective. The bright part is the silicon crystal and the dark part is air. Fig. 7.7 (b) shows the sample in the same configuration when illuminating the sample with supercontinuum laser light via the illumination objective.

From the out-of-plane scattering on the two-dimensional photonic crystal it is observed that artifacts on the silicon surface, such as dust particles, signifi-

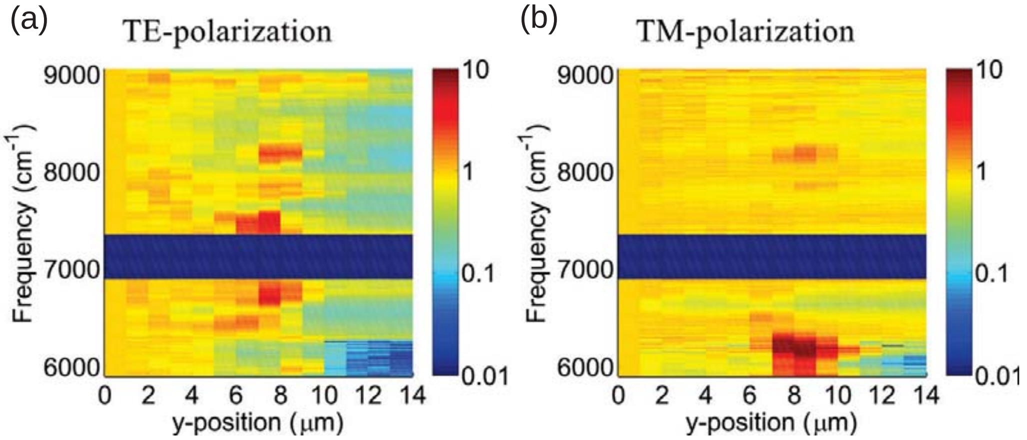

Figure 7.8: (color) Intensity and frequency resolved out-of-plane scattering of the photonic crystal for (a) TE-polarization and (b) TM-polarization light over a single line. The wide dark blue line is due to the broken diodes in the detection array, corresponding to a frequency of 6900 to 7350 cm^{-1}. The blue and red color indicate a minimum and maximum intensity respectively in logarithmic scale.

cantly contribute to the detected scattering. In order to prevent this unwanted scattering to completely conceal the desired scattering of the photonic crystal, the excitation spot of the supercontinuum laser source is positioned $\Delta x = 35\mu m$ away from the edge of the crystal.

In order to study the light transport in the photonic crystal sample the intensity distribution of the out-of-plane scattered light over a single line is monitored. For the covered spectral range, a significant change in the crystal reflectivity or the coupling of the incident laser light is expected as shown in Fig. 7.2. This is more significant for the TE-polarization in frequencies between 5000 and 7000 cm^{-1}. The corresponding effect for an orthogonal TM-polarization is expected for light frequencies between 8000 and 8800 cm^{-1}.

Figure 7.8 shows the intensity and frequency resolved out-of-plane scattering of the 2D silicon photonic crystal for (a) TE-polarization and (b) TM-polarization incident light over a single line at z=0. The data is normalized to the initial scattering intensity at the edge of the sample. In Fig. 7.8 (a) for light frequencies smaller than 6500 cm^{-1} the intensity distribution of the out-of-plane scattering along the line scan significantly decreases after 10 μm. We attribute this effect to the relatively large stop gap at a central frequency of $\nu = 6000 cm^{-1}$. A distinct increase in the intensity near a lateral position of 7 μm is observed. As the accumulation of intensity also reproduces for frequencies outside the stopgap, it is unlikely that this feature is attributed to the photonic character of the sample. Most likely the increase in scattering intensity is the result of an artifact, such as dust particle, at the surface of the photonic crystal.

Fig. 7.8 (b) shows the out-of-plane scattering for the TM polarized light. The character of the photonic crystal is more restricted in the intensity and frequency resolved measurements for light polarized along the TM-direction. Between 8000 cm^{-1} to 9000 cm^{-1} a small reduction in the intensity can be seen after a lateral

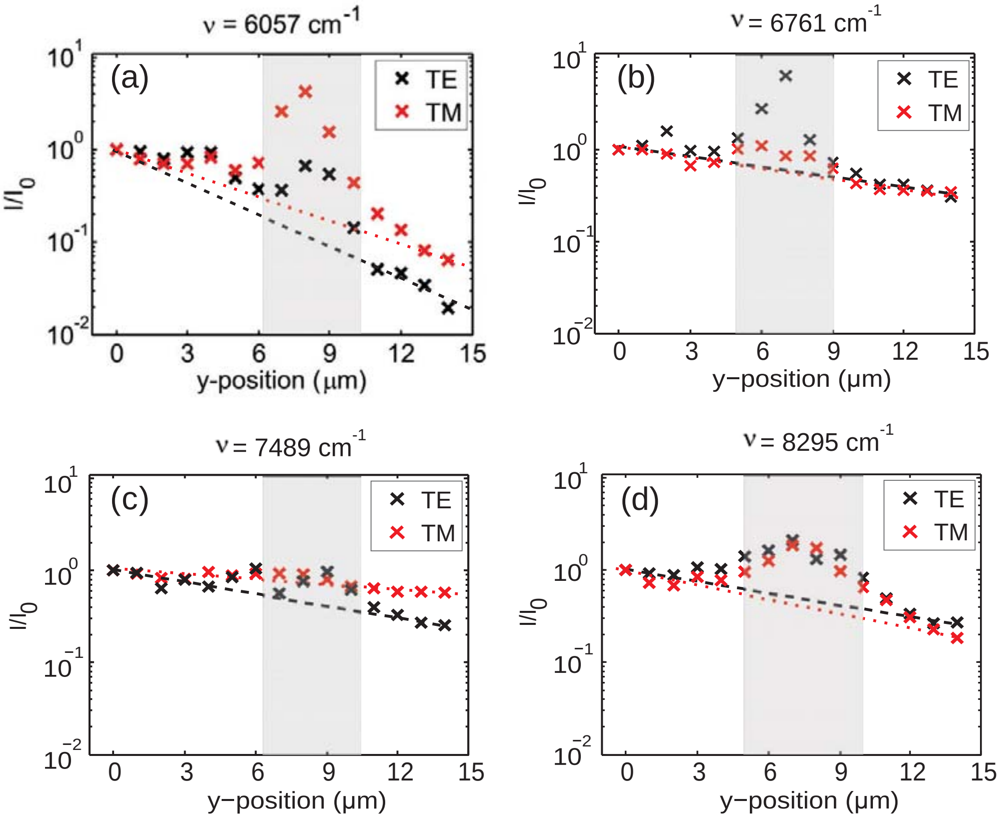

Figure 7.9: Intensity of the out-of-plane scattering of the photonic crystal as function of the lateral y-position of the collecting aperture. (a) through (d) show the intensity distribution for TE (black cross) and TM (red cross) polarized incident light at mean frequencies of ν=6057, 6761, 7489, and 8295 cm^{-1} respectively. The gray bar covers the data points which were excluded for the fitting.

position of 10 μm which can correspond to the TE stop gap. Similar to the TE polarization, for light frequencies smaller than 6500 cm^{-1} the intensity distribution of the out-of-plane scattering along the line scan significantly decreases after 10 μm. While this is not expected for the TM polarized light it can readily be understood: when scattering occurs, the polarization of the incident light is not conserved, hence the stop gap for the TE polarized light affects the TM polarized incident light, and *vice versa*.

Figure 7.9 (a) to (d) show the intensity distributions for the out-of-plane scattered light of the two-dimensional photonic crystal along a line scan for incident light polarized in the TE and TM direction for mean frequencies of ν=6057, 6761, 7489, and 8295 cm^{-1} respectively. The intensity is averaged over a frequency interval of 50 cm^{-1} and they correspond to the intensity distribution for light frequencies in, at the edge, or outside the photonic stopgap for both TE and TM polarized light. Frequency ν=6057 is in the middle of the experimental stop gap for the TE polarized light. As we expect the intensity strongly drops to almost 1% of its initial value after 15 μm. A similar drop of intensity is observed for the TE polarized light. This can be explained following our reasoning about polarization mixing in scattering. In order to extract the extinction length for

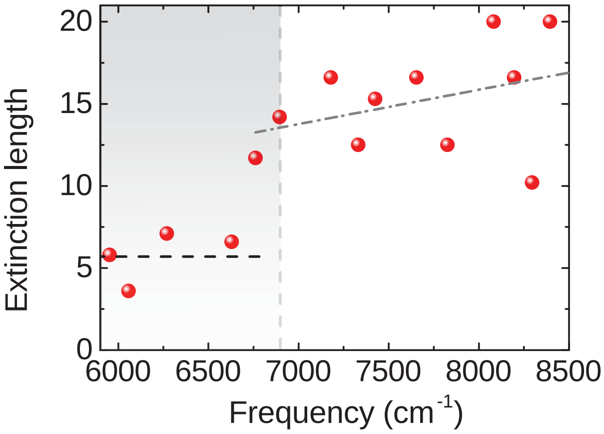

Figure 7.10: Extinction length versus as a function of frequency for TE polarized light. The gray bar indicated the experimental stop gap in TE direction. Inside the band gap the extinction length is on average 3 times smaller than outside the stop gap. Outside the stop gap the extinction length shows an increasing trend with frequency in contrast with the theoretical prediction [11].

the intensity in the crystal we fit a single exponential function to the data. For the fit we exclude the data points that are the result of an artifact at the surface (between y= 6 to y=10 μm) of the photonic crystal. We obtain an extinction length of $\ell = 3.6 \pm 0.3$ μm for TE polarized light and 5.1 ± 0.3 μm for the TM polarized light. The Bragg length for the TE stop gap is calculated to be $\ell_B = 3.3$ μm [19] which is very close to the measured extinction length. We therefore conclude that the decay is caused by the Bragg diffraction in the stop gap range. The difference between the measured extinction length and the Bragg length is expected, since the calculated and the measured stop gap do not exactly overlap as shown in Fig. 7.2. Another reason for this difference is the polarization mixing effect which leads to propagation of light with TM polarization in the TE stop gap and therefore increasing the extinction length compared to the Bragg length. At frequencies ν=6761, and ν=7489 the decrease of the intensity is very gradual as we are probing frequencies outside the stop gaps for both polarizations. An exponential fit to the data at frequency ν=6761 results in an extinction length of $\ell = 11.7$ $\mu m \simeq 15a$. At ν=8295 the intensity reduction becomes again more significant as we are close to the TM stop gap. An extinction length of $\ell = 8.3$ μm for the TM polarization and $\ell = 10.2$ μm for the TE polarization is obtained.

Figure. 7.10 show the calculated extinction length versus frequency for TE polarized light. The extinction length in the band gap is in average 3 times shorter than out side the band gap due to the Bragg diffraction of the incident light in this frequency range.

Comparing the outlined data in Fig. 7.9 with the corresponding experiments performed on the Teflon sample, we clearly see influence of the periodicity of the photonic crystal sample in the stop gap range. The results outside the stop gap range is comparable with the out-of-plane scattering results from the weakly scattering Teflon sample where we do not see any clear decay of the intensity in the scanned range.

7.6 Conclusion

Out-of-plane scattering experiments on a two-dimensional photonic crystal were successfully performed. Reference measurements on a solid piece of Teflon were also conducted. By resolving the induced out-of-plane scattering in intensity and frequency, the spectral behavior of the transport of the in-coupled light in the photonic crystal is analyzed. For the Teflon sample it was observed that the out-of-plane scattering is independent of the frequency and polarization of the incident radiance. This matches the expectations for a uniform disordered random scattering material in which light is coupled in at a first order approximation with equal efficiency throughout the covered spectral range. Taking into account these reference measurements, distinct results were obtained for the out-of-plane scattering experiment performed on the two-dimensional photonic crystal. The results outline different spectral behavior for TE and TM polarized excitation. It is concluded that, the out-of-plane scattered light is influenced by photonic character of the sample showing a fast drop of intensity for the frequencies in the stop gaps.

7.7 Outlook

The list of recommendations for future research presented here is a result of the performed experimental work. Recommendation includes the use of an illuminating microscope objective with an increased numerical aperture. To minimize the scattering from the crystal edge on the out-of-plane surface of the photonic crystal the incident spot on the sample needs to be aligned on a relatively small area a few micron away from the crystal edge. By employing an illuminating objective with a high numerical aperture the focus of the illumination source on the sample becomes smaller and the mentioned unwanted effects are reduced. However, since the detection objective has a high numerical aperture, in this case, due to the spatial extent of the two high numerical aperture objectives it is not possible to place two objectives close enough to each other. Therefore it is not possible to fulfill the requirements of the current state-of-art experimental scheme. Another draw-back of using a high NA objective is launching a wide range of wave vectors into the sample and therefore wiping out the effect of narrow stop gaps. Possible solutions here are the use of samples which contain a larger photonic crystal, or to implement a fiber as an illumination source. The latter solution is at the moment the most feasible, but it is expected to result in an even more cumbersome alignment of the experimental scheme.

In order to reduce effects of the artifacts in the data it is recommended to check the sample surface with a microscope and mark a clean area on the sample surface, prior to the experiment.

The experimental setup enables to measure the in-situ reflectivity of the photonic crystal. It is recommended to acquire the spectral position of photonic stop gaps by means of in-situ reflectivity measurements. This enables to directly compare the out-of-plane scattering experiments with the reflectivity of the photonic crystal obtained with identical experimental settings.

For future research, out-of-plane scattering experiments on three-dimensional photonic crystals is proposed. These kinds of crystal are fabricated by etching two sets of carefully aligned perpendicular pores as explained in chapter 2. Since this crystal possess a full photonic band gap, the long-searched localization of light in three spatial dimensions is achievable.

Bibliography

[1] W. Vos, R. Sprik, A. van Blaaderen, A. Imhof, A. Lagendijk, and G. H. Wegdam, *Strong effects of photonic band structures on the diffraction of colloidal crystals*, Phys. Rev. B. **53**, 16231 (1996). — p.109.

[2] E. Yablonovitch, *Inhibited spontaneous emission in solid-state physics and electronics*, Phys. Rev. Lett. **58**, 2059 (1987). — p.109.

[3] M. D. Leistikow, A. P. Mosk, E. Yeganegi, S. R. Huisman, A. Lagendijk, and W. L. Vos, *Inhibited spontaneous emission of quantum dots observed in a 3D photonic band gap*, Phys. Rev. Lett. **107**, 193903 (2011). — p.109.

[4] G. Demésy and S. John, *Solar energy trapping with modulated silicon nanowire photonic crystals*, J. Appl. Phys. **112**, 074326 (2012). — p.109.

[5] J. G. Fleming and S. Y. Lin, *Three-dimensional photonic crystal with a stop band from 1.35 to 1.95 μm*, Opt. Lett. **24**, 49 (1999). — p.109.

[6] A. Blanco, E. Chomski, S. Grabtchak, M. Ibisate, S. John, S. W. Leonard, C. Lopez, F. Meseguer, H. Miguez, J. P. Mondia, G. A. Ozin, O. Toader, and H. M. van Driel, *Large-scale synthesis of a silicon photonic crystal with a complete three-dimensional bandgap near 1.5 micrometres*, Nature **405**, 437 (2000). — p.109.

[7] S. Noda, K. Tomoda, N. Yamamoto, and A. Chutinan, *Full three-dimensional photonic bandgap crystals at near-infrared wavelengths*, Science **289**, 604 (2000). — p.109.

[8] Y. A. Vlasov, X. Z. Bo, J. C. Sturm, and D. J. Norris, *On-chip natural assembly of silicon photonic bandgap crystals*, Nature **414**, 289 (2001). — p.109.

[9] A. F. Koenderink, M. Megens, G. v. Soest, W. L. Vos, and A. Lagendijk, *Enhanced backscattering from photonic crystals*, Phys. Lett. A **268**, 104 (2000). — p.109.

[10] S. Hughes, L. Ramunno, J. F. Young, and J. E. Sipe, *Extrinsic optical scattering loss in photonic crystal waveguides: role of fabrication disorder and photon group velocity*, Phys. Rev. Lett. **94**, 033903 (2005). — p.109.

[11] A. F. Koenderink, A. Lagendijk, and W. L. Vos, *Optical extinction due to intrinsic structural variations of photonic crystals*, Phys. Rev. B **72**, 153102 (2005). — p.109, 120.

[12] P. M. Johnson, S. Faez, and A. Lagendijk, *Full characterization of anisotropic diffuse light*, Opt. Express **16**, 7435 (2008). — p.109, 110.

[13] A. Avoine, C. Vion, J. Laverdant, S. Bonnefont, O. Gauthier-Lafaye, L. Coolen, and A. Maître, *Photonic crystal cavity modes in the visible range characterized by scattering spectroscopy*, Phys. Rev. A **82**, 063809 (2010). — p.109.

[14] C. F. Bohren and D. R. Huffman, *Absorption and scattering of light by small particles* (John Wiley, 2008). — p.110.

[15] B. P. J. Bret, *Multiple light scattering in porous gallium phosphide*, PhD Thesis, Universiteit Twente, 2005. — p.110.

[16] A. F. Koenderink and W. L. Vos, *Light exiting from real photonic band gap crystals is diffuse and strongly directional*, Phys. Rev. Lett. **91**, 213902 (2003). — p.111.

[17] S. R. Huisman, *Observing the forbidden zone for light*, Master Thesis, University of Twente, 2010. — p.112.

[18] S. R. Huisman, R. V. Nair, A. Hartsuiker, L. A. Woldering, A. P. Mosk, and W. L. Vos, *Observation of sub-bragg diffraction of waves in crystals*, Phys. Rev. Lett. **108**, 083901 (2012). — p.112.

[19] S. R. Huisman, R. Nair, L. A. Woldering, M. D. Leistikow, A. P. Mosk, and W. L. Vos, *Signature of a three-dimensional photonic band gap observed on silicon inverse woodpile photonic crystals*, Phys. Rev. B **83**, 205313 (2011). — p.120.

CHAPTER 8

Summary and outlook

In this thesis both theoretical and experimental studies have been presented on light emission and propagation in real photonic band gap crystals. We have investigated several aspects of a real photonic band gap crystal by different types of measurements such as time resolved emission of light sources in the band gap, scattering of light due to randomness and probing the internal wave structure of photonic crystals. In this chapter we review all the studies in this thesis and based on that we give directions for future work.

The present-day understanding of complex nanophotonic systems is heavily leaning on theories that describe infinite systems. Well-known examples are random media and photonic crystals. In contrast, experiments are obviously performed on real devices with a finite extent. Many of the fascinating optical properties associated with these nanophotonic systems such as a full three-dimensional photonic band gap, weak and strong localization, and divergences in the densities of states are strongly depending on system size. Hence, the understanding of these effects is crucial for the success of our field, and will surely open up novel applications.

In this thesis we have devised an original theory that allows the models for infinite photonic crystals to be extended to represent finite-size effects, without actually reducing the size of the infinite system. The method is based on an extension of the wave-vector space of the Green's functions into the complex plane. We have successfully applied this theory to a one-dimensional system, where the results can be verified with exact calculations Green's function and transfer matrix revealing an excellent match between our theory and these calculations. A remarkable result is that the local density of states (LDOS), which is strictly zero in the band gap of an infinite crystal irrespective of frequency (within the gap of course) and position, becomes strongly dispersive and position-dependent in a finite crystal.

We developed a theory for the density of states in a finite three-dimensional photonic crystal. The theory is based on mode broadening in a finite photonic crystal. We have experimentally studied the controlling of spontaneous emission of light in real finite photonic band gap crystals. It seems that we are finally in the position to explain our experimental observations on the non-zero DOS inside the 3D photonic band gap. These observations are leveraged by time-resolved emission studies on semiconductor quantum dots that emit in the telecom range within the band gap of silicon 3D photonic crystals made by CMOS-compatible methods. It is remarkable that our theory predicts a volume dependency of the inhibition in the band gap of a finite photonic crystal. We conclude that the main limiting factors to observe an infinite inhibition in the band gap are the photonic crystal size and the non-radiative decay of the quantum emitters. Therefore future experiments at low temperature and on larger photonic crystals will definitely yield a greater inhibition in the band gap.

Recently, our group has proposed a design to realize controlled point defects in inverse woodpile crystals as studied in this thesis. Based on the calculations these point defects show all the signatures of cavity resonances where light is strongly confined. It will of course be highly intriguing to investigate the control of material excitations - be it quantum emitters or plasmonic resonances - by such resonances. For instance, the simultaneous presence of a very low background in the band gap suggests that very clear signals can be collected. From a somewhat different view, it will also be exciting to pursue Anderson localization of light, that is notably expected near the edge of the gap. Here embedded quantum emitters could play a role as internal reporter of the phenomena. In our measurements we have observed an enhancement of the quantum dot decay rate near the edge of the gap that might be caused by this phenomena.

Three-dimensional photonic band gap crystals are capable of controlling the radiative loss of any material systems. In principle any field propagation in the band gap frequency range is forbidden due to the interference effect in the band gap, no matter what is the radiation source. In this respect the radiative loss of the plasmonic systems in the band gap can also be controlled. Currently the main limitation on this experiment is fabricating plasmonic particles whose plasmonic spectrum overlaps with the photonic band gap range. The size polydispersity of the particles is currently an issue, making the plasmonic spectrum of the particles much broader than the band gap. In future when the right combination of the plasmonic particles and the photonic crystal is found, the experiments will reveal the ultimate control on the plasmonics scattering.

In this thesis, we have probed the LDOS by meaning the time-resolved emission rate of quantum dots. It is a principal disadvantage of counting photons that in the situations of interest, namely a strongly decreased LDOS, the signal also decreases. Therefore it is relevant to consider alternative methods. Signs of a photonic band gap might be also experimentally accessible by probing the excited state population. In an ideal case, if an emitter in the photonic band gap is excited it stays excited forever and therefore the excited state stays populated. Population of the excited state increases by decreasing the LDOS. In a real photonic crystal the excitation will not last forever as the LDOS is not zero, and the excited emitters decay to the ground state after several lifetimes. Meanwhile, when the emitter is in the excited state the excited state population can be probed by excited-state absorption measurements. In this case electrons in the excited state are excited to the second excited state by absorbing a photon. Since the emitters that are deeper inside the crystal experience a lower LDOS, their excited state population is higher. As opposed to the emission measurements performed in this thesis such a measurement is biased to the long life-time emitters. In the ultimate case, the longest living excited state will determine the longest remaining signal.

We have introduced a Bayesian method for time-resolved emission data analysis. In the near infrared range the time-resolved data collected from the emitters in the band gap photonic crystal are suffering from a very low signal to noise ratio. In our statistical analysis we have used the probability distribution of the background counts as prior information to improve the data analysis and refine the free parameters in modeling the data. The method can be used in any data analysis where the signal to noise ratio is low and therefore the uncertainty on parameter determination is high.

In the last chapter, we have investigated the internal waves inside photonic crystals by measuring the light scattering using correlation microscopy and scattering microscopy techniques. Coherence length, extinction length, long range, and short range order of light in the opal and in the two-dimensional photonic crystals have been measured. Here we propose future experimental studies to quantitatively investigate the scattering from photonic crystal samples. To start with, we propose to use simpler photonic structures such as Bragg stacks where the periodicity is present only in one direction. By investigating different Bragg stacks with different lattice parameters we can quantify the transport mean free path with respect to the Bragg length for different crystals. In this way we obtain information on how deep the light propagates inside the crystal.

A second proposition which simplifies the interpretation of the results is to use a low numerical aperture objective to send a small range of incident wave vector into the sample. This comes at the price of lowering the spatial resolution and illuminating a larger area on the crystal. The disadvantage is of course that the measurements will not be anymore sensitive to the short range disorder in the photonic crystals. However, the main advantage is that we will be able to investigate the directional light propagation into the photonic crystal by coupling the incident light to a limited set of Bloch modes, thereby simplify theoretical interpretation.

Thirdly, using wavefront shaping one can modulate the wavefront to couple to a particular Bloch mode. The main limitation is however that the modulation in the wavefront is diffraction limited. In order to be in the photonic range of photonic crystal we need to use light sources with the wavelength in the order of the crystal periodicity. Using an objective with NA = 0.9 for visible laser light we have a focus size of about 300 nm. Therefore the resolution of the modulated wavefront can not be smaller that 300 nm. This will limit the number of possible Bloch waves that can be generated and imaged on the crystal surface. However, it is very exciting to perform this experiment even for a simple Bloch wave and study the surface impedance and the scattering. Fascinating wavefront shaping experiments can be done by addressing cavities inside a full photonic band gap crystal.

APPENDIX A

Light propagation in periodic media

In this section we describe the optical properties of an infinitely extended 1D periodic structure. To calculate the band structure and the electromagnetic fields we have used the transfer matrix method [1, 2]. The dielectric function of the structure is real and periodic:

$$\epsilon(z) = \epsilon(z + a), \tag{A.1}$$

where a is an arbitrary lattice vector [3]. This means that the structure is invariant under the translation $(m \cdot a)$ where m is an integer and a is the period of the structure. Here we limit ourselves to propagation of light in the z-direction perpendicular to the layers, and we assume that the medium is non-magnetic. In this 1D periodic structure it is only necessary to consider one polarization due to the symmetry. The propagation of light with frequency ω in a periodic structure is described by Maxwell's equations [1, 4]. Due to symmetry these equations remain the same after substituting $(z + a)$ for z in the operators and ϵ. The solutions of the wave equation have the form of a plane wave times a function with the periodicity of the lattice

$$\mathbf{E}_{n,K}(z) = \bar{\mathbf{E}}_{n,K}(z)e^{-iKz}, \tag{A.2}$$

where $\bar{\mathbf{E}}_{n,K}(z)$ is periodic with the lattice

$$\bar{\mathbf{E}}_{n,K}(z) = \bar{\mathbf{E}}_{n,K}(z + a), \tag{A.3}$$

which is known as the Bloch-Floquet theorem. The subscript K indicates that the function $\bar{\mathbf{E}}_{n,K}(z)$ depends on the Bloch wave number K. Note that Eq. A.2 and Eq. A.3 imply that:

$$\mathbf{E}_{n,K}(z) = \mathbf{E}_{n,K}(z + a)e^{-iKa}, \tag{A.4}$$

The problem at hand is thus of determining K and $\bar{\mathbf{E}}_{n,K}(z)$ as a function of ω. To this end we have used the transfer matrix method together with the Bloch condition to calculate the band structure and the Bloch fields propagating in the structure. The electric field within each homogeneous layer is expressed as a sum of an incident and a reflected plane wave:

$$\mathbf{E}_{n,K}(z) = b^{-}e^{-ikz} + b^{+}e^{ikz}, \tag{A.5}$$

where $k = \frac{n\omega}{c}$ is the wave vector and b^- and b^+ are coefficients that are related through the continuity conditions at the interfaces. Using Maxwell's equations one obtains the general form of the magnetic field amplitude:

$$\mathbf{B}_{n,K}(z) = b^- \sqrt{\epsilon} e^{-ikz} - b^+ \sqrt{\epsilon} e^{ikz}, \tag{A.6}$$

Imposing the continuity of the electric and magnetic fields at two consecutive interfaces leads to a matrix that connects the coefficients of one homogeneous layer(n) to the coefficients of the same type of layer($n+1$) in the next period. These can be written as the following matrix equation:

$$\begin{pmatrix} b_{n-1}^- \\ b_{n-1}^+ \end{pmatrix} = \begin{pmatrix} A & B \\ C & D \end{pmatrix} \begin{pmatrix} b_n^- \\ b_n^+ \end{pmatrix} \tag{A.7}$$

where $T = \begin{pmatrix} A & B \\ C & D \end{pmatrix}$ is a transfer matrix that relates the coefficients of the same type of layers. The matrix elements A, B, C, and D are complex functions of the layers properties such as the dielectric permittivity (ϵ_i) and the width (a_i) of each layer. As a consequence, only the first two components b_0^- and b_0^+ (or the first column vector $\begin{pmatrix} b_0^- \\ b_0^+ \end{pmatrix}$) can be chosen arbitrarily. If we choose the column vector of layer 1 in the zeroth unit cell ($n = 0$), then the remaining column vectors of the equivalent layers are related to that of zeroth unit cell by :

$$\begin{pmatrix} b_n^- \\ b_n^+ \end{pmatrix} = \begin{pmatrix} D & -B \\ -C & A \end{pmatrix}^n \begin{pmatrix} b_0^- \\ b_0^+ \end{pmatrix} \tag{A.8}$$

Besides the continuity conditions that should be satisfied, the periodic layers must be invariant under lattice translation, in other words the Bloch condition Eq. A.4 must be satisfied. In terms of our column vector representation and from Eq. A.5, the Bloch condition Eq. A.4 yields

$$\begin{pmatrix} b_n^- \\ b_n^+ \end{pmatrix} = e^{-iKa} \begin{pmatrix} b_{n-1}^- \\ b_{n-1}^+ \end{pmatrix}. \tag{A.9}$$

By combining Eq. A.7 and Eq. A.9 the column vector of the Bloch wave satisfies the following eigenvalue equation:

$$\begin{pmatrix} A & B \\ C & D \end{pmatrix} \begin{pmatrix} b_n^- \\ b_n^+ \end{pmatrix} = e^{iKa} \begin{pmatrix} b_n^- \\ b_n^+ \end{pmatrix}. \tag{A.10}$$

The eigenvalues are equal to

$$e^{iKa} = \frac{1}{2}(A+D) + [\frac{1}{4}(A+D)^2 - 1]^{1/2} \tag{A.11a}$$

$$e^{iKa} = \frac{1}{2}(A+D) - [\frac{1}{4}(A+D)^2 - 1]^{1/2} \tag{A.11b}$$

that are the reciprocal of each other. The eigenvectors corresponding to the eigenvalues are

$$\begin{pmatrix} b_0^- \\ b_0^+ \end{pmatrix} = \begin{pmatrix} B \\ e^{iKa} - A \end{pmatrix}. \tag{A.12}$$

This bring us to the point that although for the transfer matrix method one column vector $\begin{pmatrix} b_0^- \\ b_0^+ \end{pmatrix}$ can be independently chosen, since we have imposed the Bloch condition this column vector will be set by Bloch condition as Eq. A.12. That means that depending on K there exists a unique initial condition for which the electromagnetic field propagates into the periodic structure and this initial condition depends on the properties and the geometry of the periodic structure. To normalize the initial condition we have normalized the field such that if we consider both layers to be vacuum, the intensity of the field propagating in vacuum is equal to one and does not depend on frequency, therefore:

$$\begin{pmatrix} b_0^- \\ b_0^+ \end{pmatrix} = \begin{pmatrix} 1 \\ (e^{iKa} - A)/B \end{pmatrix} \tag{A.13}$$

According to Eq. A.9 the corresponding field amplitudes for the n^{th} unit cell are equal to

$$\begin{pmatrix} b_n^- \\ b_n^+ \end{pmatrix} = e^{-inKa} \begin{pmatrix} 1 \\ (e^{iKa} - A)/B \end{pmatrix} \tag{A.14}$$

With the initial conditions and the Bloch wave vector K we obtain the fields and dispersion relation between ω and K for the Bloch wave function.

$$K(\omega) = \frac{1}{a} \cos^{-1}[\frac{1}{2}(A + D)]. \tag{A.15}$$

Bibliography

[1] A. Yariv and P. Yeh, *Optical waves in crystal: Propagation and control of laser radiation* (John Wiley, New York, 1983). — p.129.

[2] C. Barnes and J. B. Pendry, *Multiple scattering of waves in random media : a transfer matrix approach*, Proc. Mat. Phys. Sc **435**, 185 (1991). — p.129.

[3] N. W. Ashcroft and N. D. Mermin, *Solid state physics* (Holt, Rinehart and Winston, New York, 1976). — p.129.

[4] J. D. Joannopoulos, S. G. Johnson, J. N. Winn, and R. D. Meade, *Photonic crystals - molding the flow of light, 2nd edition* (Princeton University Press, 2008). — p.129.

APPENDIX B

Decay rate versus frequency of PbS quantum dots

Semiconductor quantum dots of $IV - VI$ materials such as PbS and PbSe offer unique access to the regime of extreme quantum confinement since the electron, hole, and exciton all have relatively large Bohr radii [1]. In PbS, the electron, hole, and exciton Bohr radii are 10, 10, and 18 nm, respectively. These large radii allow strong confinement to be achieved in relatively large structures. Thus, QDs of $IV - VI$ materials have properties reflecting all benefits of strong quantum confinement, with reduced influence from surface effects.

In this section we discuss the decay rate of the PbS quantum dots in toluene versus frequency. In chapter 4 we do the same experiment for the quantum dots in the photonic crystals. Therefore, it is important to study their behavior before placing them in a more complex environment.

The decay rate measured as a function of frequency is shown in Fig. B.1 (a). The decay rate was obtained from data as in Fig .2.3 (b). It is seen that the decay rates are a function of the emission frequency, which is a direct confirmation that the emission spectrum is inhomogeneously broadened. It is known that the bigger quantum dots have a smaller band gap and therefore emit at lower frequency and as the size increases the emission frequency decreases [2]. In our measurements at lower frequencies (larger quantum dots) we observe a higher decay rate. Hence the decay rate increases with increasing quantum dot size. For the PbSe quantum dots three data points have been measured by Husken [3], showing a similar trend as shown in Fig. B.1. The same experiment was performed by Moreels *et al* [4] on PbS quantum dots, in which they measured the decay rate versus quantum dot size for a very wide range of the quantum dot size. The result of their results in the same range as we measured shows an almost constant decay rate without a clear increasing or decreasing trend.

As a first step to interpret the result, we have calculated the radiative decay rate versus frequency for an ideal two-level exciton PbS quantum dot using the following equation:

$$\gamma_{rad}(\omega) = \frac{e^2 n\omega^2}{6m_e\epsilon_0\pi c^3} f_{em}(\omega), \tag{B.1}$$

Equation (B.1) gives the emission oscillator strength $f_{em}(\omega)$ of the transition as a function of radiative decay rate [5]. Here e is the electron charge, n is refractive index of surrounding material, m_e is the electron mass, ω is emission frequency, ϵ_0 is vacuum permittivity, and c is speed of light in vacuum. In the strong confinement limit of the exciton wavefunction the oscillator strength is

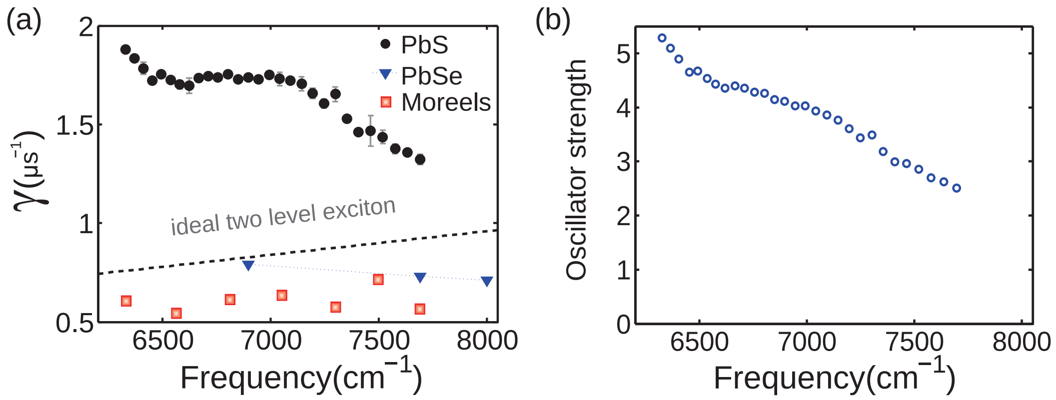

Figure B.1: (a) The decay rate measured versus frequency on PbS quantum dots ensemble (black circles). The behavior is opposite to the expectation for an ideal exciton that the decay rate is proportional to the emission frequency as it is plotted with gray dashed line. A similar measurements on PbSe quantum dots shows the same trend (blue triangles). The red squares shows measurements on PbS quantum dots by Moreels *et al* [4]. Their measurements in the same range shows an almost constant decay rate. (b) The calculated oscillator strength for the PbS quantum dots increases with quantum dot size.

given by [6]:

$$f_{em} = \frac{4}{\sqrt{3}}\pi\frac{a_B^{*3}}{a^3}\frac{\omega_{bulk}}{\omega}f_{bulk} \tag{B.2}$$

where f_{bulk} is the oscillator strength in bulk per chemical PbS unit, a_B^* is the exciton Bohr radius, ω_{bulk} is bulk emission frequency, ω is emission frequency of the quantum dots that depends on quantum dot radius, and a is the lattice constant. We consider $a_B^* = 18$ nm, $a = 0.59$ nm, $f_{bulk} = 1.4 \cdot 10^{-4}$, $\omega_{bulk} = 0.37$ eV [7], and ω varies between 6000 cm^{-1} to 8000 cm^{-1} as in the experiment. The behavior of the decay rate versus frequency is shown in Fig. B.1. The ideal PbS quantum dots shows an increasing decay rate with frequency (or decreasing quantum dot radius), which is an inverse behavior compared to the measured data.

To interpret the difference between our observation and the two level exciton model, we discuss three possible hypotheses for the observed increase of the quantum dot decay rate with size, based on literature. First the non-radiative decay rate may become larger for larger dot sizes, due to phonon coupling. This essentially means that the changes in decay rate are due to changes in the quantum efficiency of the dots. However, phonon interactions are expected to be small due to the strong confinement that are especially important in PbS quantum dots [1]. Therefore we reject this first hypothesis.

Second, a size dependence of the spatial overlap of the electron and hole wavefunctions may cause a change of the radiative decay rate, as has been observed for InAs quantum dots [8]. However, for PbS quantum dots it is very unlikely that the wavefunctions shift much due to the strong confinement. Therefore this hypothesis is also rejected.

The third explanation for the changes in decay rate is related to the difference in oscillator strength of the dots with different sizes, since the decay rate is written explicitly as a function of the emission oscillator strength $f_{em}(\omega_j)$. We have calculated the oscillator strength for our PbS quantum dots as shown in Fig. B.1 (b). The oscillator strength increases with the quantum dot size. As it has been calculated by Moreels *et al* [4], following the tight-binding model for the PbS and PbSe quantum dots, oscillator strength scales approximately linearly with the quantum dot size, which confirms our calculations. The change of oscillator strength with size can be explained by a size dependent dipole moment of these quantum dots. We therefore believe that the oscillator strength causes the change in the decay curves, instead of non-radiative process or the wave function overlap. Beside the opposite trend of the decay rate, the decay rate shows a non-linear trend versus frequency. Such a behavior can be assigned to parity-forbidden transitions in PbS quantum dots as discussed in Ref. [9].

To conclude the decay rates has been measured as a function of frequency and therefore as a function of quantum dots size. The measurements show increase of the decay rate as a function of quantum dots size suggesting that the emission spectrum is inhomogeneously broadened

Bibliography

[1] F. W. Wise, *Lead salt quantum dots: the limit of strong quantum confinement*, Acc. Chem. Res. **33**, 773 (2000). — p.133, 134.

[2] A. I. Ekimov and A. A. Onushchenko, *Size quantization of the electron energy spectrum in a microscopic semiconductor crystal*, JEPT Lett **40**, 1136 (1984). — p.133.

[3] B. H. Husken, *Spontaneous emission of near-infrared quantum dots controlled with photonic crystals*, PhD Thesis, University of Twente, 2009. — p.133.

[4] I. Moreels, K. Lambert, D. Smeets, D. De Muynck, T. Nollet, J. C. Martins, F. Vanhaecke, A. Vantomme, C. Delerue, G. Allan, and Z. Hens, *Size-dependent optical properties of colloidal PbS quantum dots.*, ACS Nano **3**, 3023 (2009). — p.133, 134, 135.

[5] A. Siegman, *Lasers* (University Science Books, 1986). — p.133.

[6] Y. Kayanuma, *Quantum-size effects of interacting electrons and holes in semiconductor microcrystals with spherical shape*, Phys. Rev. B **38**, 9797 (1988). — p.134.

[7] E. D. Palik, *Handbook of optical constants of solids* (Academic Press, 1985). — p.134.

[8] J. Johansen, S. Stobbe, I. S. Nikolaev, T. Lund-Hansen, P. T. Kristensen, J. M. Hvam, W. L. Vos, and P. Lodahl, *Size dependence of the wavefunction of self-assembled inas quantum dots from time-resolved optical measurements*, Phys. Rev. B **77**, 073303 (2008). — p.134.

[9] L. Cademartiri, E. Montanari, G. Calestani, A. Migliori, A. Guagliardi, and G. A. Ozin, *Size-dependent extinction coefficients of PbS quantum dots.*, J. Am. Chem. Soc **128**, 10337 (2006). — p.135.

APPENDIX C

Control radiative linewidth of plasmonics with photonic crystals

C.1 Decay mechanism of plasmonic particles

Our goal is to control the radiative properties of surface plasmon polaritons using photonic crystals. The optical response of a metallic nanoparticle depends on its shape, size and environment [1]. Free plasmons excited by electrons are not discussed here. The homogeneous linewidth Γ of the plasmon resonance is related to the dephasing time T_2 by $\Gamma = \dfrac{2\hbar}{T_2}$, which is related to the time constant of population decay T_1(total life time) by

$$\frac{1}{T_2} = \frac{1}{2T_1} + \frac{1}{T^*}. \tag{C.1}$$

The term T^* is the pure dephasing time corresponding to elastic collisions such as phonon interactions, which can be controlled by temperature. Inelastic decay occurs via the transformation of a plasmon into a photon or via nonradiative decay, such as the creation of electron hole-pairs by intraband or interband transitions. Therefore the total decay includes radiative $T_{1,r}$ and non-radiative $T_{1,nr}$, ($T_1^{-1} = T_{1,r}^{-1} + T_{1,nr}^{-1}$). The non-radiative decay can also be controlled by the temperature but the radiative decay is completely determined by the LDOS. A beautiful example of the latter effect was demonstrated on a single nanosphere near a mirror [2], and a few subsequent studies [3–5].

Photonic band gap crystals have been demonstrated to strongly inhibit the LDOS [6–10], and hence to control spontaneous emission of embedded quantum emitters. Therefore in this section, we explore the feasibility of inhibiting the radiative plasmonic damping rate, which is considered to be an important loss mechanism of plasmons [11].

If we consider a plasmonic resonance as a dipole, then the rate of decay for such a dipole transition between an initial i and an available final f dipole-field state is proportional to the local density of states at the atom position (LDOS), as stated by Fermi's Golden Rule:

$$\gamma_{i\to f}(\omega, \vec{r}, \vec{e_d}) = \frac{\pi\omega d^2}{\hbar\epsilon_0} N(\omega, \vec{r}, \vec{e_d}). \tag{C.2}$$

Here $T_{1,r}^{-1} = \gamma_{i\to f}$.

C.2 Investigation: controlling plasmonic radiation of gold nanorods with photonic crystals

To control the radiative plasmonic loss we consider 2D and 3D silicon inverse woodpile photonic crystals. As discussed in chapter 2, these crystals have the broadest band gap among all fabricated crystals. Since a broader band gap results in a smaller value for the LDOS inside the gap of a finite crystal, these crystals are the most appealing for our purpose. Since the crystals are made of silicon, and silicon is transparent for the range $\omega \leq 1.1eV$, thus photonic crystals are designed such that they form a complete photonic band gap in the infrared range.

In order to control the plasmonic radiation we need to choose the particles such that their extinction spectrum not only overlaps with the band gap in the near infrared ($\omega \leq 1.1$ eV), but is also narrower than the band gap range [12]. Among a large variety of different types of plasmonic particles, such as spheres, core-shells, and nanorods, we have chosen gold nanorods. The nanorods have a higher albedo and a narrower relative linewidth in the near infrared compared to spheres and core-shell particles. Another advantage of the nanorods is that their plasmon resonances can be tuned easily to the desired frequency range by changing their aspect ratio [13].

C.2.1 Extinction of gold nanorod suspensions

Organic gold rod nano-particles have been purchased from NANOPARTz. They are delivered as suspension in "Short chained Alkane Alcohol" and can be maximally diluted 10× with an organic solvent. The nanorods have an aspect ratio c=10, length l=100 nm and diameter d=10 nm, with a broad aspect ratio distribution of around 50%. To measure the surface plasmon resonance peak we have prepared the gold nanorods diluted in toluene with different concentrations (3× and 5× dilution) and also a reference sample of only toluene. Since we want to infiltrate particles in the photonic crystal, we expect their resonance frequency to shift due to a change in the refractive index of the substrate. Therefore, we have made also samples which consist of Au particles dried on top of a silicon wafer, and in this case a piece of silicon wafer has been used as reference.

To understand the effect of aspect ratio distribution of the particles the spectrum of one single nanorod was calculated by Coupled Dipole Approximation method, which is also known as the Discrete Dipole Approximation, as shown in Fig. C.1*. The nanorod has a length of l=102 nm and a diameter of d=10 nm in a homogenous environment of refractive index n=1.33. The calculation shows a peak resonance at 1100 nm, with a FWHM of about 150 nm.

The extinction spectra of Au particles 3× diluted in toluene and on a silicon wafer are shown in Fig. C.1. As it was specified by the company the resonance frequency of particles in suspension is around λ=1400 nm. The measurement shows a very broad extinction peak of 500 nm FWHM, broader than what we

---

* We thank Prof. W. L. Barnes and Alastair Humphrey for performing this calculation.

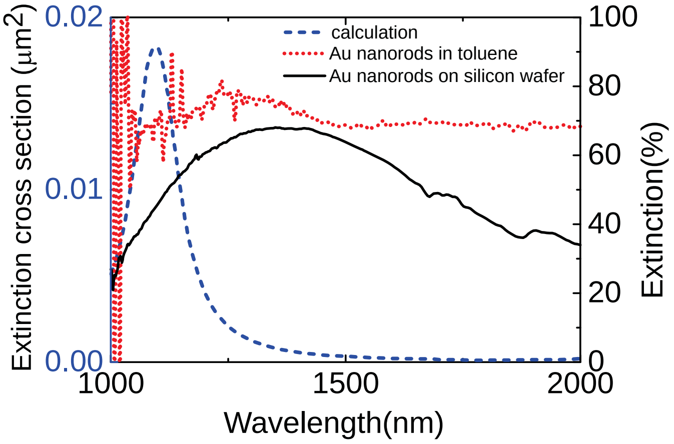

Figure C.1: Extinction spectrum of Au particles (E12N-10-1400), purchased from NANOPARTz 3× diluted in toluene. The peak of intensity is around 1400 *nm* as specified by the company (black solid curve), and dried on the surface of a silicon wafer (red dotted curve). The particles on the silicon surface experience a higher refractive index environment and therefore their resonance frequency shifts to the lower wavelengths as expected. Blue dashed curve shows the calculated extinction cross section of one nanorod with length 100 nm and diameter 10 nm in a medium with refractive index 1.33.

expect from the calculation. Comparing the measurements and the calculation indicates that the linewidth measured in suspension is mostly dominated by inhomogeneous broadening. For the particles dried on the silicon wafer, the resonance frequency is red shifted, and due to reflection from the silicon substrate the reflectivity increases for the entire range of the measurements.

In order to investigate the possibility of controlling plasmonic radiative losses with silicon two-dimensional photonic crystals, we have plotted the measured extinction spectrum of the nanorods together with reflectivity measurements of a 2D crystal in Fig. C.2. The reflectivity spectra are measured on different crystal directions and light polarizations as discussed extensively in [14]. In the range of the stop gap the incident light cannot propagate inside the crystal and is reflected back, appearing as a peak in the reflection spectrum. In this range not only the external field is forbidden to enter the crystal, inside the crystal the field propagation is also prohibited resulting in a low local density of states. Therefore the reflectivity peaks are also an indication of the range of low LDOS in the crystal, where the plasmonic radiation can be inhibited. Comparing the different reflectivity peaks with the surface plasmon resonance peak, an overlap in the ΓK direction with TM polarization of the incident light (red dashed curve) is seen. Although in this direction the stop gap is very broad, the control over the radiation loss is unfortunately not achievable since the extinction spectrum is much broader.

During the synthesis, nanorods form a constant width but a large variation in length. Afterwards, the particles of the wanted aspect ratio have to be filtered out which is only possible with an accuracy of about 10 nm. This would result in

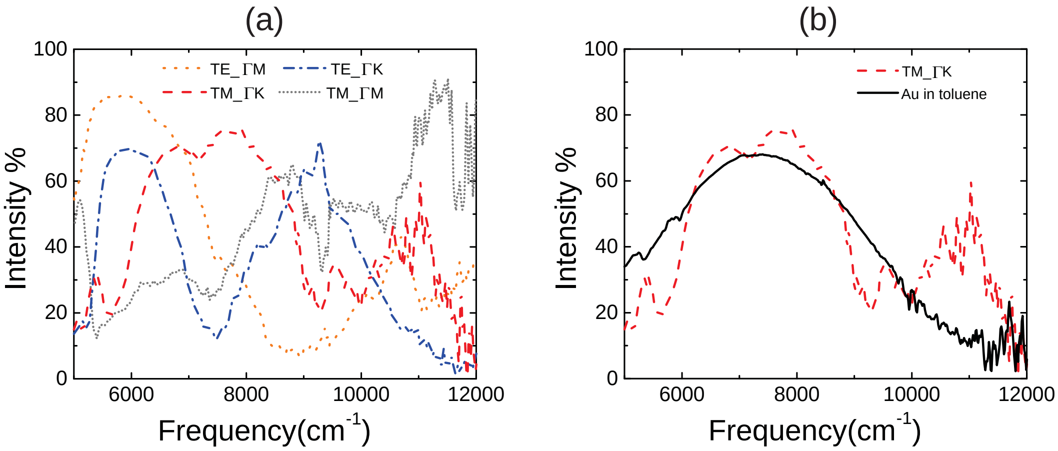

Figure C.2: (a) Reflectivity spectra of a 2D silicon photonic crystal with different light polarizations and different crystal directions. (b) Extinction spectrum of gold nano-rods in comparison with reflectivity spectrum of the 2D photonic crystal. The extinction spectrum has a very good overlap with ΓK direction and TM polarization of the reflectivity spectrum. However, due to inhomogeneous broadening of the nano-rods their extinction spectrum is much broader than the calculated spectrum, making them ineligible for our purpose.

a large inhomogeneous linewidth. In future when higher quality nanorods with narrow linewidth will be available, it will be possible to control the plasmonic loss using different stop gaps, or even ultimately control the plasmonic loss using a full 3D photonic band gap.

Bibliography

[1] C. F. Bohren and D. R. Huffman, *Absorption and scattering of light by small particles* (John Wiley, 2008). — p.137.

[2] B. C. Buchler, T. Kalkbrenner, C. Hettich, and V. Sandoghdar, *Measuring the quantum efficiency of the optical emission of single radiating dipoles using a scanning mirror*, Phys. Rev. Lett. **95**, 063003 (2005). — p.137.

[3] M. W. Knight, Y. Wu, J. B. Lassiter, P. Nordlander, and N. J. Halas, *Substrates matter: influence of an adjacent dielectric on an individual plasmonic nanoparticle*, Nano Lett. **9**, 2188 (2009). — p.137.

[4] T. Kalkbrenner, U. Håkanson, A. Schädle, S. Burger, C. Henkel, and V. Sandoghdar, *Optical microscopy via spectral modifications of a nanoantenna*, Phys. Rev. Lett. **95**, 200801 (2005). — p.137.

[5] K. Imura, T. Nagahara, and H. Okamoto, *Near-field optical imaging of plasmon modes in gold nanorods*, J. Chem. Phys. **122**, 154701 (2005). — p.137.

[6] E. Yablonovitch, *Inhibited spontaneous emission in solid-state physics and electronics*, Phys. Rev. Lett. **58**, 2059 (1987). — p.137.

[7] K. Busch and S. John, *Photonic band gap formation in certain self-organizing systems*, Phys. Rev. E **58**, 3896 (1998). — p.137.

[8] I. S. Nikolaev, W. L. Vos, and A. F. Koenderink, *Accurate calculation of the local density of optical states in inverse-opal photonic crystals*, J. Opt. Soc. Am. B **26**, 987 (2009). — p.137.

[9] M. D. Leistikow, A. P. Mosk, E. Yeganegi, S. R. Huisman, A. Lagendijk, and W. L. Vos, *Inhibited spontaneous emission of quantum dots observed in a 3D photonic band gap*, Phys. Rev. Lett. **107**, 193903 (2011). — p.137.

[10] E. Yeganegi, A. Lagendijk, A. P. Mosk, and W. L. Vos, *Local density of optical states in the band gap of a finite one-dimensional photonic crystal*, Phys. Rev. B **89**, 045123 (2014). — p.137.

[11] H. Mertens, A. F. Koenderink, and A. Polman, *Plasmon-enhanced luminescence near noble-metal nanospheres: comparison of exact theory and an improved Gersten and Nitzan model*, Phys. Rev. B **76**, 115123 (2007). — p.137.

[12] I. S. Nikolaev, P. Lodahl, and W. L. Vos, *Fluorescence lifetime of emitters with broad homogeneous linewidths modified in opal photonic crystals*, J. Phys. Chem. C **112**, 7250 (2008). — p.138.

[13] G. W. Bryant, F. J. G. de Abajo, and J. Aizpurua, *Mapping the plasmon resonances of metallic nanoantennas*, Nano Lett. **8**, 631 (2008). — p.138.

[14] S. R. Huisman, R. Nair, L. A. Woldering, M. D. Leistikow, A. P. Mosk, and W. L. Vos, *Signature of a three-dimensional photonic band gap observed on silicon inverse woodpile photonic crystals*, Phys. Rev. B **83**, 205313 (2011). — p.139.

Algemene Nederlandse samenvatting

Het belang van licht voor de mensheid wordt weerspiegeld in de enorme inspanningen die wereldwijd worden geleverd om haar ontstaan en voortplanting te beheersen. Profiterend van de wisselwerking tussen licht en materie zijn zorgvuldig ontworpen optische elementen, zoals spiegels en lenzen, in de afgelopen eeuwen succesvol toegepast voor het manipuleren van licht.

Sinds kort is het ook mogelijk om licht tot extreem te manipuleren, op nanoschaal, door composieten te gebruiken met typische afmetingen in de orde van een golflengte of nog kleiner.

Fotonische kristallen behoren tot de meest veelbelovende nanostructuren voor het beheersen van lichtemissie en propagatie. Fotonische kristallen zijn nanostructuren met een periodieke samenstelling, met een periodiciteit in de orde van de golflengte van licht. Een ééndimensionaal fotonisch kristal is slechts in één richting periodiek, zoals een 'Bragg stack'. In dit geval kan de propagatie van licht loodrecht op de lagen worden beheerst, door constructieve en destructieve interferentie van het licht dat door verschillende kristalvlakken wordt gereflecteerd.

Wanneer de periodiciteit zich in twee dimensies voordoet, kan het licht ook in twee dimensies worden beheerst. De uiterste beheersing over lichtpropagatie en emissie kan worden verkregen wanneer de periodiciteit zich in alle drie dimensies voordoet. In dat geval kan er voor een bepaald interval van de lichtfrequentie in alle richtingen en voor beide polarisaties van het licht constructieve interferentie optreden. Dat maakt het voor het licht onmogelijk om zich voort te planten binnenin het kristal. Dit frequentiebereik wordt het bereik van de fotonische bandkloof genoemd. Ook als er lichtbronnen zijn die zich in het kristal bevinden, en licht uitzenden in het frequentiebereik van de bandkloof, kan het licht zich niet voortplanten buiten het kristal.

De meest opmerkelijke eigenschap van een kristal met een fotonische bandkloof is het beheersen van spontane emissie van licht. Bij spontane emissie zendt een lichtbron een foton uit in een willekeurige richting en op een willekeurig tijdstip. Dit proces wordt niet alleen bepaald door de lichtbron zelf, maar ook door zijn omgeving. Overal om ons heen bevindt zich een flucturerend elektromagnetisch veld. Deze fluctuaties bestaan zelfs in vacuüm. Hoewel de fluctuaties gemiddeld genomen over de tijd nul zijn, zijn ze de hele tijd om ons heen. Door interactie van een lichtbron met deze fluctuaties wordt een foton uitgezonden. Aangezien de fluctuaties niet voorspelbaar zijn, is het principieel niet mogelijk om vooraf te bepalen wanneer dit foton zal worden uitgezonden. Wat wel kan worden bepaald, is de gemiddelde tijdsduur voor het uitzenden van een foton. Door gebruik te maken van een fotonische bandkloof kristal is het mogelijk om deze toevallige verschijnselen te beheersen.

Dat is precies wat er in ons experiment is gedaan. We veranderen de omgeving van de lichtbronnen in een omgeving waar geen vacuümfluctuaties aanwezig zijn: “de fotonische bandkloof”. Voor de lichtbron wordt een suspensie van PbS quantum dots in tolueen in de silicium ‘inverse woodpiles’ fotonische kristallen ingebracht. We meten de vervalsnelheid van de quantum dots in het fotonische bandkloof kristal; de ratio van de vervalsnelheid van de quantum dots in suspensie versus de vervalsnelheid van de quantum dots in het fotonisch band gap kristal. In ons experiment zien we, voor het eerst ooit, een sterke afremming van spontane emissie in echte fotonische bandkloof kristallen, met het waarnemen van niet minder dan achttien keer langere levensduur van quantum dots in de bandkloof.

Volledige controle over de voortplanting van licht is alleen mogelijk in een oneindig groot kristal. Omdat een oneindig kristal in de realiteit niet bestaat en ieder fotonisch kristal eindig is, blijft het absoluut verboden gebied voor licht een theoretisch concept. Maar wij hebben het concept experimenteel zo goed mogelijk waargemaakt.

De gemeten emissie van quantum dots in de bandkloof, opgelost naar optische frequentie, heeft geleid tot een nieuw begrip van effecten van eindige afmetingen op de bandkloof bereik, hetgeen resulteert in een nieuw gezichtspunt. In dit originele gezichtspunt, toegelicht in hoofdstuk 3 en 4 van dit proefschrift, hebben we de golfvectorruimte en de frequentieruimte uitgebreid in de complexe ruimte. We hebben twee Ansatzes ontwikkeld: de eerste is gebaseerd op tunneling van vacuümfluctuaties vanuit de vrije ruimte in het fotonische bandkloof kristal. Licht inclusief vacuümfluctuaties, dat zich voortplant in de vrije ruimte tunnelt het kristal in door het imaginaire deel van de golfvector. Dit imaginaire deel van de golfvector is een functie van de structuur van het fotonische kristal en is afhankelijk van de breedte van de bandkloof De tweede Ansatz is dat de eigen trillingen van het kristal die deltafuncties zijn in een oneindig kristal, ver- breden in een eindig kristal en Lorentzfuncties worden. Wij stellen voor dat de breedte en het aantal van deze Lorentz-modes afhangt van de grootte van het kristal. Op basis van deze twee Ansatzes ontwikkelden we een model om de lokale toestandsdichtheid te berekenen in de bandkloof van een eindig kristal en we vergeleken de berekeningen met onze metingen. De vergelijking toont een uitstekende overeenkomst, en verifiëert ons model. Het model is een algemeen model dat kan worden gebruikt voor alle soorten fotonische kristallen en verklaart het effect van eindigheid in de emissie en de propagatie van licht in alle fotonische kristallen.